

High-resolution surface wave tomography in oceanic and continental regions:
simultaneous inversion for shear wave velocity,
azimuthal anisotropy and attenuation

By

Yingjie Yang

B.S., University of Science and Technology of China, 2000

M.S, Brown University, 2003

Thesis

Submitted in partial fulfillment of the requirements for the Degree of Doctor of
Philosophy in the department of Geological Sciences at Brown University

May 2006

© Copyright 2006 by Yingjie Yang

This dissertation by Yingjie Yang
is accepted in its present form by the Department of
Geological Sciences as satisfying the
Dissertation requirements for the degree of Doctor of Philosophy

Data _____
Donald W. Forsyth, advisor

Recommended to the Graduate Council

Data _____
Karen M. Fischer, Reader

Data _____
E. Marc Parmentier, Reader

Data _____
Yan Liang, Reader

Data _____
Goran Ekstrom, Reader

Approved by the Graduate Council

Data _____
Sheila Bonde, Dean of the Graduate School

Yingjie Yang

Brown University

Department of Geological Sciences

P.O. Box 1846, Providence, RI 02912-1846

(401) 863-1701, Yingjie_Yang@brown.edu

Education

Ph.D. Geophysics, Brown University (May, 2006)

Advisor: Donald W. Forsyth

Thesis Title: High-resolution surface wave tomography in oceanic and continental regions: simultaneous inversion for shear wave velocity, azimuthal anisotropy and attenuation

M.S. Geophysics, Brown University (May, 2003)

Thesis Title: Improving Epicentral and Magnitude Estimation of Earthquakes from T Phases by Considering the Excitation Function

B.S. Geophysics, University of Science and Technology of China (July, 2000)

Research interests:

- Regional surface wave tomography for the structure, dynamics and deformation of Earth's lithosphere and mantle
- Shear wave splitting for anisotropy structure
- Numerical modeling of surface wave propagation in 3-D heterogeneous medium.
- Oceanic earthquake location and magnitude estimation by T-phase

Refereed Publications

Yang, Y. and D.W. Forsyth, Improving epicentral and magnitude estimation of earthquakes from T phases by considering the excitation function, *Bull. Seism. Soc. Am.* 93, 2106-2122, 2003

Forsyth, D.W., and Y. Yang, M.-D Mangriotis, and Y. Shen, Coupled seismic slip on adjacent oceanic transfer faults, *Geophys. Res. Lett.*, 30(12), 1618, doi:10.1029/2002GL016454, 2003.

Yang, Y., and D.W. Forsyth, Regional tomographic inversion of amplitude and phase of Rayleigh waves with 2-D sensitivity kernels, submitted to JGI.

Manuscripts to be submitted

- Yang, Y., and D.W. Forsyth, Rayleigh wave phase velocities, small-scale convection and azimuthal anisotropy beneath southern California, to be submitted to JGR.
- Weeraratne, D.S., D.W. Forsyth, and Y. Yang, Rayleigh wave tomography of intraplate Volcanic chains west of the East Pacific Rise, in preparation.
- Yang, Y., and D.W. Forsyth, Seismic velocity and attenuation constrains on the formation of oceanic plate and the origin of the low-velocity zone, in preparation.

Conference Abstracts

- Yang, Y., and D.W. Forsyth, Improvement and Testing of Earthquake Epicentral Locations on the East Pacific Rise Using T-phases: Application to a Mainshock/Aftershock Sequence, AGU, Spring, 2001.
- Yang, Y., and D.W. Forsyth, Multiple Reverberation Seafloor Scattering: A Mechanism for T-phase Excitation, AGU, Fall, 2002.
- Yang, Y., and D.W. Forsyth, Rayleigh wave phase velocities, shear wave structure and azimuthal anisotropy beneath southern California, AGU, Fall, 2003.
- Yang, Y., and D.W. Forsyth, Improved Rayleigh wave phase velocities, attenuation structure and station site response in southern California, IRIS workshop, Tucson, 2004
- Yang, Y., and D.W. Forsyth, Tomographic inversion of amplitudes and phases of Rayleigh waves with 2-D sensitivity kernels applied to southern California, AGU, Fall, 2004.

Preface

The primary goal of this thesis is to understand the structure, dynamics, deformation and evolution of the Earth's lithosphere and mantle in both oceanic and continental settings by studying elastic wave velocity, azimuthal anisotropy and attenuation structure using surface waves.

In chapter 1, we revised 2-D Born-approximation sensitivity kernels of surface waves for the global case to that for a regional case. The 2-D sensitivity kernels for regional cases are used to calculate the scattered wavefield of a plane Rayleigh wave propagating over heterogeneous structure. To assess the accuracy of 2-D sensitivity kernels in describing the wavefield, we used a pseudo-spectral method to numerically simulate a Rayleigh wave propagation and compare it to the calculated wavefield based on sensitivity kernels. We found that the kernels can accurately predict the perturbation of the wavefield even when the size of anomaly is larger than one wavelength. Based on the 2-D sensitivity kernels, we developed a surface wave tomography method by representing the incoming waves as two plane waves. For each plane wave, the 2-D sensitivity kernels are employed to account for finite frequency effects. We applied the inversion method to synthesized data obtained from numerical simulations modeling Rayleigh wave propagation over checkerboard structures. We found the method can almost completely recover the input checkerboard structure when the size of anomalies is larger than one wavelength. When the size of anomalies is about half the wavelength,

we still can recover the pattern of variations of phase velocities, but the magnitude of anomalies is underestimated. Surface wave amplitude contains important information about Earth structure and should be inverted together with phase data in surface wave tomography.

In chapter 2, we applied the tomography method developed in chapter 1 to phase and amplitude data of fundamental mode Rayleigh waves recorded at the TriNet network in southern California to invert for phase velocities at periods from 25 to 143 s. A one-dimensional shear wave velocity model based on average phase velocities reveals a pronounced low velocity zone (LVZ) at the depth range from 90 km to 210 km underneath a lithospheric lid. The average shear velocity in the lid is significantly slower than in typical stable continental or oceanic lithosphere and the low velocities in the low velocity zone probably require the presence of melt. Two-dimensional phase velocities are used to invert for three-dimensional S-wave velocities of the upper mantle. The pattern of velocity anomalies indicates that there is active small-scale convection in the asthenosphere beneath southern California and that the dominant form of convection is 3-D lithospheric drips and asthenospheric upwellings, rather than 2-D sheets or slabs. Several of the features we observe have been previously detected by body wave tomography, including delaminated lithosphere and consequent upwelling of the asthenosphere beneath the eastern edge of the southern Sierra Nevada and Walker Lane region; sinking lithosphere beneath the southern Central Valley;

upwelling and low velocity anomalies beneath the Salton Trough region; and downwelling beneath the Transverse Ranges. Our new observations provide better constraints on the lateral and vertical extent of these anomalies. In addition, we detect two previously undetected features: a high velocity anomaly that probably represents delaminated lithosphere beneath the northern Peninsular Range and a low velocity anomaly that may be caused by dynamic upwelling beneath the northeastern Mojave block. Azimuthal anisotropy is obtained in a joint inversion including lateral variations of phase velocities. The strength of anisotropy is $\sim 1.7\%$ at periods shorter than 67s and decreases to $\sim 1\%$ at longer periods. With the measurements of shear-wave splitting time from other studies, we estimated the thickness of anisotropy is about 350 km. The fast direction is nearly W-E, which is consistent with shear wave splitting measurements. The W-E fast feature is attributed partially to the N-S compressive stress in the lithosphere and partially to the asthenospheric flow at depth.

In chapter 3, we invert phase and amplitude data of Rayleigh waves recorded at ocean-bottom seismometers (OBSs) in very young (less than 10 Ma) seafloor in two arrays near the East Pacific Rise, the MELT array and the GLIMPSE array, for shear wave velocity (V_s) and attenuation (Q_u). The finite-frequency scattering of surface waves due to elastic heterogeneities is taken into account with 2-D sensitivity kernels. The scattering effects on surface wave amplitude can be separated from the attenuation effects on amplitude, which is not accurately accounted for in previously regional

attenuation studies. A high velocity lid with negative gradient in the uppermost mantle overlying a low velocity zone is observed in both regions. The highest velocity in the high velocity lid reaches 4.4 km/s. The minimum of shear wave velocity in the low velocity zone is ~ 4.0 km/s. Our Q_u models exhibit a sharp change over the depth range of 40 to 60 km with higher values above 40 km. The change of Q_u and S-wave velocity with depth is partly due to the sharp change of water content in the upper mantle as a result of the extraction of water by large fractional melting above ~ 65 km. Anelasticity effects on seismic velocities from attenuation are not enough to explain the observed low velocity zone. $\sim 1\%$ partial melting in the low velocity zone is required to satisfy the minimum value of shear wave velocity. The combined model with partial melt in the depth range between the 'dry' solidus and 'wet' solidus and dehydration of peridotite above the 'dry' solidus explain the origin of observed low velocity zone. Our seismic observations provide strong constraints on the argument that the structure of oceanic plates is controlled by compositional as well as thermal parameters.

Acknowledgements

It is very fortunate for me to study in such a great department with so many excellent professors and talented students for the past five years. I would like to take this opportunity to express my gratitude to those who teach, help and support me in both study and life in Brown.

First and foremost, I want to thank my advisor Don Forsyth, who guided me through all the difficulties in my research and provided me tremendous supports and ideas about how to solve scientific problems and how to be a professional geophysicist. I benefited greatly from his endless knowledge and patience. His passion and persistence in science imprint in my mind and will inspire me in my future scientific career.

I would like to thank Karen Fischer and Marc Parmentier, who taught me so much in class that broaden my knowledge in geosciences. Marc's clear and elegant explanations of geophysical problems in class impressed me deeply. Karen gave me a lot of help and advices in my research and future career. I am also grateful to Yan Liang and Terry Tullis, who taught me mineralogy and advance structural geology and gave me a lot of comments and suggestions about my research. I would like to thank Goran Ekstrom for sparing his time reading my thesis and being on my final examination committee.

I feel so fortunate to have spent my graduate years with many great students in the geological department. Dayanthie Weeraratne provided a lot of help and advices for my

research. She taught me a lot of things about American culture and language. Zhonghui Liu provided me temporary accommodation when I first came to a new country and helped me through the first tough semester in Brown. I enjoyed the cruise in southern Pacific with Nick Harmon and Catherine Rychert, who brought many delightful memories to me. I had great time talking with Sarah Zaranek, Amandine Cagnioncle and David Abt, who gave me a lot of chance to speak English during the busy school days.

I would also like to thank Bill Collins and Margaret Doll for assisting me in using PC, workstations and printers. Whenever I encountered problems in computer, they always provided kind helps and tried very hard to solve it. Without their supports in computer, my research will never be done.

I would like to thank a number of people outside geological department in Brown for their friendship and help during my past five years: Shougang Wang, Xipeng Liu, Zhen Zhou, Hongjie Wang, Weiye Li, Zhengwen Li and Kunquan Yu.

Finally, I would like to thank my parents for their continuous encourage and support. Even though I was away from them for many years, their image of hard working and persistence drove me to work hard day and night and to achieve what I have done today.

Table of Contents

Signature page	ii
Vita	iii
Preface	v
Acknowledgements	ix
Table of Contents	xi
Chapter 1: Regional tomographic inversion of amplitude and phase of Rayleigh waves with 2-D sensitivity kernels.....	1
Summary.....	2
Introduction.....	3
Theory of finite-frequency properties of surface waves.....	5
Accuracy evaluation of 2-D sensitivity kernels.....	8
Wavefields comparison with calculation based on 2-D sensitivity kernels.....	10
Surface wave inversion.....	15
Resolution evaluation.....	15
Importance of amplitude in surface wave tomography.....	19
One-plane wave versus two-plane wave.....	21

Discussion and conclusion.....	24
References.....	25
Figure Captions.....	28
Figures.....	32
Chapter 2: Rayleigh wave phase velocities, shear wave structure and azimuthal anisotropy beneath southern California.....	45
Abstract.....	46
Introduction.....	47
Data correction and processing.....	52
Methodology of surface wave tomography.....	57
Isotropic phase velocity.....	61
Average shear wave velocity structure.....	66
Crustal structure.....	71
Upper mantle anomalies and small-scale convection.....	75
Delamination beneath the Sierra Nevada.....	75
Upwelling beneath Salton Trough.....	81
Lithospheric drips beneath the Transverse Range.....	82

Thin crust and cool lithosphere beneath the Borderlands.....	84
Peninsular Range drip and Mojave upwelling.....	85
Azimuthal anisotropy.....	88
Conclusions.....	95
References.....	97
Figure captions.....	108
Figures.....	112
Chapter 3: Seismic velocity and attenuation constrains on the formation of oceanic plate and the origin of the low-velocity zone.....	128
Abstract.....	129
Introduction.....	130
Methodology and data acquisition.....	134
Attenuation coefficients and phase velocities.....	138
Models for the origins of the LVZ.....	145
Model prediction of shear velocity and attenuation.....	148
Results and discussion.....	149
Conclusions.....	156

References.....	158
Figure captions.....	163
Figures.....	166
Appendix: Improving epicentral and magnitude estimation of earthquakes from T phases by considering the excitation function.....	177
Abstract.....	178
Introduction.....	179
MELT OBS array.....	182
T phases recorded by the OBSs.....	183
Empirical model.....	185
Evaluation of the Empirical model.....	187
Comparison between T phase and surface-wave relative locations.....	190
A comparison between T-phase maximum amplitude and earthquake magnitude.	192
T-phase excitation.....	196
Multiple-reverberation seafloor scattering.....	200
Numerical simulation.....	201

Synthetic envelope.....	204
Summary	207
Acknowledgments.....	208
References.....	208
Figure captions.....	213
Figures.....	218

Chapter 1

Regional tomographic inversion of amplitude and phase of Rayleigh wave
with 2-D sensitivity kernels

Yingjie Yang and Donald W. Forsyth

Department of Geological Sciences

Brown University

Providence, RI 02912

Submitted to *Geophysical Journal International*

June 7, 2005

Summary

In this study, we test the adequacy of 2-D sensitivity kernels for fundamental-mode Rayleigh waves based on the single-scattering (Born) approximation to account for the effects of heterogeneous structure on the wavefield in a regional surface wave study. The calculated phase and amplitude data using the 2-D sensitivity kernels are compared to phase and amplitude data obtained from seismic waveforms synthesized by the pseudo-spectral method for plane Rayleigh waves propagating through heterogeneous structure. We find that the kernels can accurately predict the perturbation of the wavefield even when the size of anomaly is larger than one wavelength. The only exception is a systematic bias in the amplitude within the anomaly itself due to a site response.

An inversion method of surface wave tomography based on the sensitivity kernels is developed and applied to synthesized data obtained from a numerical simulation modeling Rayleigh wave propagation over checkerboard structure. By comparing recovered images to input structure, we illustrate that the method can almost completely recover anomalies within an array of stations when the size of the anomalies is larger than or close to one wavelength of the surface waves. Surface wave amplitude contains important information about Earth structure and should be inverted together with phase data in surface wave tomography.

Introduction

In traditional surface wave tomography, ray theory is assumed to resolve heterogeneities of lithosphere and upper mantle with the great-circle ray approximation (e.g., Woodhouse & Dziewonski, 1984; Trampert & Woodhouse 1995; van der Lee & Nolet 1997) or by tracing rays through a heterogeneous earth model. However, ray theory is only valid when the scale of heterogeneities is much larger than the wavelength and the width of the Fresnel zone. This theoretical limitation calls into question the ability to discover small-scale structure using surface wave tomography based on ray theory even with the fast-growing abundance of seismic data. When the length scale of heterogeneities is comparable to the wavelength, the sensitivity of surface waves to heterogeneous structure off the ray path is significant and finite frequency effects should be taken into account. In recent years, the finite-frequency properties of surface waves have been considered in a number of global surface wave tomography studies (Clevede et al. 2000; Spetzler *et al.* 2002, Ritzwoller et al. 2002; Yoshizawa & Kennett 2002, Zhou et al. 2004).

However, in regional teleseismic surface wave tomography, the conventional two-station method is still widely used. Phase travel times along great-circle paths between many pairs of stations are combined to find 2-D local phase velocities. Surface wave amplitude has not been included in these inversions due to complicated effects such as multi-pathing, focusing/defocusing and attenuation. In regional tomography, the length scale of structures we are interested in is often comparable to the wavelength or even

smaller than the wavelength, which urges us to consider finite frequency effects. To represent the effects of scattering of waves outside the regional array, Forsyth and Li (2004) developed a method that represents an incoming wave with the interference of two plane waves. For each plane wave, a Gaussian sensitivity function was utilized to represent the finite width of the response of surface waves to structure along the ray path. The interference of two plane waves can often represent well the character of non-planar incoming waves caused by multi-pathing and scattering with far fewer parameters than the more general approach of Friederich and Wielandt (1995), thus providing more stability in the inversion for velocity variations within the array. However, the Gaussian sensitivity function, which assumes the sensitivity is equal along the ray path and decays as a Gaussian function in the direction perpendicular to ray path, does not describe the sensitivity accurately.

In this study, we use the kernels derived by Zhou et al. (2004) to represent the sensitivity of surface waves to structure. By comparing with numerical simulation, we evaluate the accuracy of the sensitivity kernels based on the Born approximation in describing the wavefield variation caused by heterogeneous structure. We develop a regional surface wave tomography method based on the sensitivity kernels and apply the method to synthesized data. Finally, we compare the recovered phase velocity structure with that found from the previous method based on Gaussian sensitivity function.

Theory of finite-frequency properties of surface waves

In traditional surface wave tomography, ray theory is commonly utilized to interpret relative phase shifts along great circle paths in terms of local relative phase velocities. Propagation of a surface wave on the surface of the earth is assumed to be along an infinitely thin ray path. Ray theory is valid when the characteristic scale of heterogeneous structure is much larger than the wavelength. However, when the scale of heterogeneous structure is close to the wavelength or even smaller, finite-frequency effects will be significant and ray theory cannot describe the phase shift accurately. In order to resolve finer heterogeneous structure, we have to take finite-frequency effects into account in surface wave tomography. In 2004, Zhou et al. derived 3-D sensitivity kernels for surface waves based on single-scattering (Born) approximation on the earth surface. The sensitivity kernels are formulated in the form of surface wave mode summations for measured phases and amplitudes. For the single-frequency case, phase and amplitude variations, $\delta\phi(\omega)$ and $\delta \ln A(\omega)$, in a perturbed earth model relative to the reference earth model can be expressed as following:

$$\delta\phi(\omega) = \iiint_{\oplus} K_{\phi}^m(x, \omega) \delta m(x) d^3x, \quad \delta \ln A(\omega) = \iiint_{\oplus} K_A^m(x, \omega) \delta m(x) d^3x, \quad (1)$$

where δm is shorthand for $\delta\alpha/\alpha, \delta\beta/\beta, \delta\rho/\rho$, and $K_{\phi}^m(x, \omega)$ and $K_A^m(x, \omega)$ are the phase and amplitude sensitivity kernels respectively.

Furthermore, they show that by using the forward-scattering approximation and neglecting mode-coupling effects, the 3-D sensitivity kernels, expressing the sensitivities to 3-D perturbations in density, shear wave velocity and compressional wave velocity,

can be combined to form 2-D sensitivity kernels expressing the sensitivities to the local phase velocity perturbation, $\delta c/c$. The 2-D sensitivity kernels are defined as:

$$\delta d = \iint_{\Omega} K_d^c(r, \omega) (\delta c/c) dx^2, \quad (2)$$

where the integration is over the earth's surface. δd is shorthand for the phase delay, $\delta\phi$, or the relative amplitude variation, $\delta \ln A$, with corresponding phase kernel $K_\phi^c(r, \omega)$ or amplitude kernel $K_A^c(r, \omega)$.

In regional surface wave array tomography using teleseismic sources, incoming waves are generally regarded as plane waves when propagating through a study region with maximum dimensions of hundreds of kilometers. The sensitivity kernels for a plane wave can be simplified as,

$$K_\phi^c(r, \omega) = \text{Im} \left(\frac{k^2 R'' e^{-i[kx'' - k\Delta x + \pi/4]}}{R \sqrt{\pi/8} k x''} \right), \quad (3)$$

and

$$K_A^c(r, \omega) = -\text{Re} \left(\frac{k^2 R'' e^{-i[kx'' - k\Delta x + \pi/4]}}{R \sqrt{\pi/8} k x''} \right), \quad (4)$$

where k is wavenumber of surface waves, x'' is the distance from scatterer to receiver and Δx is the differential propagating distance between the direct incoming wave arriving at the receiver and the wave arriving at the scatterer (Fig. 1); R and R'' are receiver polarization vectors for direct incoming waves and scattered waves respectively. Since we use the vertical component of Rayleigh waves in this study, the receiver vectors R and R'' are equal.

The sensitivity kernels in eqs. (3) and (4) are formulated for single-frequency observables of phase and amplitude from unwindowed seismograms in the time domain. The 2-D geometry of the single-frequency sensitivity kernels depends on wave frequency and reference phase velocity. In realistic data processing, Rayleigh waves are isolated from observed seismograms by applying proper time windows to the seismograms. The windowing of seismograms in the time domain is equivalent to smoothing the spectrum in the frequency domain. Thus the sensitivity kernels for windowed seismograms will be the integral of sensitivity kernels over a range of different frequencies centered at the frequency of interest. An example of sensitivity kernels for a waveform at the period of 50 s windowed using a 300 s window with a half cosine taper of 50 s on each end is shown in Fig. 2. In the inverse method we describe later, we interpolate velocities between nodal points with a 2-D Gaussian averaging function, thus implicitly restricting the scale of heterogeneities allowed through the characteristic length of the Gaussian filter. Here we also smooth the sensitivity kernels with a 2-D Gaussian function to represent the distributed effects of any perturbation in the value of a node. In the example shown, we use a characteristic $1/e$ fall off distance of 50 km. The receiver is located at the origin (0,0) and a plane Rayleigh wave propagates from left to right as indicated by the arrow. Obviously, the sensitivity is not limited to the ray path as is assumed in traditionally linearized ray tomography. The sensitivity kernels have a broad distribution and become broader with increasing distance from the station along the ray path. The sensitivity is mainly concentrated in the region of the first two Fresnel zones, and quickly

decreases in the higher-order Fresnel zones, due to the interference between sensitivity kernels for different frequencies and the Gaussian smoothing. The magnitude of sensitivity is much larger in the area close to station than in the area away from station, which helps us to obtain high spatial resolution of phase velocity in regional tomography.

Accuracy evaluation of 2-D sensitivity kernels

One of our primary goals in this paper is to evaluate how accurately the 2-D sensitivity kernels based on the Born approximation can represent wavefield variations caused by finite amplitude heterogeneities with dimensions on the order of a wavelength. In this section, we will evaluate this accuracy by comparing with numerical simulation.

Numerical simulation

The numerical simulation method we adopt to simulate surface wave propagation is a pseudo-spectral method developed by Hung and Forsyth (1998). This method solves a velocity-stress formulation of the elastic wave equation. Spatial variations of velocity and stress fields propagating in heterogeneous media are calculated by high-accuracy Fourier series in horizontal directions and by a Chebyshev differential operator in the vertical direction. A fourth-order Runge-Kutta method is used to represent time marching of wavefields. The computation programs are run in a high-performance parallel computer at the Technology Center for Advanced Scientific Computing and Visualization at Brown University.

In simulating Rayleigh wave propagation, we do the simplest case with a 2-D

variable media in 3-D model space, that is, medium parameters are uniform in the vertical direction. We discretize a model space into a $288 \times 288 \times 64$ grid with grid spacing of 20 km in the horizontal directions and an average of 10 km vertically. Thus the model space is 5740 km in the horizontal direction and 630 km in the vertical direction. Absorbing boundary conditions are applied at the sides and bottom of the model space. Isotropic medium properties are specified with P-wave velocity 8 km/s, S-wave velocity 4.5 km/s and density 3.3 kg/m^3 . An inclusion cylinder is centered at the grid point of (2600 km, 2600 km) with radius of 100 km. In the interior of the inclusion cylinder, both P-wave and S-wave velocity are increased by 5%, while density remains the same. Thus the corresponding phase velocity is increased by about 5% as well. Rayleigh wave phase velocities calculated analytically (Saito, 1988) for 1-D media are 4.15 km/s in the exterior and 4.36 km/s in the interior of the inclusion cylinder. As shown in Fig.3, an initial plane Rayleigh wave propagates past the cylindrical anomaly from left to right, starting at 1000 km. The form of the starting wave is determined by first propagating waves for several thousand km from a point source in a homogenous model, then filtering and windowing to isolate the velocity and stress fields of the Rayleigh waves. 1891 “stations” are placed in each grid node to record particle motion in a neighboring subarea of $1200 \text{ km} \times 600 \text{ km}$ surrounding the inclusion cylinder. In the example shown in figure 4, the seismograms recorded at each station are filtered using a band-pass filter with 10 mHz width centering at frequency of 40 mHz and windowed using the same time window as that used to calculate the sensitivity kernels, i.e., 300 s length with 50 s cosine taper. The

filtered and windowed seismograms are transformed into the frequency domain to obtain phase and amplitude data. Thus in this example, we study scattering of surface waves with wavelength about 100 km propagating over a heterogeneous structure with scale about twice the wavelength. Since horizontal components are strongly influenced by higher mode Rayleigh waves and Love waves, we only consider the vertical components here.

In order to reduce the numerical errors introduced by the 3-D pseudo-spectral method, we do an additional simulation with the same model space but having uniform medium properties. In theory, for this uniform media, amplitude should be identical anywhere on the surface. However, due to numerical inaccuracy in representing the wave, there are some slight variations in amplitude that are a systematic function of position within the grid. In order to reduce this inaccuracy in representing the wave, we subtract the phase and amplitude data in the uniform case from those in the case with the inclusion cylinder. The retrieved phase and amplitude are the scattered phase and amplitude data caused by the included cylinder.

Wavefield comparison with calculation based on 2-D sensitivity kernels

With the same model space and station configuration as that in the numerical simulation, we also calculate the scattered phase and amplitude caused by the inclusion cylinder using 2-D sensitivity kernel, eqs. (2), (3) and (4), for windowed Rayleigh waves at period of 40 mHz. This calculation based on 2-D sensitivity kernels only considers

scattering of fundamental mode Rayleigh wave onto itself using a far-field approximation, whereas the numerical simulation includes all higher mode excitation and near-field terms. Friederich et al. (1993) have shown that the contribution of higher modes to the overall wavefield is negligible for a cylindrical structure situated in the center of a homogenous structure. Thus we can approximately regard the simulation wavefield as a fundamental mode surface wave wavefield, and compare the wavefield based on 2-D sensitivity kernels directly with that from the numerical simulation.

In Fig. 4, we show the scattered wavefields in terms of phase and amplitude for period of 25 s based on the numerical simulation (Fig. 4a, 4b) and the 2-D sensitivity kernels (Fig. 4c, 4d, 4e, 4f). The circle represents the inclusion cylinder. Overall scattering patterns are very similar behind the cylindrical scatterer except that the extreme values in the focusing region at large distance are slightly overestimated by the scattering kernels and the width of the Fresnel zone is slightly underestimated (Fig.5c), probably because there is a slight mismatch between the shape of spectrum for the simulation and that assumed in the sensitivity kernels.

In the neighboring area of the circle, the difference of wavefields becomes larger. Fig. 5a and 5b shows that amplitude and phase estimated from the scattering kernels are significantly different from the numerical simulation on a profile just past the heterogeneity. The difference is probably the result of the forward scattering approximation used in calculating the sensitivity kernels. The forward scattering approximation assumes scattering magnitude is the same in all directions. In reality,

scattering is direction-dependent and determined by the perturbation of medium parameters, $\delta\alpha, \delta\beta, \delta\rho$. The scattering pattern at different depths can be calculated according to the formula (29d) in Snieder (1986). The Rayleigh wave at an individual period is sensitive to earth structure over a range of depths. The largest sensitivity to shear velocity perturbations is located at a depth of about one third of the wavelength. Fig. 6 shows the radiation pattern of scattering at a variety of depths over the primary sensitivity range for Rayleigh waves with period of 25 s, assuming that the medium is a Poisson solid. We note that the patterns over this range of depths are similar in the forward direction, and there is some difference in the backward direction. If we intend to get the exact sensitivity to perturbations of local phase velocities, we need to do a numerical integral of scattering coefficients over depth, which requires prior knowledge of the form of the perturbations in elastic parameters in a forward model and will introduce cumbersome computations. Thus, as an approximation, we use the scattering pattern at the most sensitive depth as the overall scattering pattern when calculating sensitivity kernels considering scattering coefficients.

Fig. 4e and 4f show the wavefield calculated using 2-D sensitivity kernels including the scattering pattern. This wavefield matches the scattered wavefield from numerical simulation better than those calculated using kernels without scattering pattern, especially in the region close to the circle, which is obvious in the cross-sections in Fig. 5. For cross-sections right behind the circle, both amplitude and phase calculated with sensitivity kernels and anisotropic scattering pattern (dashed line) fit the numerical

simulation (bold line) almost completely. For the cross-sections far away from the scatterer, there is only a small difference between the isotropic scattering (thin solid line) and angle-dependent scattering (dashed line), which is expected since the scattering angle from the forward direction is very small for stations far behind the cylindrical scatterer.

In 1993, Friederich et al. showed that multiple scattering is superior to the single-scattering method if the scattering region is bigger than one wavelength. In our case, the scatterer is almost twice as large as the wavelength for 25 s. Thus we expected that multiple scattering would introduce significant contribution to the wavefield. However our calculation shows that the multiple scattering introduces only a very small amplitude effect, which is negligible compared to the overall scattering amplitude with a 5% velocity perturbation. The possible reason for the large difference of amplitude between the single and multiple scattering in Friederich's study may be that they do not consider radiation pattern of scattering. As shown in Fig. 5, the isotropic single scattering (dotted line) predicts bigger amplitude right behind the circle than numerical simulation (solid line), which is similar to the observed difference between the single scattering and numerical calculation in their paper. Thus we conclude that the single scattering method with non-isotropic scattering pattern is relatively accurate even for structure bigger than one wavelength, and multiple scattering is negligible for this simple example. Single scattering is linear with respect to phase velocity perturbation, which allows us to invert phase velocity with a linear inversion algorithm.

We also note that the amplitude calculated from scattering kernels inside the circle

is generally larger than those from the numerical simulation. Three cross-section profiles of amplitude and phase at the longitudinal profile through the center of the circle and 20 km from the center in either direction respectively are shown in Fig.7. The predicted phase matches the numerical simulation very well except for a small discrepancy in the middle of the circle. The amplitude is systematically higher than the numerical simulation solution inside the circle, but agrees closely with the numerical simulation solution outside the circle along all three profiles. The reason for the amplitude mismatch when anisotropic kernels are employed is primarily the station site responses in the numerical simulation that are neglected in the 2-D sensitivity kernels. When isotropic scattering is assumed, the discrepancy inside the anomaly is even greater due to an overestimation of the intensity of backscattering (compare Fig. 4a and 4c). Since the phase velocity is about 5% higher inside the circle than outside, the wavelength is about 5% greater, and the vertical energy distribution of Rayleigh waves will be different inside and outside the circle. The anomalous cylindrical structure with higher phase velocity tends to have less energy concentrated at shallow depth than the background media, which leads to smaller amplitude observed at the surface than that predicted using 2-D sensitivity kernels which have no station site response term. In order to demonstrate that this amplitude difference is caused by local structure, we do a numerical experiment in which a plane Rayleigh wave propagates through two uniform structures with 5% percent phase velocity contrast from left to right. A number of stations are placed along a line perpendicular to the medium boundary. We note that the amplitude is about 5 % lower in the higher phase

velocity region than in the lower phase velocity space and the transition of amplitude across the boundary is gradual (Fig. 8). This amplitude variation across the boundary is due to local structure beneath stations, which we call the station site response. In order to take the station site response into account in surface wave tomography, we need an additional amplitude parameter for each station analogous to station static corrections for time delays, except that this site response term will be frequency dependent.

Surface wave inversion

Resolution evaluation

In previous regional surface wave inversions, we approximated scattering effects from heterogeneities outside the vicinity of the array by representing the incoming wave with two interfering plane waves (Forsyth and Li, 2004). The interference of two plane waves produces a sinusoidal variation in amplitude that is a reasonable first-order approximation over an array of limited extent downrange from a scatterer. In the vicinity of the array, phase effects of heterogeneities were considered, but amplitude effects were neglected. Finite frequency effects were approximated with a Gaussian phase sensitivity function along the ray path with characteristic length determined from the width of first Fresnel zone at a distance characteristic of the dimension of the array. The primary disadvantage of this representation of the sensitivity is that it neglects the great increase in phase sensitivity as the Fresnel zone narrows near the receiver. In this study, we continue to represent the effect of distant scatterers with two incoming plane waves, but

represent the effects of finite frequencies for each incoming wave with 2-D sensitivity kernels calculated with the Born approximation. Sensitivity of both phase and amplitude to heterogeneous structure is considered, whereas only phase sensitivity was considered in the previous method. Thus the new method with 2-D sensitivity kernels should improve the spatial resolution of phase velocity greatly.

In order to demonstrate the inversion resolution of the new method based on 2-D sensitivity kernels and compare with the previous method based on Gaussian sensitivity function, we apply both methods to seismic data synthesized using the pseudo-spectral method to invert for phase velocity.

We put a $1000 \text{ km} \times 600 \text{ km}$ subregion in the middle of a model space with dimensions $5740 \text{ km} \times 5740 \text{ km}$. The subregion is a smoothed checkerboard structure with 200 km square anomalies. Both P-wave velocity and S-wave velocity alternate fast and slow anomalies of $\pm 5 \%$. A 60-station network with station spacing 120 km is placed inside the checkerboard structure (Fig.9a). A number of plane waves propagate over the checkerboard structure from different directions with even azimuthal distribution at an interval of 15 degrees. Even though each incoming wave front in this numerical experiment is a single plane wave because there are no external heterogeneities, we can still use the two-plane wave method; the inversion will simply find a solution in which each incoming wave is represented with one main plane wave with large amplitude and a second plane wave with very small amplitude. In the inversion, 6 wavefield parameters are required for each incoming wave, describing the amplitude, initial phase and direction

of propagation of each of the two plane waves. To isolate the fundamental mode Rayleigh waves, the same data processing procedure of filtering and windowing as that used in preceding section are applied to the synthesized seismograms. In the inversion, we parameterize the study region with 273 velocity nodes distributed evenly inside the checkerboard region with spacing 50 km and an additional 152 nodes surrounding the checkerboard to represent some of the effects from outside the array for later experiments. The phase velocity at any point in the study region is represented by a 2-D weighted average of the values at nearby grid nodes using a Gaussian weighting function with 80 km characteristic length. The same function is employed in smoothing the Born sensitivity kernels. We add a multiplicative amplitude correction factor or site response term to be determined for each station. To invert phase and amplitude data for phase velocity at each node, the incoming wavefield parameters and the site terms simultaneously, a standard, iterative, linearized inversion technique (Tarantola and Valette, 1982) is utilized, alternating with a simulated annealing adjustment of the wavefield parameters (Forsyth and Li, 2004). The solution for the general non-linear least-squares problem is

$$\Delta m = \left(G^T C_{nn}^{-1} G + C_{mm}^{-1} \right)^{-1} \left(G^T C_{nn}^{-1} \Delta d - C_{mm}^{-1} [m - m_0] \right) \quad (5)$$

where m_0 is the original starting model, m is the current model, Δm is the change relative to the current model, Δd is the difference between the observed and predicted data for the current model, \mathbf{G} is the partial derivative of \mathbf{d} with respect to perturbation of m , \mathbf{C}_{nn} is data covariance matrix describing the data uncertainties, and \mathbf{C}_{mm} is the prior

model covariance matrix, which acts to damp or regularize the solution. The uncertainties of synthesized data, which are introduced due to the inaccuracy of the numerical simulation, are relatively small compared to a real data set. However, we can approximately regard the synthesized data as a realistic data set by assigning values of data uncertainties in the diagonal terms of C_{nn} that are typical of those found in regional surface wave studies (Li et al. 2003a; Li et al. 2003b; Weeraratne et al., 2004). To damp the underdetermined solution and stabilize the inversion, we employ a prior model covariance of 0.4 km/s for phase velocity parameters. The choice of damping value 0.4 km/s for phase velocity parameters is based on many experiments using a range of damping values from 0.2 km/s to 0.5 km/s by considering the trade-off between the resolution and model uncertainties.

The resultant phase velocity maps based on the 2-D sensitivity kernels are shown in Fig.9 at periods of 25 s (Fig. 9a), 50 s (Fig.9c) and 100 s (Fig. 9d). One phase velocity map at the period of 25 s based on Gaussian sensitivity function is shown in Fig.9b. For the inversion based on 2-D sensitivity kernels, anomalies of phase velocity are almost completely recovered at the periods of 25 s and 50 s. At the period of 100 s, we still can recover the variation pattern, although the magnitude of anomalies is greatly underestimated. The underestimation in magnitude is partly due to the wide Fresnel zone of long-period surface waves, which decreases the local intensity of the sensitivity functions, and the damping that reduces the amplitude of the anomalies when the sensitivity is low. The primary limitation is not the accuracy of the kernels when the

wavelength is similar to the wavelength of the heterogeneities; it is the increased uncertainty in relative arrival time at longer periods coupled with the decreased local sensitivity. In the absence of noise, damping would be unnecessary and the pattern could be recovered nearly perfectly at all periods. For the inversion based on Gaussian sensitivity function, the pattern of anomalies can only be recovered fairly at the period of 25 s. At longer period, the anomalies are poorly imaged and the primary limitation is the accuracy of the Gaussian representations of the kernels close to the stations.

These inversion experiments demonstrate that inversion based on 2-D single-scattering sensitivity kernels can greatly improve phase velocity resolution compared to that based on Gaussian sensitivity function. The new inversion method can resolve structure on the scale of one wavelength given the distribution of stations and events in the experiment. The improvement in resolution helps us to recover the earth's smaller scale structure.

Importance of amplitude in surface wave tomography

In the above section, we have shown that the new inversion method including both phase and amplitude sensitivities can greatly improve the resolution of phase velocities. In this section, we will evaluate the importance of amplitude information in the inversion for phase velocities and show why we should include amplitude data in surface wave tomography.

Conventional surface wave tomography uses only phase data to invert for phase velocities. Amplitude has been long neglected in tomography since amplitude is affected

by many different factors, such as scattering, attenuation, station response and local structure. It is hard to estimate all the different effects in tomography with ray theory. However amplitude contains important information about earth structure and should be combined with phase data to better constrain earth structure. As demonstrated in a previous section, amplitude variations caused by scattering can be estimated accurately by the amplitude sensitivity kernel when Rayleigh waves propagate over inhomogeneous structure. Anelastic effects on amplitude are not considered here, since we can model surface wave propagation only in elastic media using the pseudo-spectral method. However the anelastic effect, i.e. attenuation, can be estimated easily in tomography according to the propagation distance of individual wave rays and the effects are relatively small in an array of limited extent.

We invert phase and amplitude data separately for phase velocity perturbation using the appropriate sensitivity kernels. Model parameters and the inversion scheme are the same as in the combined inversion described in the previous paragraphs. Inversion results are shown in Fig.10 at period of 50s in comparison to the combined inversion. Inversion using only amplitude data or phase data can recover the variation pattern of anomalies, but the strength of anomalies are not recovered fully in both inversions. If we combine both amplitude and phase data in inversion, the anomalies can be almost perfectly recovered with realistic noise levels.

Although amplitudes clearly do not provide information about the absolute velocity, they appear to contain equivalent information as phase about perturbations in earth

structure. Phase or amplitude alone does not provide complete resolution, given realistic estimation of noise levels. In the real earth situation, when a Rayleigh wave propagates along the ray path from source to receiver, it will be affected by heterogeneous structure off the ray path. The ray path may deviate from the great circle due to multi-pathing and scattering, leading to change of the direction of propagation and the presence of a non-planar incoming wavefield. In order to obtain the structural phase velocity, the non-planar incoming wavefield stemming from heterogeneities outside seismic array must be accounted for using both phase and amplitude information.

One-Plane wave Versus Two-Plane wave

Wielandt (1993) has shown that the inaccurate representation of incoming wavefields could bias the resolved phase velocity systematically from the real phase velocities. Friederich and Wielandt (1995) developed a method that can simultaneously solve for phase velocity variations within an array region and the incoming wavefield for each event. The incoming wavefields are represented by a series of basis functions in the form of Hermite-Gaussian functions. However due to many parameters used to represent the incoming wavefields, with this method it is hard to resolve relatively small changes in the wavefield associated with variation in phase velocity within the study area. In order to simplify the representation while taking into account the primary effects of non-planar energy, Forsyth and Li (2004) developed a two-plane-wave method, which uses two plane waves coming with different incoming directions to represent the variation of wavefield. This method has been used to represent incoming surface waves in several

regional surface wave tomography studies (Forsyth et al. 1998; Li et al. 2003a; Li et al. 2003b; Weeraratne et al., 2004). Here we intend to illustrate the advantage of the two-plane-wave method in representing the wavefield and resolving phase velocity by numerical experiments

We create a spatial model that has the same dimensions as that in preceding checkerboard experiment. A checkerboard structure is placed in the middle of the model space, and outside the checkerboard a random medium is constructed with characteristic scale about 100 to 200 km (Fig.11). The strongest velocity anomalies in the random media are $\pm 5\%$ and the velocities of P-waves and S-waves change simultaneously with same percentage. In order to illustrate the influence of outside heterogenous structure on the wavefield, we compute two kinds of wavefields just as Friederich et al. (1994) did in their study: one without local checkerboard structure, i.e. local structure is uniform, the other with local checkerboard structure. We show one example with a plane wave incident from the bottom of the diagram beginning at a distance of about 1500 km from the edge of the checkerboard. Amplitude is retrieved from stations put at each grid point and is shown in Fig. 12 at a period of 25 s. First, we can see that broad features of the amplitude distribution are similar for both cases with local checkerboard or without checkerboard, which implies that amplitude variation is mainly controlled by outside heterogeneities and local structure has a smaller influence on wavefield than the random media outside. Second, the range of amplitude variation is large, from 0.6 to 1.4. If we regard the incoming wave as a single plane wave, no amplitude variation is predicted

inside the local structure in the case without checkerboard, which differs greatly from the real variation (Fig.12b). In the entire 600×1000 km inner region, the non-plane waves can be better approximated with two plane-wave interference, as shown in the following paragraph.

To do inversion for local structure with surrounding random media, we first simulate wavefields propagating from different azimuths. The structure remains the same for all of these wavefields. 24 different wavefields are simulated with uniform azimuthal distribution at 15 degree intervals. The two-plane-wave method with sensitivity kernels from the Born approximation is applied to the phase and amplitude data. Recovered structure is shown in Fig.13 for this case. The variation pattern of phase velocity is well recovered for both periods of 25 and 50 s. The shape of anomalies in some edge blocks is distorted, such as in the lower-right corner, due to the effects of heterogeneous structure just outside the boundary of the checkerboard region. In order to verify the advantage of two plane waves over one plane wave, we also do the same inversion for phase velocities at the period of 25 s regarding each incoming wave as one single plane wave. In both inversions, we include site response terms for each station, and in the single-plane-wave method, the direction of propagation for each event is a variable. By comparing the result of both inversions, we find that two-plane-wave method improves the fit to amplitude and phase data and reduces the rms misfit of both amplitude and phase by about 30%. The two-plane-wave method based on sensitivity kernels can accurately resolve phase velocities within a seismic array even if there are large heterogeneities present outside the

array area that produce amplitude variations larger than the variations associated with local structure, provided there is good azimuthal coverage.

Discussion and Conclusion

We have revised the 2-D Born approximation sensitivity kernels for the global case to that for a regional case with a plane-incoming wave. The 2-D sensitivity kernels for regional cases are used to calculate the scattered wavefield for Rayleigh wave propagation over a cylindrical anomaly. In order to assess the accuracy of 2-D sensitivity kernels in describing the wavefield variation induced by anomalous structure, we use the pseudo-spectral method to numerically simulate the Rayleigh wave propagation and compare it to the calculated wavefield based on sensitivity kernels. We found that 2-D sensitivity kernels with isotropic forward scattering approximation are not accurate enough to estimate the wavefield variations in regions close to anomalies. We can use the radiation pattern of scattering for the heterogeneities of P-wave and S-wave velocities at the depth of greatest sensitivity for Rayleigh waves as the overall scattering pattern to better model wavefield variations. Inside anomalies, the amplitude is significantly affected by local structure, which is not accounted for by the sensitivity kernel. Additional parameters should be introduced for each station in surface wave tomography to account these local structure effects. This local site effect on amplitude contains some information about structure beneath stations and will be studied further in the future.

Based on the 2-D sensitivity kernels, we develop a surface wave tomography method by representing the incoming waves as two plane waves. For each plane wave, the 2-D sensitivity kernels are employed to account for finite frequency effects. We synthesize Rayleigh wave propagation over checkerboard structure and apply the developed method to synthesized data to recover the input checkerboard structure. We found the method can almost completely recover the input structure when the size of anomalies is larger than one wavelength. When the size of anomalies is about half the wavelength, we still can recover the pattern of variations of phase velocity, but the magnitude of anomalies is underestimated. The amplitude of surface waves is important data and contains nearly as much information about the earth structure as phase data. We should combine both amplitude and phase data to constrain incoming wave fields and invert for phase velocity.

References

- Clevede, E., Megnin, C., Romanowicz, B. & Lognonne, P., 2000. Seismic waveform modeling and surface wave tomography in a three-dimensional Earth: asymptotic and non-asymptotic approaches, *Phys. Earth Planet. Int.*, **119**, 37-56.
- Forsyth, D.W. & Li, A., 2004. Array-analysis of two-dimensional variations in surface wave phase velocity and azimuthal anisotropy in the presence of multi-pathing interference, *Seismic Data Analysis and Imaging with Global and Local Arrays*, (A. Levander and G. Nolet, ed.), AGU Geophysical Monograph, in press.

- Forsyth, D.W., Webb, S., Dorman, L., & Shen Y., 1998. Phase velocities of Rayleigh waves in the MELT experiment on the East Pacific Rise, *Science* **280**,1235-1238.
- Friederich, W., Wielandt, E. & Stange, S., 1993. Multiple forward scattering of surface waves: comparison with an exact solution and Born single-scattering methods, *Geophys. J. Int.*, **112**, 264-275.
- Friederich, W., Wielandt,E. & Stange,S., 1994. Non-plane geometries of seismic surface wavefields and their implication for regional surface-wave tomography, *Geophys. J. Int.* **119**,931-948.
- Friederich, W., & Wielandt,E, 1995. Interpretation of seismic surface waves in regional networks: joint estimation of wavefield geometry and local phase velocity. Method and numerical tests, *Geophys. J. Int.* **120**,731-744.
- Hung, S.-H. & Forsyth, D.W., 1998. Modeling anisotropic wave propagation in oceanic inhomogeneous structures using the parallel multi-domain pseudo spectral method, *Geophys. J. Int.*, **133**, 726-740.
- Li, A., D. W. Forsyth and K. M. Fischer, 2003. Shear velocity structure and azimuthal anisotropy beneath eastern North America from Rayleigh wave inversion, *J. Geophys. Res.*, 108, B8, 2362, 10.1029/2002JB002259.
- Li, A., D. W. Forsyth and K. M. Fischer, 2004. Rayleigh wave constraints on shear-wave structure and azimuthal anisotropy beneath the Colorado Rocky Mountains, AGU Monograph, Lithospheric structure and evolution of the Rocky Mountain region, in press.

- Ritzwoller, M.H., Shapiro, N.M., Barmin, M.P., & Levshin, A.L., 2002. Global surface wave diffraction tomography, *J. Geophys. Res.*, **107**, B12, 10.1029/2002JB001777.
- Saito, M., DISPERS80: A subroutine package for the calculation of seismic normal-mode solutions, *seismological algorithms*, edited by Doornbos, D. J., Academic Press, 293-319, 1988.
- Snieder, R., 1986. 3-D linearized scattering of surface waves and a formalism for surface wave holography, *Geophys. J. R. astr. Soc.*, **84**, 581-605.
- Spetzler, J., Trampert, J. & Snieder, R., 2002. The effects of scattering in surface wave tomography, *Geophys. J. Int.*, **149**, 755-767.
- Tarantola, A., & Valette, B., 1982. Generalized non-linear problems solved using the least-squares criterion, *Rev. Geophys. Sp. Phys.*, **20**, 219-232.
- Trampert, J. & Woodhouse, J.H., 1995, Global phase velocity maps of Love and Rayleigh waves between 40 and 150 seconds, *Geophys. J. Int.*, **122**, 675-690.
- Trampert, J. & Woodhouse, J.H., 2001. Assessment of global phase velocity models, *Geophys. J. Int.*, **144**, 165-174.
- van der Lee, S. & Nolet, G., 1997. Upper mantle S-velocity structure of North America, *J. Geophys. Res.*, **102**, 22815-22838
- Weeraratne, D. S., Forsyth, K. M., Fischer, A. A., Nyblade, 2003. Evidence for an upper mantle plume beneath the Tanzanian craton from Rayleigh wave tomography, *J. Geophys. Res.*, 108, 2427, doi:10.1029/2002JB002273.

Wielandt, E., 1993. Propagation and structural interpretation of non-plane waves,

Geophys. J. Int., **113**,45-53.

Woodhouse, J.H. & Dziewonski, A.M., 1984. Mapping the upper mantle:

three-dimensional modeling of earth structure by inversion seismic waveforms, *J.*

Geophys. Res., **89**, 5953-5986.

Yoshizawa, K. & Kennett, B. L. H., 2002. Determination of the influence zone for surface

wave paths, *Geophys. J. Int.*, **149**,440-453.

Zhou Y., Dahlen, F.A. & Nolet, G., 2004. 3-D sensitivity kernels for surface-wave

observables, *Geophys. J. Int.*, **158**, 142-168.

Figure Captions

Figure 1. The schematic figure of single scattering for a plane surface wave propagating from left to right. x'' is the scatter-receiver distance; y is the perpendicular distance from the scatterer to the direct incoming ray recorded by the receiver; Δx is the differential propagating distance between the direct incoming wave arrived at the receiver and that arrived at the scatterer.

Figure 2. 2-D sensitivity kernels K_c^ϕ, K_c^A for a 20 mHz plane Rayleigh wave. (Top panels) map view of kernels at surface. Black triangles denote receivers; white arrows

indicate the incoming direction of plane Rayleigh waves. (Bottom panels) Cross-section profile of kernels along line AB.

Figure 3. Model space for numerical simulation. Isotropic medium properties are specified with P-wave velocity 8 km/s, S-wave velocity 4.62 km/s and density 3.3 kg/m³. The circle in the middle is a 5% high velocity anomaly. The colored strips in the left indicate the initial wave front of a plane Rayleigh wave on the surface.

Figure 4. Scattered wavefields at 40 mHz by a 5% high velocity cylinder marked with circle. Left panels: scattered amplitude distribution in percentage relative to a uniform wavefield. Right panels: distribution of phase delay time in seconds induced by the cylindrical anomaly. The direction of incidence is from left to right. (a) and (b): scattered wavefields from numerical simulation. (c) and (d): scattered wavefields from calculation based on 2-D sensitivity kernels with isotropic forward scattering approximation. (e) and (f): scattered wavefields from calculation based on 2-D sensitivity kernels with anisotropic scattering pattern as in Fig. 6. The two bold lines in (a) delineate the positions of two profiles along which cross-sections of amplitude and phase delay are plotted in Fig. 5.

Figure 5. Cross-sections of amplitude and phase delay time along two profiles delineated in Fig. 4a. (a) and (b) for the profile at $x = 2700$ km, the very end of the circle; (c) and (d) for the other profile at $x = 3300$ km, 600 km away from the circle. Bold lines represent numerical simulation case; thin solid lines represent the calculation based on sensitivity kernels with isotropic scattering pattern; and dashed lines represent the calculation with

anisotropic scattering pattern (Fig. 6).

Figure 6. Radiation pattern for a scatterer located at the origin. The scattering is fundamental mode to fundamental mode of Rayleigh wave at period of 25 s for P-wave and S-wave heterogeneities, assuming the medium is a Poisson solid. The wave is incident in direction indicated by arrow. Radiation patterns at different depths are represented with different style lines, which are shown in legend. Note that bold line presents the pattern at the most sensitive depth.

Figure 7. Cross-section of amplitude (left panels) and phase delay time (right panels) along three profiles. Middle panels for the profile at the center of the circle, top panels for the profile 20 km left of the center, and bottom panels for the profile 20 km right of the center. Solid lines represent numerical simulation case (Fig. 4a and 4b); dashed lines represent the calculation based on sensitivity kernels with anisotropic scattering pattern (Fig. 4d and 4f).

Figure 8. Amplitude at each station placed along a line perpendicular to the medium boundary. The dashed line indicates the boundary position. Note that amplitude in higher velocity region is smaller, but the transition is not instantaneous. The case shown is for 25 s period with wavelength about 100 km.

Figure 9. Recovered phase velocity maps for checkerboard structure based on the 2-D sensitivity kernels at periods of 25 s (a), 50 s (c) and 100 s (d). For comparison, (b) shows the recovered phase velocity map at period of 25 s based on Gaussian sensitivity function. Black triangles in Fig.9a represent stations put at the surface in numerical simulation for

phase velocity inversion.

Figure 10. Recovered phase velocity maps at period of 50 s. (Top) inversion with phase data alone; (Middle) inversion with amplitude data alone; (Bottom) inversion with both amplitude and phase data.

Figure 11. Constructed model space with random phase velocity. A checkerboard structure is emplaced in the middle delineated by a rectangle. The strongest velocity anomaly of random medium is 5% and the typical scale of anomalies is about 100 to 200 km.

Figure 12. Amplitude distribution from numerical simulation for structure shown in Fig.11. The displayed area is the rectangular region in Fig. 11. The direction of wave incidence is from bottom of diagram to top. Left panel shows amplitude distribution without included checkerboard structure; right panel shows amplitude distribution with included checkerboard structure.

Figure 13. Recovered phase velocity maps for checkerboard structure with surrounding random media shown in Fig. 11 at periods of 25 s (a) and 50 s (b).

.

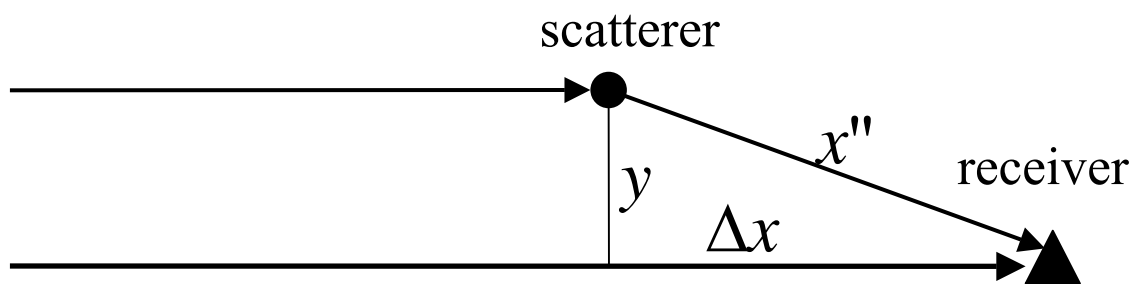


Figure 1

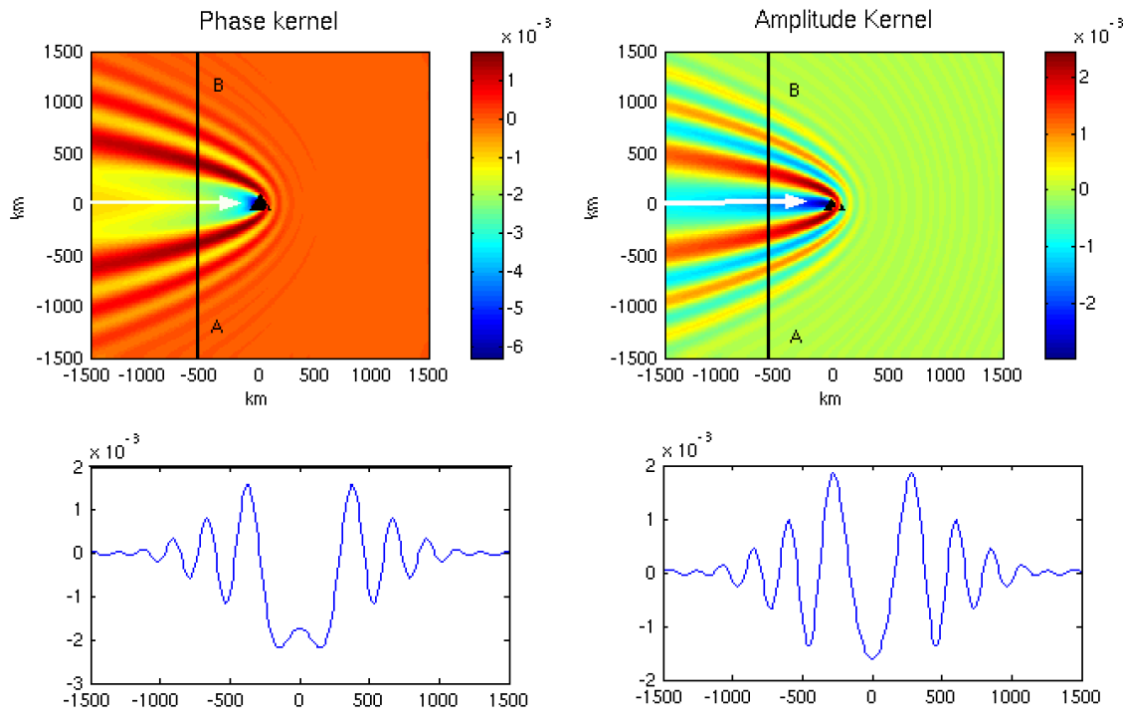


Figure 2

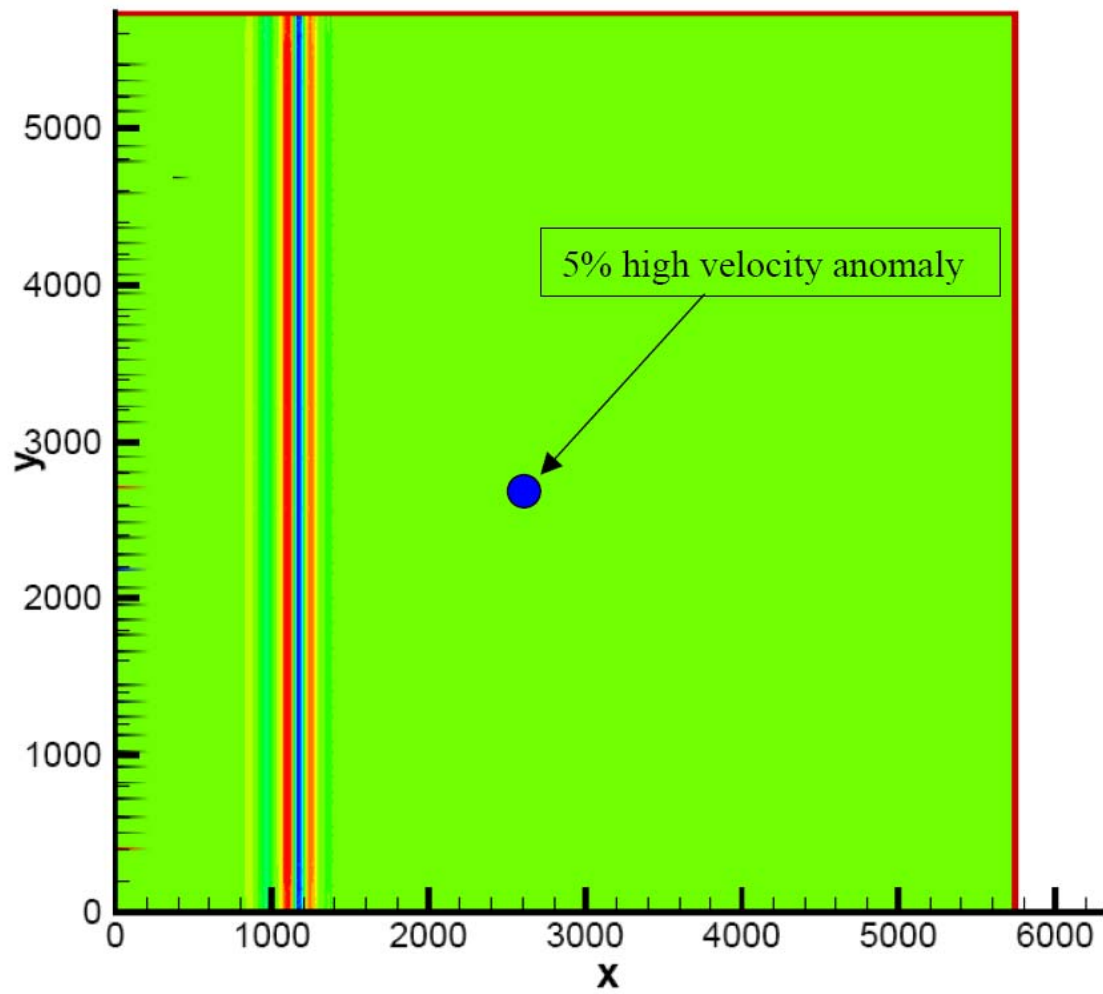


Figure 3

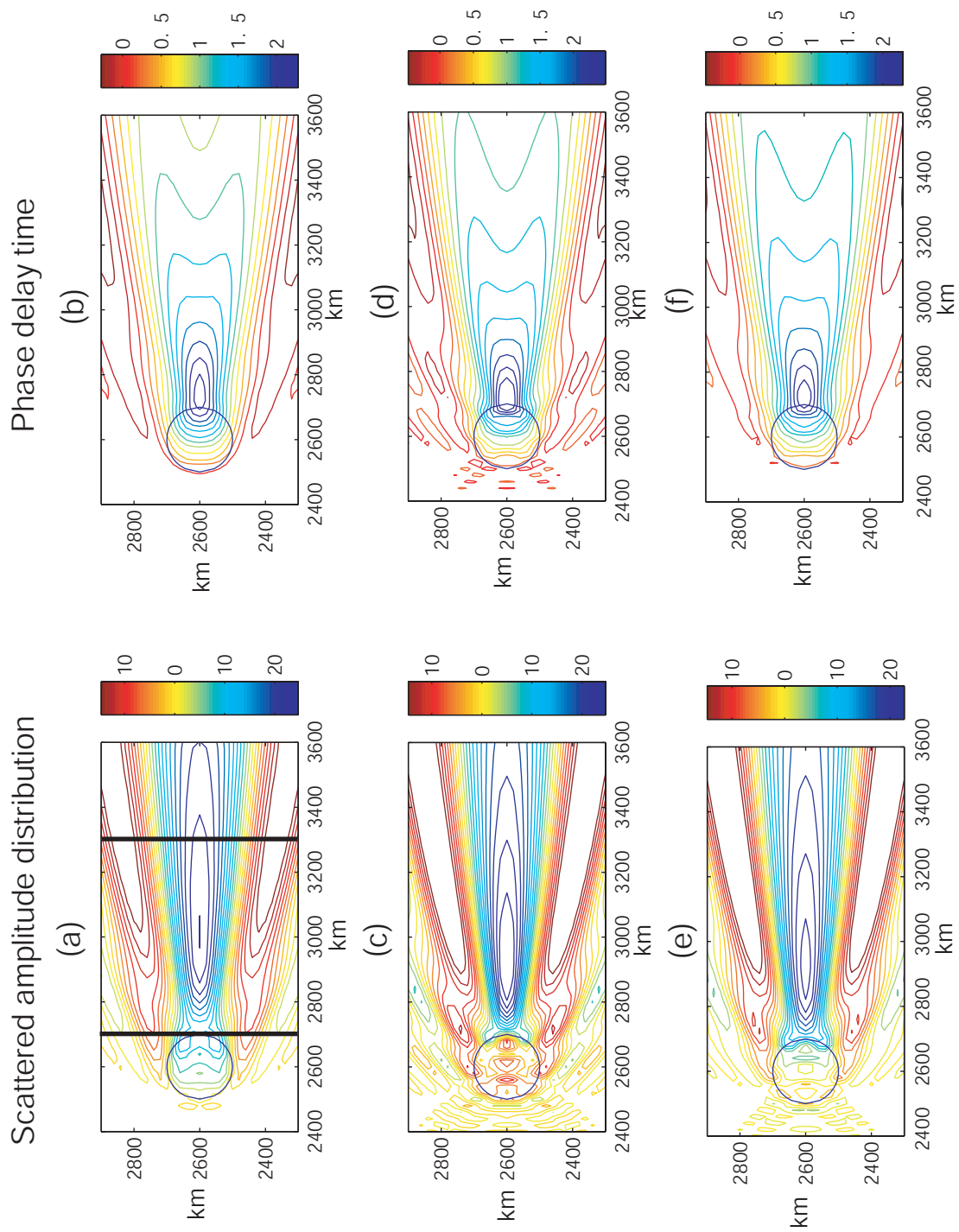


Figure 4

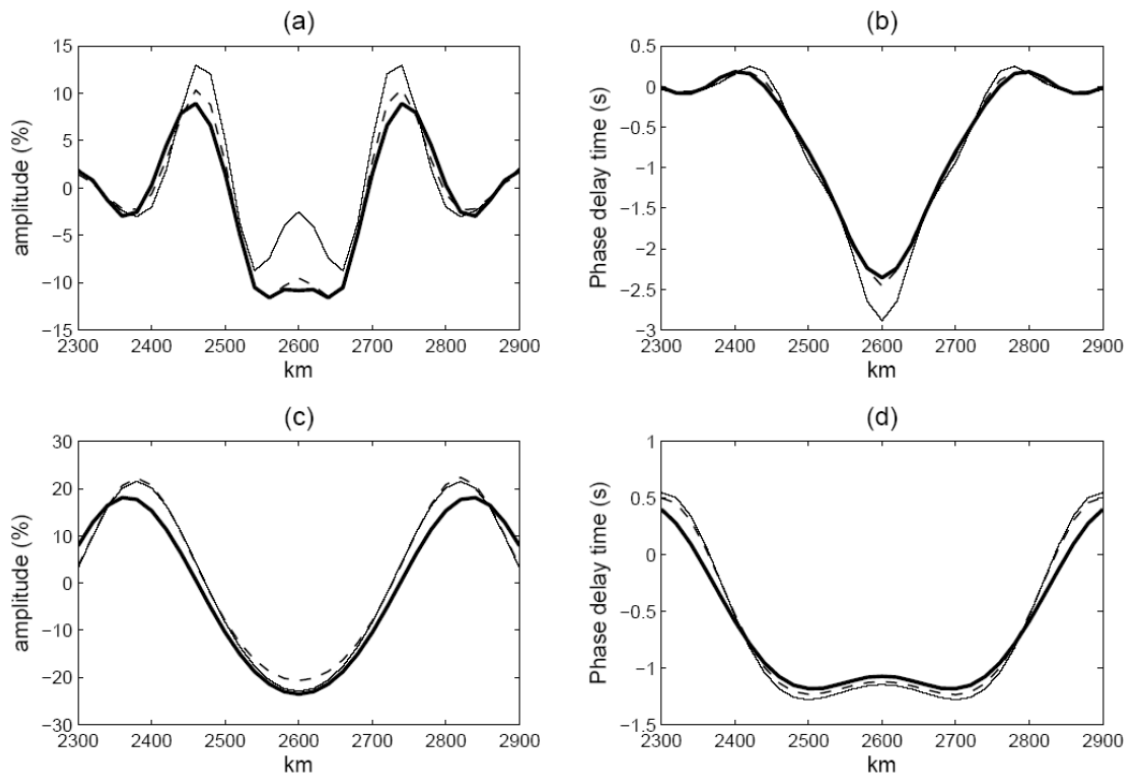


Figure 5

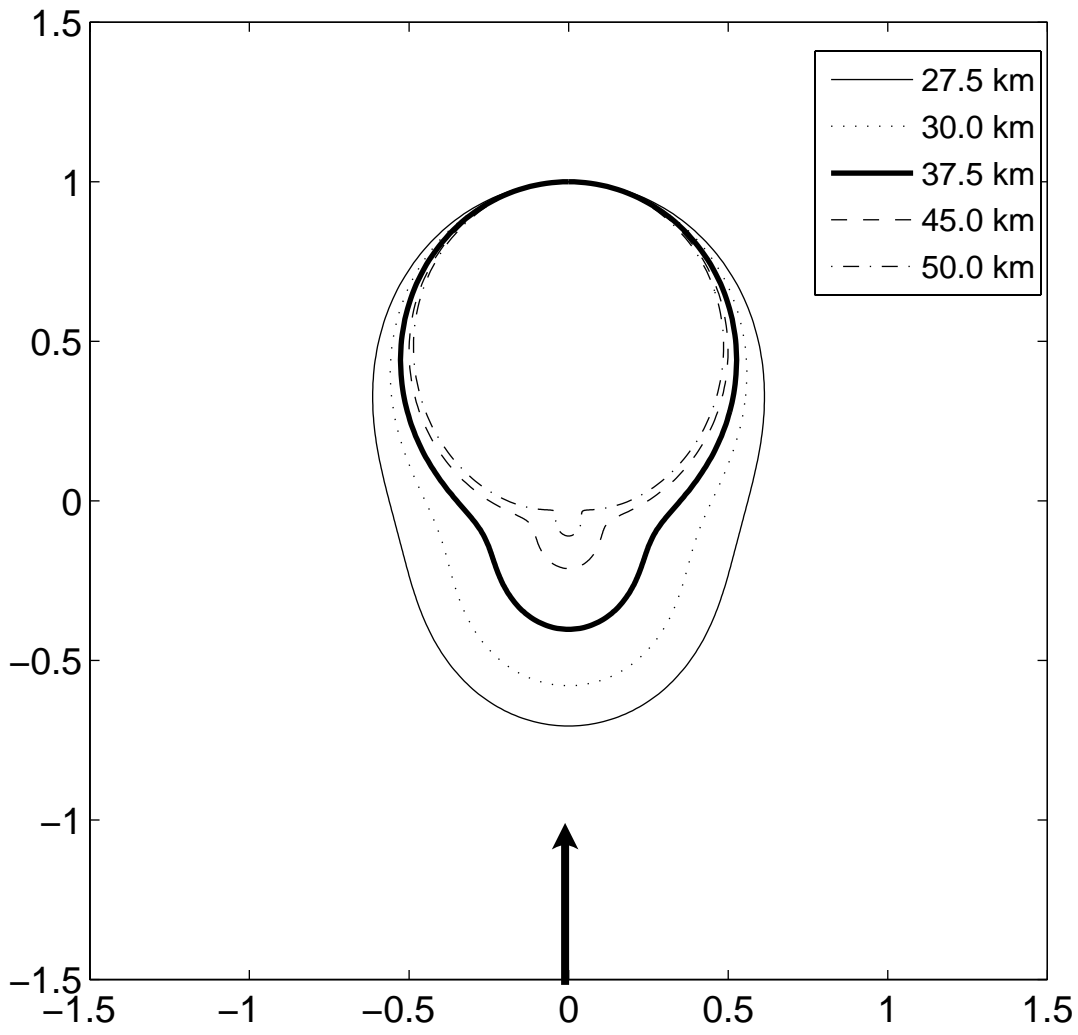


Figure 6

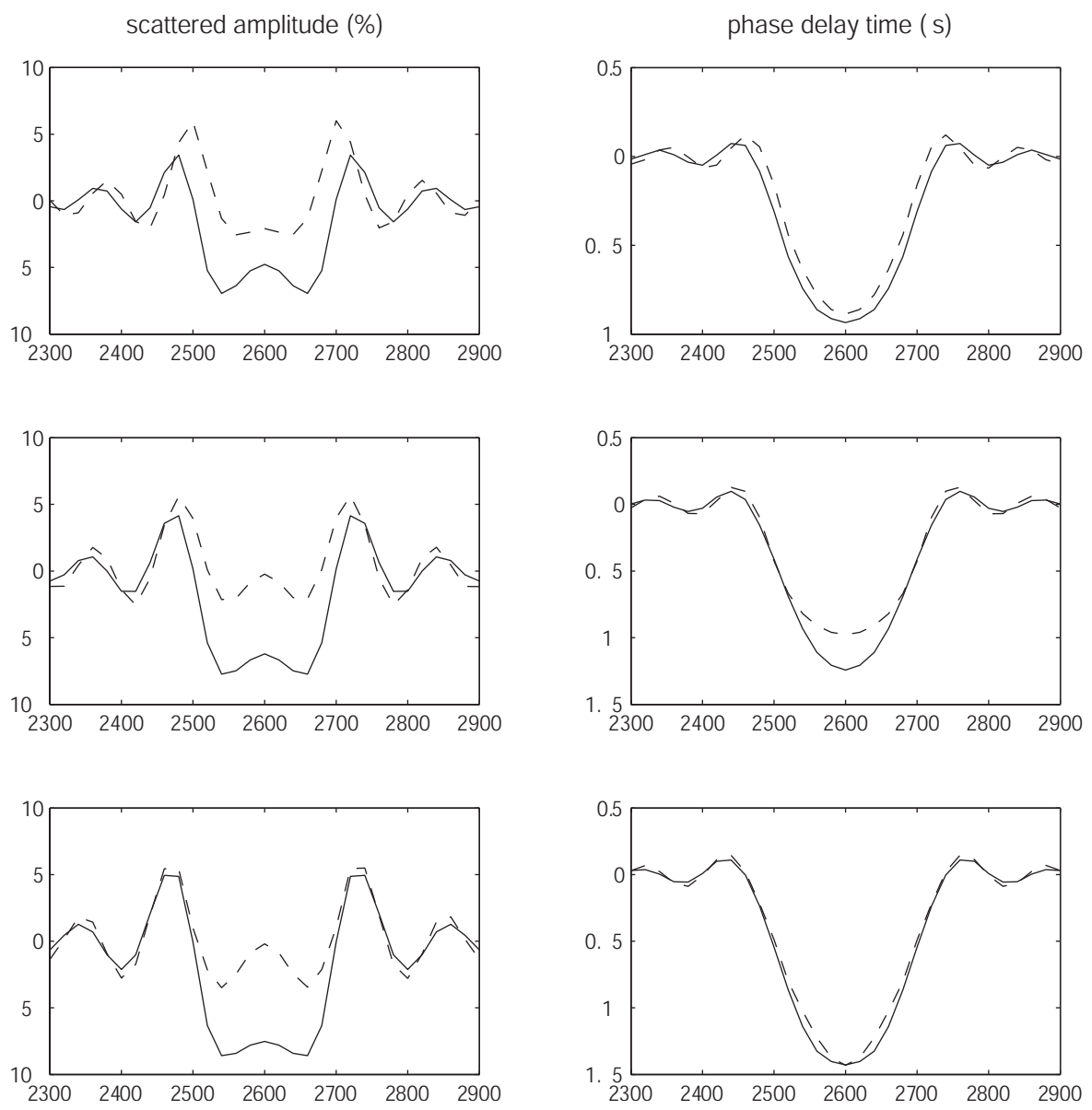


Figure 7

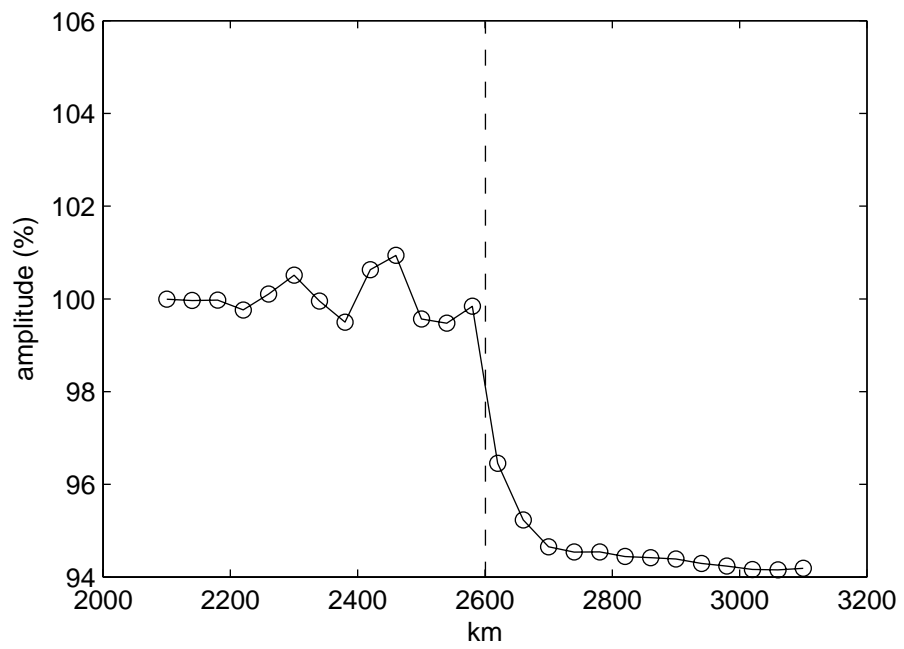


Figure 8

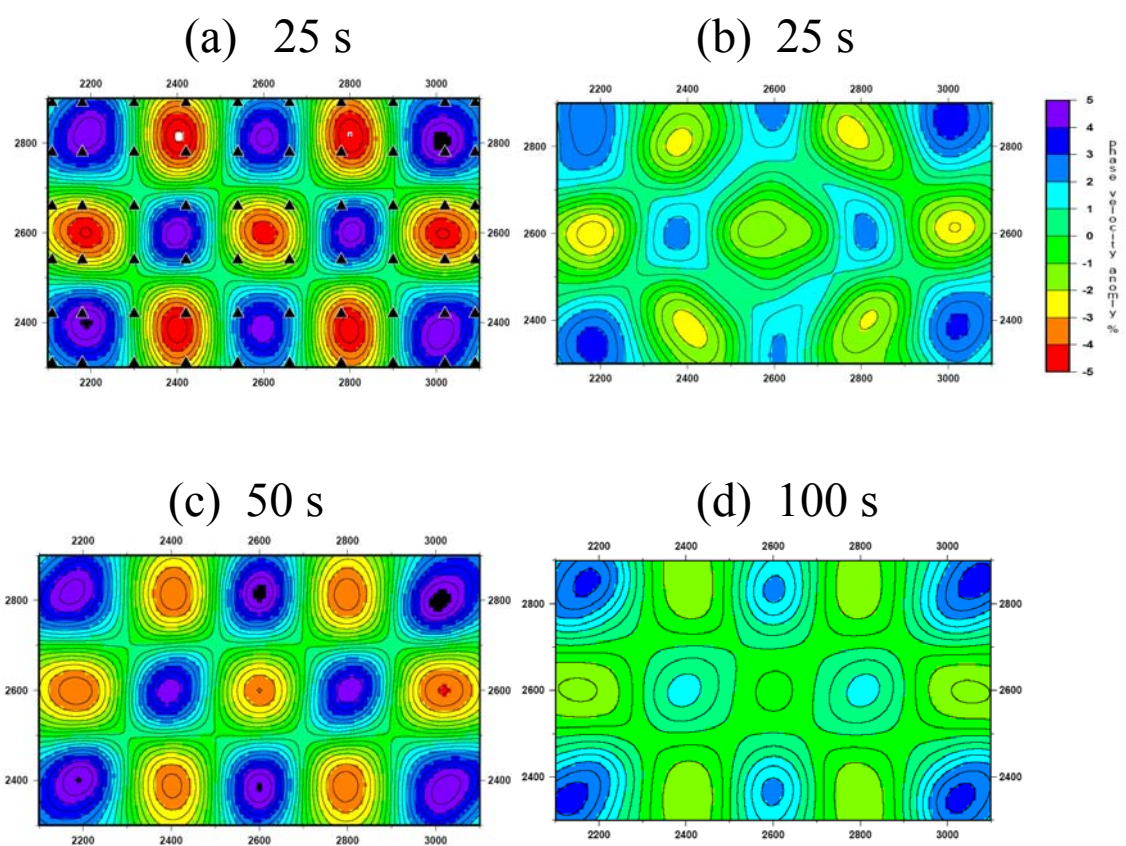


Figure 9

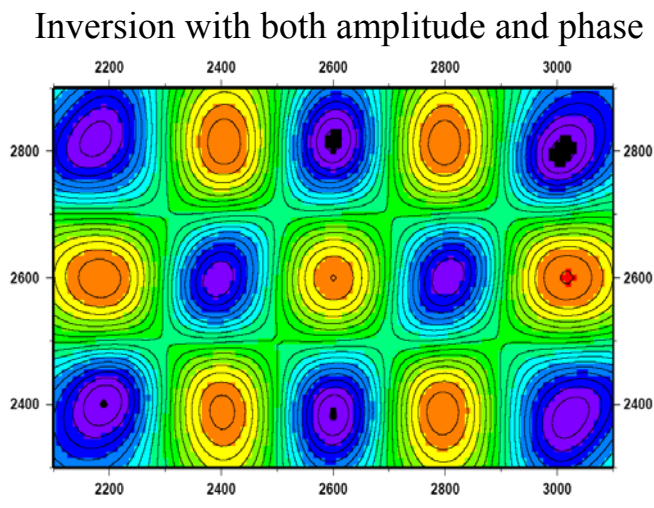
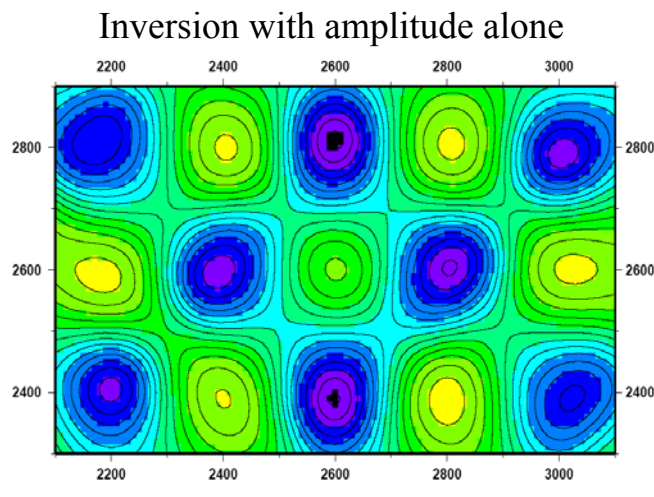
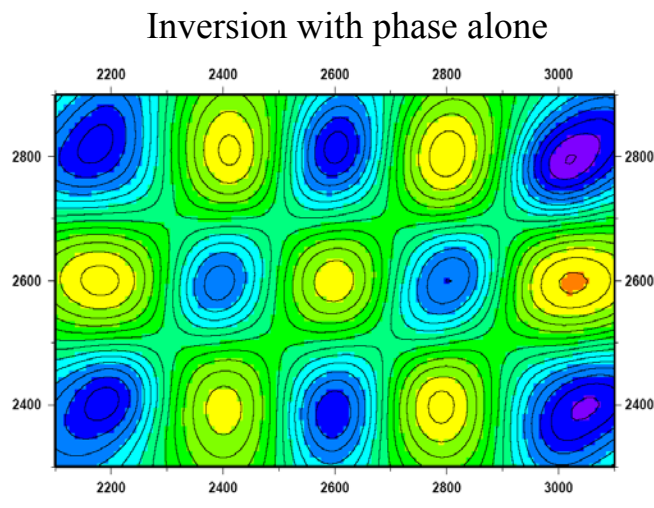


Figure 10

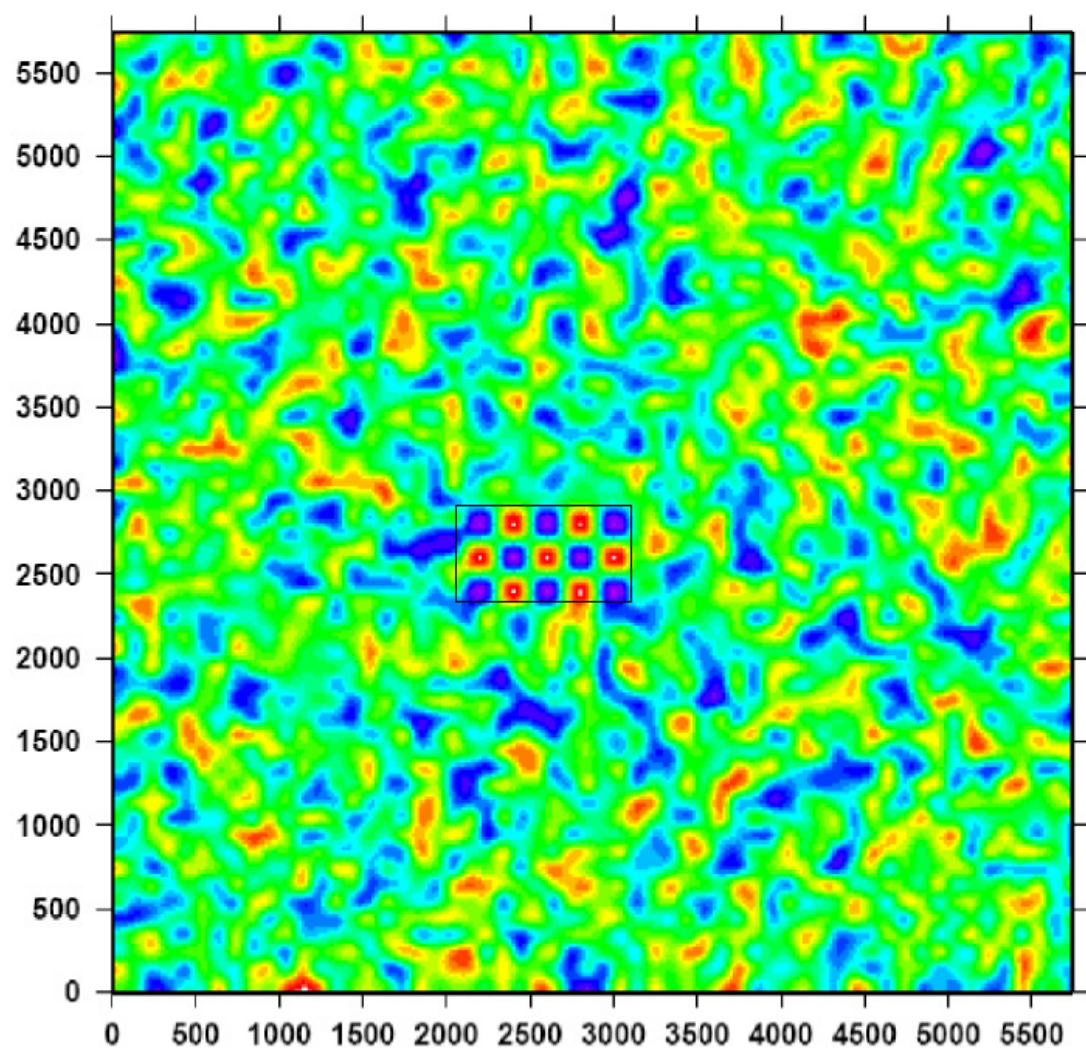


Figure 11

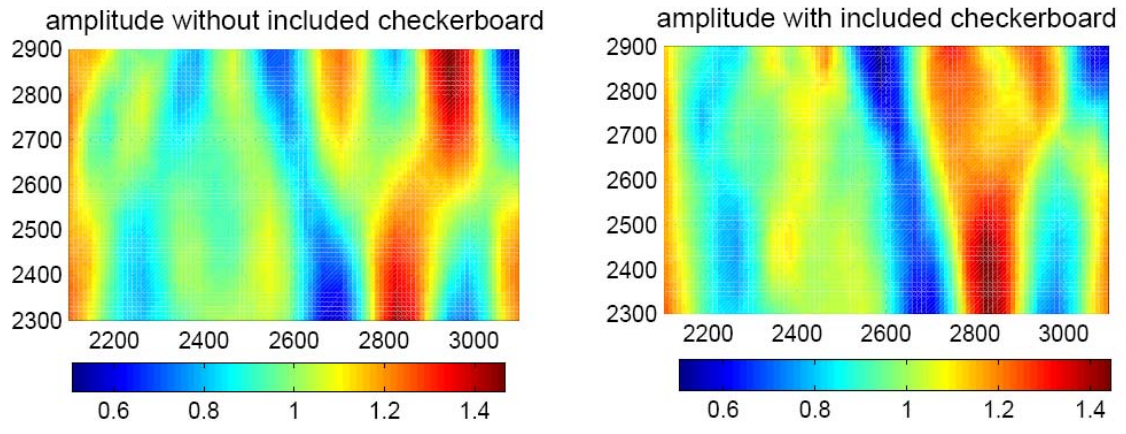


Figure 12

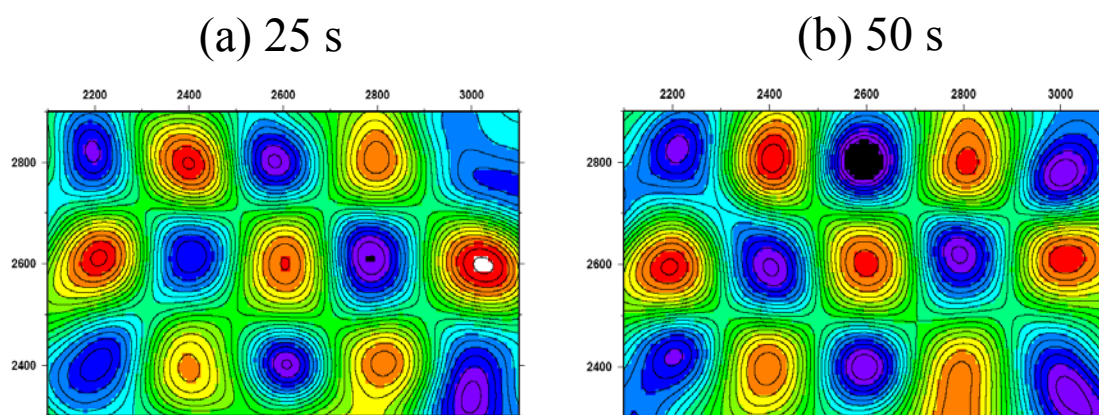


Figure 13

Chapter 2

Rayleigh Wave Phase Velocities, Small-Scale Convection and Azimuthal
Anisotropy Beneath Southern California

Yingjie Yang and Donald W. Forsyth

Department of Geological Sciences

Brown University

Providence, RI 02912

To be submitted to *Journal of Geophysical Research*

Abstract

We use phase and amplitude data of fundamental mode Rayleigh waves recorded at the TriNet/USArray network in southern California to invert for phase velocities at periods from 25 to 143 s. Finite-frequency scattering effects of Rayleigh waves are represented by 2-D sensitivity kernels based on the Born approximation. Site responses and station corrections are included as part of the inversion, and the incoming wavefield is represented as the sum of two plane waves. A one-dimensional shear wave velocity model based on the average phase velocities reveals a pronounced low velocity zone (LVZ) from 90 km to 210 km underneath a lithospheric lid. The average shear velocity in the lid is significantly slower than in typical stable continental or oceanic lithosphere and the low velocities in the low velocity zone probably require the presence of melt. Two-dimensional variations in phase velocities as a function of period are used to invert for three-dimensional S-wave velocities of the upper mantle. The pattern of velocity anomalies indicates that there is active small-scale convection in the asthenosphere beneath southern California and that the dominant form of convection is 3-D lithospheric drips and asthenospheric upwellings, rather than 2-D sheets or slabs. Several of the features we observe have been previously detected by body wave tomography, including delaminated lithosphere and consequent upwelling of the asthenosphere beneath the eastern edge of the southern Sierra Nevada and Walker Lane region; sinking lithosphere beneath the southern Central Valley; upwelling and low velocity anomalies beneath the Salton Trough region; and downwelling beneath the Transverse Ranges. Our new

observations provide better constraints on the lateral and vertical extent of these anomalies. In addition, we detect two previously undetected features: a high velocity anomaly that probably represents delaminated lithosphere beneath the northern Peninsular Range and a low velocity anomaly that may be caused by dynamic upwelling beneath the northeastern Mojave block.

We also estimate the azimuthal anisotropy from Rayleigh wave data. The strength of anisotropy is $\sim 1.7\%$ at periods shorter than 67s and decreases to $\sim 1\%$ at longer periods. The fast direction of apparent anisotropy is nearly E-W, consistent with the fast polarization axis of SKS splitting measurements in Southern California. The anisotropy layer is about 350 km thick, which implies that anisotropy is present in both lithosphere and asthenosphere. The E-W fast directions in the lithosphere and sub-lithosphere mantle may be caused by distinct deformation mechanisms: pure shear in the lithosphere due to N-S tectonic shortening and simple shear in sub-lithosphere mantle due to mantle flow.

Introduction

Southern California lies astride the boundary between the Pacific plate and the North American plate. The current plate boundary is broad, extending from offshore to the Basin and Range province. The complex evolution from a subduction boundary between the Farallon and North American plates to the present transform boundary [Atwater, 1998], involving rotating crustal blocks, passage of a triple junction, and opening of a slab window, has left scars in the lithospheric mantle and crust. That

evolution continues today along with generation of new structural anomalies that can be detected with geophysical experiments. For example, the bend in the San Andreas fault introduces a component of compression generating the Transverse Range and the underlying, sinking tongue of the lower lithosphere that is revealed by high seismic velocities in the mantle [*Bird and Rosenstock, 1984; Humphreys and Hager, 1990; Kohler, 1999*]. A similar high velocity anomaly beneath the Great (or Central) Valley is thought to be a sinking, lithospheric drip associated with delamination of the mantle lithosphere from beneath the volcanic fields of the southern Sierra Nevada [*Boyd, et al., 2004; Zandt et al., 2004*]. Upwelling of hot asthenosphere to replace this delaminated lithosphere creates melting and low-velocity anomalies beneath the southern Sierra and adjacent Walker Lane [*Wernicke, et al., 1996; Boyd et al., 2004; Park, 2004*]. Similarly, upwelling beneath zones of extension, like the Salton trough, also induces low velocity anomalies [*Raikes, 1980*]. The primary purpose of this paper is to improve the lateral and vertical resolution of these and other convective upwellings and downwellings by taking advantage of the nearly uniform areal coverage and sensitivity to asthenospheric and lithospheric structure provided by Rayleigh wave tomography.

A number of investigations have been conducted to study the compressional-wave velocity structure of the crust and upper mantle beneath southern California using P-wave travel time data [e.g. *Raikes, 1980; Humphreys and Clayton, 1990; Zhao and Kanamori, 1992; Zhao et al., 1996*]. Surprisingly, there are few shear velocity or surface wave studies. *Press [1956]* used Rayleigh waves to determine crustal structure in

southern California. *Crough and Thompson* [1977] argued on the basis of a single two-station measurement of Rayleigh wave phase velocities that there may be no mantle lithosphere beneath the Sierra Nevada. *Wang and Teng* [1994] inverted the phase velocity dispersion of Rayleigh waves using broadband data obtained from TERRAScope for the shear velocity structure beneath the Mojave Desert in southern California. *Polet and Kanamori* [1997] used long-period Rayleigh and Love waves from teleseismic earthquakes recorded by the TERRAScope network to investigate the overall shear velocity structure in the top 250 km of the upper mantle. Because there were relatively few broadband stations, these early studies did not map lateral variations throughout southern California. The deployment of the TriNet seismic network, now incorporated in USArray, made it possible to perform 3-D inversions for S-wave velocity from surface wave data. *Tanimoto and Sheldrake* [2002] conducted such a study using Rayleigh wave phase velocities measured using the two-station method. The requirement that two stations and a source event align along a great circle limited the area and density of seismic ray coverage, but within much of southern California they were able to resolve structure on a scale of 60 - 100 km. Finite frequency and scattering effects were also not incorporated in their inversion, which was restricted to a narrow frequency band (0.03-0.045 Hz), thus preventing the resolution of variations in lithospheric thickness and asthenospheric structure. In this study, we take the finite frequency and scattering effects into account using a wider frequency range (0.007-0.04 Hz) and employ an array analysis method that employs many more paths, thus improving the phase velocity resolution and

resolving fine structure beneath southern California in a greater depth range.

The second main goal of this investigation is to better resolve the origin of the seismic anisotropy observed in this region. Despite the complexity of lithospheric structure and tectonic history, the fast direction of shear wave splitting is nearly uniform throughout southern California. Shear wave splitting is often thought to be caused primarily by the anisotropy associated with lattice preferred orientation of olivine aligned by shearing flow in the mantle, with the fast direction roughly in the direction of mantle flow. The near vertical propagation of SKS phases commonly used in splitting studies, however, yields very little resolution of the depth of the anisotropic layer. If the anisotropy is caused by the horizontal alignment of the olivine a-axis, then the fast direction for splitting should coincide with the fast direction for Rayleigh wave propagation. The frequency dependence of the azimuthal anisotropy of Rayleigh waves should yield information on the vertical distribution of anisotropy, as waves of different periods are sensitive to different depth ranges.

In southern California, the fast direction found in SKS splitting measurements is dominantly E-W [*Savage and Silver, 1993; Ozalaybey and Savage, 1995; Liu et al. 1995; Polet and Kanamori, 2002*]. There are debates, however, about the origin of the anisotropic structure in southern California, that is, whether the anisotropy is dominated by plate tectonism and/or by sublithospheric mantle flow. *Ozalaybey and Savage [1995]* interpreted the E-W feature as being created by asthenospheric flow in the slabless window left behind the subducting Farallon plate. *Silver and Holt [2002]* also attributed

the splitting to asthenospheric flow, driven both by the motion of the Farallon plate and the motions of the Pacific and North American plates. On the other hand, *Liu et al.* [1995] proposed that the cause might be related to late Cenozoic N-S contraction in southern California, with anisotropy distributed throughout the lithosphere and into the asthenosphere. *Davis* [2003], summarizing observations in southern California of *SKS* and *SKKS* splitting, *P* wave horizontal polarizations, P_n anisotropy, and limited surface wave data, concluded that anisotropy is relatively uniformly distributed in the upper mantle from the Moho to a depth of 200 to 250 km. With a greater number of seismic sources and paths employed in this study, we can test whether there is a change in the fast direction or degree of anisotropy from lithosphere to asthenosphere and whether there is a shift in orientation between the Pacific and North American plates.

In this paper, we use Rayleigh wave data recorded at TriNet/USArray network in southern California to invert for 2-D phase velocities and azimuthal anisotropy at periods ranging from 25 to 143 s. Rather than the two-station method, we use an array analysis approach in which the complex incoming wavefield of each event is represented by the interference of two plane waves, which frees us from the requirement that sources and station pairs be aligned, enabling denser ray coverage and better lateral and azimuthal resolution than previous studies. In addition, our approach using finite frequency response kernels more accurately represents the sensitivity of phase shifts to lateral variations in structure and allows the incorporation of amplitude constraints on structure from the focusing and defocusing of waves caused by lateral heterogeneities. These

variations in amplitude carry nearly as much information about the velocity structure as the phase perturbations [*Dalton and Ekstrom, 2003*], but have usually been neglected in regional and global tomographic studies (exceptions include *Pollitz [1999]* and *Friederich [1998]*). The 2-D phase velocities at different periods are then inverted for 3-D shear velocity structure. Finally, we compare the azimuthal anisotropy with shear-wave splitting measurements from other studies to test models for the origin of the observed anisotropy.

Data selection, processing and station/site corrections

We use fundamental mode Rayleigh waves recorded at 40 broadband seismic stations selected from the TriNet/USArray network in southern California (Figure 1). About 120 teleseismic events that occurred from 2000 to 2004 with surface wave magnitudes larger than 6.0 and epicentral distances from 30° to 120° were chosen as sources (Figure 2). The azimuthal coverage of these events is very good, which enables us to resolve both azimuthal anisotropy and lateral variations in phase velocity unprecedentedly well. The ray coverage for Rayleigh waves at the period of 50 s in the network region is shown in Figure 3. As expected from the distribution of the events, the coverage is excellent with many crossing rays both inside and outside the array. The ray density decreases somewhat with increasing period as fewer earthquakes generate waves with good signal-to-noise ratio at the longest periods.

We use the vertical-component Rayleigh wave seismograms, because they are not contaminated by Love wave interference and typically have lower noise levels than the

horizontal components. The selected seismograms are filtered with a series of narrow-bandpass (10mHz), zero-phase-shift, Butterworth filters centered at frequencies ranging from 7 to 40 mHz. All of the filtered seismograms are checked individually and only those with signal-to-noise ratio larger than 3 are selected, thus restricting the accepted frequency range separately for each event. If an event at a particular period is acceptable at some stations but not others, we check whether the low signal-to-noise ratio is caused by high noise or by destructive interference associated with multi-pathing or scattering along the path. If noise levels are comparable to those at the acceptable stations, we retain the record because it will provide valuable information on the scattering pattern. Fundamental mode Rayleigh waves are isolated from other seismic phases by cutting the filtered seismograms using a boxcar window with a 50-s half cosine taper at each end. The width of the boxcar window is different for each period, but varies very little for different events at the same period and is identical for all seismograms from an individual source.

To effectively use the focusing and defocusing of Rayleigh waves as constraints on the lateral variations in velocity structure, we need to carefully account for other influences on amplitude. These influences include: scattering and multi-pathing outside the array; local site response or amplification; instrument response, including erroneous responses; source radiation pattern; intrinsic attenuation and scattering from small-scale heterogeneities within the array; noise; and interference from other modes. We minimize the effects of noise by careful selection of the period range accepted for each

station/event and by our application of frequency dependent windowing. Windowing also effectively isolates the dispersed fundamental mode from higher modes, and the amplitude of the fundamental mode is usually much greater than that of other modes for the shallow sources we employ. We neglect the source radiation pattern because the aperture of the array is small compared to the distance to the source; after eliminating events close to nodes in excitation of the surface waves, the expected variation in initial amplitude and phase with azimuth from the source is negligible. We correct for geometrical spreading on a sphere and model anelastic attenuation as part of the tomographic inversion. We assume amplitude decays with propagation distance x as $e^{-\gamma x}$, where γ is the attenuation coefficient, and solve for the optimum value of γ for each period. Details of the resolution of attenuation are described in a separate paper [Yang and Forsyth, in preparation]. In the next section, we explain our approach to scattering and multi-pathing outside the array.

A key element in our study is the correction for instrument responses. The 40 broadband stations consist of several different types of seismometers. It often may not be properly appreciated, but just as stations frequently have misoriented horizontal components [Schulte-Pelkum *et al.*, 2001], they also commonly have misreported or miscalibrated response functions. In every study we have performed to date that has involved multiple instrument types (MELT Experiment, northeastern US/MOMA, Colorado/Rocky Mountain Front, Tanzania), we have found that the instrument response parameters reported for at least one of the instrument types has been incorrect. We first

use the published responses to correct all seismograms to the response of a common instrument type. Incorrect amplitudes and phases responses are then detectable through amplitude mismatches or careful comparison of waveforms at adjacent stations. Then, as part of our tomographic inversion for phase velocities and wavefield parameters, we group each station type together and solve for an amplitude correction and phase correction for that group of seismometers as a function of frequency (keeping one type fixed as the standard). We then correct all the seismograms to the standard response and repeat the inversion, this time allowing a separate amplitude response for every station, because individual stations sometimes do not function in the same way as others of the same type. In principle, if there were no other factors affecting amplitude, one could solve for corrections to one station of a pair of stations using just two earthquake sources producing waves traveling in opposite directions along a great circle path between the two stations. In practice, using many sources from a wide range of azimuths, we find amplitude corrections resolved with standard deviations of just a few percent, including tradeoffs with focusing, wavefield parameters (see next section) and attenuation.

Typically, the second stage solutions for individual station responses will deviate from the average, standard response by up to about 20% at short periods (~ 25 s) and then gradually approach ~ 1.0 at long periods ($> \sim 100$ s) (figure 4). We attribute this pattern to local site responses rather than instrument problems. At longer wavelengths, the wave averages over a broader area and greater depth range and the site responses are

expected to become more uniform. Amplification of surface waves at very short periods (< 10 s), of course, is a very well known and important factor in earthquake hazards [e.g., Shapiro et al., 1997], but has largely been ignored at longer periods. Occasionally, we find a station where the response does not approach 1.0 at long periods, which we interpret as an incorrect response function. We then isolate this station from others of its group and recalculate the responses for each instrument type, with a separate response for that particular instrument. (In addition to solving for amplitude correction factors, if there is any indication of incorrect response, we also solve for phase correction factors.) This procedure loses any information about site response for that problem station, but it does preserve the correction needed for reliable determination of variations in amplitude for a wave propagating across the array. If there is any indication that the response of a particular station is not uniform with time, we drop that station from our analysis entirely.

After identifying problematic stations, there is a clear geographic pattern to the apparent site responses at short periods (Figure 5) that correlates with tectonic province and with the pattern of phase velocities. These site responses carry information about local structure that we will explore in a future study. Numerical experiments on the propagation of Rayleigh waves through synthetic, heterogeneous media demonstrate that the single scattering approximations we use below in assessing the amplitude effects of focusing within the array do not take into account the local site response within the anomaly itself, although the apparent response may also be affected by inadequate

representation of back-scattering [Yang and Forsyth, 2005]. The important point for this study is that the station correction terms account for instrument and site effects not incorporated in other parameters of the model.

Methodology of surface wave tomography

One of the most important questions in phase velocity inversion of surface waves is how to represent incoming wavefields. The conventional approach is to regard incoming waves as plane waves propagating along great-circle paths and use a two-station method to find the phase difference between two stations. However, most events show variations in amplitude or waveform across the array of a seismic network, which is indicative of scattering or multi-pathing caused by lateral heterogeneities between the source and the array. These effects will distort the incoming waves, causing deviations of incoming directions from the great-circle azimuths and leading the wavefields to be non-planar. Neglecting the non-planar character can systematically bias the apparent phase velocities if only waveforms with constructive interference are selected [Wielandt, 1993]. In California, Rayleigh waves at short periods show strong interference due to scattering and multi-pathing. Events with incoming rays from the Pacific tend to have simpler waveforms than those coming through the North American plate, due to the simpler tectonic structures in the Pacific plate and fewer ocean-continent boundaries that are crossed. Seismograms of Rayleigh waves at long periods are simpler and clearer than at short periods due to the reduced complexity of seismic

structures at depth.

In this study, we use the sum of two plane waves, each with initially unknown amplitude, initial phase, and propagation direction [Forsyth *et al.*, 1998; Forsyth and Li, 2005] to represent the non-planar incoming wavefield, i.e., a total of six parameters to describe the incoming wavefield. This simple representation of the incoming wavefield has been successfully applied to other continental regions to obtain phase velocities and azimuthal anisotropy structures [Li *et al.* 2003; Weeraratne *et al.*, 2003]. We recognize that the full complexity of the wavefield is not always well represented by this simple model, but this approach avoids the damping necessary for stability when a series of orthogonal polynomials, equivalent to many plane waves, is employed [Friederich *et al.*, 1994; Friederich and Wielandt, 1995; Friederich, 1998; Pollitz, 1999] and it provides a good approximation when the amplitude variation due to interference forms an approximately sinusoidal pattern elongated roughly in the direction of wave propagation, a common form. In cases where the two-plane-wave approximation is not a good model, the misfits are regarded as noise and that event for that particularly period is automatically down-weighted [Forsyth and Li, 2005].

Another important issue is how to represent finite-frequency effects, which are important in regional surface wave tomography since the goal typically is to resolve structures with scales on the order of a wavelength. Yang and Forsyth [2005] have shown that finite frequency scattering effects by heterogeneous structures can be accurately represented by the 2-D sensitivity kernels with the Born approximation derived by Zhou

et al. [2004]. Yang and Forsyth also demonstrated that employing the tomography method we use in this paper, utilizing the Born kernels in conjunction with the two-plane-wave method, provides a much better resolution of local structure than is obtained representing the sensitivity kernels with a Gaussian-shaped influence zone [e.g., *Debayle and Sambridge, 2004; Sieminski, et al., 2004; Forsyth and Li, 2005*]. For each of the two plane waves, the 2-D sensitivity kernels at each period depend on reference phase velocity and the length of the window used to cut seismograms in data processing. An example of sensitivity kernels for a Rayleigh wave at period of 50 s windowed using a 300-s boxcar window is shown in Figure 6. Windowing the time series implicitly introduces frequency averaging into the Fourier analysis for the amplitude and phase of a particular frequency; the averaging creates interference that reduces the amplitude of the outer Fresnel zones. The kernels also have been smoothed with a 2-D Gaussian filter, because we interpolate velocities between nodal points using a 2-D Gaussian averaging function that restricts the scale of heterogeneities allowed. Perturbation of a nodal value perturbs the velocities in the surrounding region and our sensitivity function represents the integrated effect of that distributed disturbance. The filter for the example shown falls off to $1/e$ of its maximum value at a distance of 65 km from the center. The sensitivity kernels have a broad distribution and become broader with increasing distance from station along the ray path. The sensitivity is mainly concentrated in the region of the first two Fresnel zones, and quickly decreases in higher-order Fresnel zones.

Surface wave phase velocity c in a uniform slightly anisotropic medium can be

represented as

$$c(\omega, \psi) = A_0(\omega) + A_1(\omega) \cos(2\psi) + A_2(\omega) \sin(2\psi) + A_3(\omega) \cos(4\psi) + A_4 \sin(4\psi) \quad (1),$$

where ω is frequency, ψ is the azimuth of wave propagation, A_0 is the azimuthally averaged phase velocity, and A_1 to A_4 are azimuthal anisotropic coefficients [Smith and Dahlen, 1973]. We neglect the A_3 and A_4 terms here because they should be small for Rayleigh waves [Smith and Dahlen, 1973]. Scattering effects of the phase velocity perturbation $(c - c_o)$ relative to average phase velocities c_o at each grid node are expressed as:

$$\delta d = \iint_{\Omega} K_d^c(r, \omega) \left(\frac{c - c_o}{c_o} \right) dx^2, \quad (3)$$

where the integration is over the entire study region. δd is shorthand for the phase delay or the relative amplitude variation with the corresponding phase kernel or amplitude kernel (Figure 6). The study region is parameterized with a total of 399 grid nodes that are distributed evenly in the study region (Figure 7). The density of grid nodes in the middle of the region is higher with 0.50° spacing in both longitude and latitude, and the density in the edge is lower with node spacing of 1.0° . The gridded region is much larger than the station-covered region, which is important since the outer region can absorb some variations of the wavefields that are more complex and cannot be completely represented by the interference of two plane waves.

We use phase and amplitude data to simultaneously solve for the wavefield parameters of each event and the velocity parameters (A_0 , A_1 and A_2) of each grid node in

an iterative, least-square inversion. Each iteration involves two steps: first, we use a simulated annealing method to solve the six wavefield parameters for each event individually; then we apply a generalized linear inversion [Tarantola and Valette, 1982] to find the phase velocity coefficients at each node, the station corrections, the attenuation coefficient, and changes to the wavefield parameters. After completing the inversion, we have estimates of the quality of fit for each individual event. We weight each event by its standard deviation to de-emphasize noisy data or complex wavefields that are not adequately represented by the two-plane-wave approximation and then repeat the inversion to obtain the final result. Details of the inversion procedure are given in Forsyth and Li [2005] and Yang and Forsyth [2005].

Isotropic phase velocity variations

As required for any non-linear inversion, we need an appropriate starting model for lateral phase velocity inversion. Thus in the first step, we invert for average phase velocity by assuming that velocity is uniform in the entire study region at each period. The average dispersion curve is shown in Figure 8. The average phase velocities increase from 3.66 km/s at 25 s to 4.14 km/s at 143 s. The dense ray path coverage leads to small standard deviations for these averages, much smaller than reported in previous studies. There is a change in the slope of the dispersion curve around 33 s, indicating a change from sensitivity to the crust and uppermost mantle at short periods to primarily mantle sensitivity at longer periods. The concave-upward shape of the dispersion curve from

50 s to 80 s is an indicator of a possible low-velocity zone underlying a higher velocity lithospheric lid.

2-D lateral variations of phase velocities at each period are obtained using the average phase velocities as the starting model, allowing the phase velocity coefficients at each node to vary. The coefficients at these nodes are used to generate maps of lateral phase velocity variations on finer grids for plotting purposes (0.1° by 0.1°) by averaging the values at neighboring nodes using a Gaussian weighting function with a characteristic length, L_w , of 65 km, the same length used to smooth the 2-D sensitivity kernels described in the previous section. The choice of the characteristic length has great effects on model resolution and variance. The usual tradeoff between model resolution and variance exists; the smaller L_w , the higher the resolution (i.e, smaller-scale variations of phase velocities can be resolved) and the larger the variance. We can also influence this tradeoff with our choice of *a priori* variances assigned to the nodal velocity parameters, which act as damping terms, but the imposed Gaussian averaging introduces a more uniform spatial scale to the smoothing. We chose 65 km as the optimum value in this study after performing a number of experiments using different L_w . Standard errors of phase velocities in these maps are estimated from the modal covariance matrix of the phase velocity coefficients by linear error propagation [Clifford, 1975]. Figure 9h is a map of twice the standard errors of phase velocities at 50 s period, which can be interpreted as indicating how large the variations within the phase velocity map (Figure 9c) have to be to be significant at the approximate 95% confidence level. Standard errors

are smallest at the center of the study area, where densities of both stations and crossing ray paths are greatest, and gradually increase toward the edge. Maps of phase velocities are masked using the 1% contour of twice standard errors for 50 s, eliminating the illustration of phase velocity variations in the region outside this contour that are relatively poorly constrained. Maps of standard errors at other periods are similar in form, but the magnitude of the errors increases with period, because at longer periods the Fresnel zone broadens decreasing local sensitivity, the travel time errors increase for the same relative phase error, and the number of seismograms with good signal-to-noise ratio decreases.

We have explored the dependence of the phase velocity anomalies on the starting model by using an alternative approach. Instead of using the average velocity at each period as the starting model, i.e., a laterally uniform starting model, we have tried starting with a laterally variable model consisting of the average velocity for a given period perturbed by the anomalies found for an adjacent period. We began at our best-constrained period, 50 s, and worked progressively toward shorter and longer periods, each time using the percentage perturbations from the previous period as the starting model. In principle, this approach should lessen the effects of damping; assuming there is overlapping sensitivity to structure at adjacent periods and noise is uncorrelated, this procedure should allow the amplitude of true phase velocity perturbations to be more accurately mapped. We found, however, that with our choice of damping parameter and averaging length there was no significant difference in the

models from those with uniform starting velocity; nowhere did the difference exceed about 1 standard deviation of the initial models.

Figure 9a-g shows maps of phase velocities at periods of 25, 33, 50, 67, 83, 100 and 125 s. There are several pronounced features observed with patterns that vary gradually between adjacent periods. The continuity of features between adjacent periods is due to the overlapping depth ranges of Rayleigh wave sensitivity to structure. In contrast, the correlation between residuals to the models at these periods is very low, as reported also by *Weeraratne et al.* [2003], so artifacts due to noise or scattering from outside the array are unlikely to appear in more than one of these maps. Most of the anomalies we describe below have been previously detected in body or surface wave tomography studies.

There is a striking low velocity anomaly with north-south trend imaged in the region of the southeastern Sierra Nevada and Walker Lane volcanic fields from 25 s to 50 s, suggesting the possible presence of partial melting at shallow depths in the mantle. This area has previously been described as a low-velocity zone for P-waves in the shallow mantle, attributed to lithosphere delamination [*Wernicke et al.*, 1996; *Boyd et al.*, 2004; *Park*, 2004]. A strong high velocity anomaly is observed in the offshore Borderland region at 25 to 33 s, probably due to thin crust. This high velocity anomaly is somewhat different from that reported by *Tanimoto and Sheldrake* [2002], who found a velocity contrast across the San Andreas fault with phase velocities on the Pacific plate side systematically higher than on the North American side. In our study, the highest

velocities are confined to the coastal Borderlands and the strongest gradients in velocity do not straddle or parallel the fault. A possible reason for this difference may be that the high velocities in the offshore region may be smeared towards east in *Tanimoto and Sheldrake* [2002] due to the dominant west-east direction of the ray paths and the lack of crossing rays. Another high velocity anomaly is observed in the Transverse Range from 33 s up to 83 s, indicating that high S-wave velocity is present in the upper mantle extending well down into the asthenosphere, as reported in many previous P-wave tomography studies. High velocities are also imaged in the southern Central Valley at periods shorter than 67 s and in the Peninsular Range near the California/Mexico border at periods longer than 50 s. The Central Valley anomaly has sometimes been called the Isabella Anomaly [*Aki*, 1982; *Jones et al.*, 1994; *Boyd et al.*, 2004], but the Peninsular Range anomaly has not been reported previously, perhaps due to the scarcity of stations and the greater apparent depth (as it is strongest at the longest periods).

There is a small, low-velocity anomaly in the Salton trough, also detected in many previous P-wave studies [e.g., *Hough*, 1982], that is present at all periods, with its center shifting to the southeast with increasing period. The low-velocity anomaly at periods equal to or greater than 83 s centered at 35.3°N, 117.2°W in the northern Mojave desert has not previously been reported, again, perhaps due to its greater apparent depth. Some small-scale anomalies are observed usually at the edges of the maps at individual periods, which we consider to be questionable features due to poor resolution in these marginal areas.

Average shear wave velocity structure

Phase velocities can only tell us integrated information about the upper mantle. In order to obtain direct information at various depths that can be interpreted in terms of temperature anomalies, the presence of melt and/or fluids etc., we invert phase velocities for shear wave velocities. Rayleigh wave phase velocities primarily depend on S-wave velocities, less on density and P-wave velocities. P-wave sensitivity is confined primarily to the crust. Therefore we only solve for S-wave velocities by coupling P-wave velocities to S-wave velocities using a constant Poisson's ratio, which is a reasonable approximation for the materials of the crust and uppermost mantle.

The data in this inversion are phase velocities of the 11 periods from 25 s to 143 s at each point of the phase velocity maps. We perform a series of 1-D inversions at each map point to build up a 3-D model. The model parameters are shear wave velocities in each of ~20-km thick layers extending from surface to 200 km with structure below that depth fixed to the starting model. Synthetic phase velocities and partial derivatives of phase velocities with respect to the change in P and S wave velocities in each layer are computed using Saito's algorithm [*Saito*, 1988]. The model parameters are slightly damped by assigning prior standard deviations of 0.2 km/s in the diagonal terms of model covariance matrix and smoothed by adding off-diagonal terms to the model covariance matrix that enforce a 0.3 correlation in changes of shear velocities in the adjacent layers.

Because the inversion is somewhat non-linear and highly underdetermined due to the limitations of surface wave vertical resolution, details of the resultant model on scales smaller than the resolving length will depend strongly on the starting model and relative damping for shear wave velocities and the crustal thickness. In order to obtain an appropriate reference model in our study region, we first perform an inversion using the average phase velocities for the entire region (Figure 8) with the TNA model of *Grand and Helmberger* [1984] (Figure 10) as the starting model. The TNA model represents the average upper mantle shear structure in western United States. The crustal thickness is fixed at 30 km, which is the average crustal thickness in southern California constrained from receiver function studies [*Zhu and Kanamori*, 2000; *Magistrale et al.*, 2000]. For this reference model, velocity is allowed to vary to a depth of 400 km, because the standard deviations of the average phase velocities are much smaller than the uncertainties associated with lateral variations, yielding better depth resolution.

The final 1-D reference model is shown in Figure 10. S-wave velocity is 3.28 km/s in the upper crust and 3.66 km/s in the lower crust. The S-wave velocities in the upper mantle are different from the TNA model. The most striking feature is a low velocity zone from 90 km to 210 km with the lowest velocity of 4.05 to 4.1 km/s at a depth of 125 km, which is consistent with the low shear velocities in the upper mantle observed by *Polet and Kanamori* [1997]. Beneath 230 km, the S-wave velocity is indistinguishable from the TNA model. This low-velocity zone underlies a relatively high velocity upper mantle lid. The velocity contrast between the low-velocity zone and the upper mantle lid

is about 6%. If we adopt the depth of maximum negative velocity gradient as the best estimate of the base of lithosphere, which is the most frequently used criterion in surface wave studies of both oceanic and continental regions, our best estimate of average lithospheric thickness in Southern California is about 90 km. Some other studies also observed similar thickness of the lithosphere in this area. For example, based on the depth extent of the P-wave velocity contrast between the Salton Trough and surroundings [Humphreys and Clayton, 1990], Humphreys and Hager [1990] estimated lithospheric thickness of about 70-100 km. The surface wave study by Wang and Teng [1994] showed that the lithospheric thickness in the Mojave Desert is about 100 km. The differences between these studies is reasonable considering the uncertainties of about 20 km in the depth to the maximum gradient with resolving lengths of about 50 km at 90 km.

The combination of a 90-km-thick lithosphere and average shear velocity of only about 4.35 km/s in this high velocity mantle lid suggests that composition or phase state may control the thickness of the lid and the existence of the pronounced low-velocity zone, rather than the temperature structure alone. One contributing factor to a low average velocity in the lid is the inclusion of a region within the average in which the lithosphere is completely removed (see later discussion of lateral variations), but much of southern California lies within 2% of the average. In other areas of comparable lid thickness, such as old oceanic lithosphere [Nishimura and Forsyth, 1989] or eastern North America [Van der Lee, 2002; Li et al., 2003; Rychert et al., 2005], Rayleigh wave inversions yield typical lithosphere S velocities of 4.6 to 4.7 km/s. A ~ 0.30 km/s or

6.5% decrease in velocity of the lid compared to these other areas requires an increase in temperature of ~ 750 °C if accomplished purely through elastic effects [Stixrude and Lithgow-Bertelloni, 2005]. The effects of anelasticity can greatly enhance the temperature sensitivity; using the model of Jackson *et al.* [2002], anelasticity reduces the temperature change required to a minimum of about 200 to 250 °C. Attributing the velocity reduction to anelastic effects, however, requires high attenuation and, equivalently, low seismic quality factor Q . We find Q for the shear modulus in the high velocity lid in southern California to be on the order of 200 [Yang and Forsyth, in preparation], much too high to have a major effect on apparent velocity. Thus, the average temperature contrast between the southern California lid and the lithosphere in stable continental regions is likely to significantly exceed 250 °C. Based on heat flow, Humphreys and Hager [1990] estimated temperature at the base of a 30-km-thick crust in southern California to be ~ 800 °C, in contrast to typical values of 500-550 °C at the base of 40-km-thick Proterozoic continental crust [Rudnick *et al.*, 1998].

If the lithosphere is a thermal boundary layer and the mantle from 30 to 90 km is several hundred degrees hotter than the lithosphere in eastern North America, why is the high velocity lid nearly the same thickness and why is there a large velocity drop into the low-velocity zone? Under ordinary circumstances, the thermal boundary layer would be expected to thin as the average temperature in a given depth range increases and the transition at the base of the thermal boundary layer should be gradual with no further drop in velocity beneath it. One possibility is that the thickness is controlled by a

compositional or state change, such as the presence of water or melt in the low-velocity zone with the base of the high-velocity lid representing a dehydration boundary or the solidus. Indeed, many estimates of lithospheric thickness have presumed that the base of the lithosphere is the solidus [e.g., *Humphreys and Hager, 1990*]. Another possibility discussed by Humphreys and Hager is that there is a non-steady-state temperature profile in the lithosphere with a large warming gradient at its base due to cooling of the lower continental lithosphere during the time of subduction of the Farallon slab, now replaced by asthenosphere. It is difficult to explain, however, shear velocities as low as 4.1 km/s in the mantle without the existence of melt [*Stixrude and Lithgow-Bertelloni, 2005*] or a solid-state mechanism that leads to much higher attenuation than we observe [*Faul and Jackson, 2004*].

As in any inversion problem, we need to evaluate the resolution of model parameters, which can tell us how well shear velocities at different depths are resolved. The elements of resolution matrix that can be computed in the inversion provide useful measurements of resolution. The rank of the resolution matrix provides an overall measurement of resolution, which describes the number of pieces of independent information about the model parameters provided by the data, i.e., the number of linearly independent combinations of model parameters that can be resolved. For the average shear velocity of the entire region, the rank is 4.2. For typical points in Figure 9, the rank is 3.0. The rank for the entire region is higher than for a typical point, because the uncertainties of average phase velocities for the whole region are much smaller than for a

typical point. If the resolution matrix is an identity matrix, each of the model parameters is perfectly resolved and the solution is equal to the true solution. If the row vector of resolution matrix has non-zero off-diagonal terms that spread about the diagonal term, the particular solution will represent a smoothed solution over a range of depth. The resolution length is a measurement of this depth range over which the average shear velocity can be well resolved, i.e., the sum of the diagonal elements of the resolution matrix over that length scale adds to one piece of information and the resolution kernel is reasonably compact. For example, at the depth of 50 km, the resolution length is ~40 km. The resolution kernels at three depths for the average model are plotted in Figure 11, which shows how the information about shear velocity at a particular depth is entwined with the information about shear velocities in adjacent layers. The resolution length increases with depth, because longer period Rayleigh waves sensitive to deeper structures have broader sensitivity range. Resolution kernels for the point-by-point inversions are similar in the upper 150 km with the primary loss of information compared to the average model coming at depths greater than 200 km. Below 200 km, there is little information available from phase velocity data about lateral variations in structure, so we fix the models to the reference model in inverting for the 3-D velocity structure.

Crustal structure

Combining all the inversion results of shear wave velocities beneath each point, we

form a model of the 3-D shear velocity structures in southern California. Rayleigh waves cannot directly detect seismic discontinuities since they are sensitive to the seismic velocity structure over a broad depth range; there is a large tradeoff between the crustal thickness and the seismic velocities of lower crust and uppermost mantle. For instance, a 5-km change of Moho depth with a 0.7 km/s shear velocity contrast across the Moho can be approximately matched with a 0.1 km/s velocity change over a depth range of 20 to 55 km in the inversion. In order to constrain the tradeoff between them, we use prior information of crustal thickness from other studies and restrict the change of crustal thickness within a small range from the starting values by assigning an *a priori* model standard deviation of 2 km to the crustal thickness. The partial derivatives for crustal thickness change include the effects of the P-velocity and density contrasts in addition to the shear velocity contrast across the Moho.

There are two available models of crustal thickness in southern California region that cover most of the study area. *Zhu and Kanamori* [2000] (referred to as model 1 hereafter) estimated the crustal thickness and V_p/V_s under a large number of three-component seismic stations using a receiver function stacking technique that incorporates the Ps converted phase and later multiple reverberations. Their technique is not sensitive to an assumed crustal P velocity. The calculated Moho depth is 29 km on average and varies from 21 to 37 km. *Magistrale et al.* [2000] (model 2) used the same data set as *Zhu and Kanamori* [2000], but they use Ps converted phase minus P times measured from receiver functions and crustal seismic velocities determined by

tomographic analysis of local earthquakes [*Hauksson, 2000*]. The Moho depths found by *Magistrale et al.* are typically 2 to 4 km deeper than the Moho depths found by *Zhu and Kanamori*. In some areas, the difference is as large as 6 km.

The difference of crustal thickness between these two models is significant. In order to evaluate which one is more reasonable, we did 3-D shear velocity inversions using each of these two crustal models as the starting values for the crustal thickness while keeping the starting values of shear velocity the same. As expected, the difference between these two inversions is significant. Shear velocities in the crust using model 2 are overall higher than those for model 1. The most pronounced differences lie beneath the Peninsular Range. The shear velocities using model 2 have maximum values of 3.4 km/s in upper crust and 3.82 km/s in lower crust in this region. This high velocity is probably the result of overestimated crustal thickness of model 2, which predicts a thickness of 40 to 44 km, about 4 to 6 km thicker than model 1. We conclude that model 2 overestimates the crustal thickness in southern California. The reason for greater crustal thickness in model 2 may be the low V_p/V_s ratios. The V_p/V_s ratios in model 2 are determined using P and S-P travel times from local earthquakes and controlled sources [*Hauksson, 2000*], and the ray paths of P and S-P travel time are nearly horizontal, whereas the teleseismic receiver function uses teleseismic P and Ps phases that propagate along nearly vertical paths in the crust. The V_p/V_s ratio and absolute velocities obtained from nearly horizontal propagating waves may be different than for nearly vertical propagating waves due to anisotropic structure in the crust [*Paulssen, 2004*]. Because it

results in smaller crustal velocity anomalies in our Rayleigh wave inversions, we conclude the crustal model of *Zhu and Kanamori* [2000] is more reasonable and we use it to set starting values for crustal thickness in the tomographic image illustrated in Figure 12 and described below.

In the crust, the most pronounced feature is a high velocity anomaly along the southern Peninsular Ranges (Figure 12a,b), which is consistent with fast P-wave velocities reported for the lower crust [*Zhao and Kanamori*, 1992; *Zhao et al.*, 1996] or even thinner crust than estimated by *Zhu and Kanamori*. A slightly high anomaly is observed in the Death Valley region. In the Salton Trough region, the velocity is low. Strong anomalies are also imaged in the crust along the eastern edge of our study area: a high velocity anomaly along the southern Arizona/California border and a low velocity anomaly in southern Nevada. We regard these edge anomalies as questionable. As more stations are deployed in USArray in Arizona and Nevada, we should be able to resolve their strength and shape with more confidence.

The final map of crustal thickness is shown in Figure 13. Because we assign strong damping to the crustal thickness parameter, it differs little from the interpolated starting model of *Zhu and Kanamori*. Some of the lower crustal and uppermost mantle anomalies probably represent errors in crustal thickness. As discussed below, we think the crustal thickness in much of the California Borderlands region in the model is overestimated, because the model has simply interpolated between stations in the Peninsular Range and the few island stations off the coast where receiver function

analyses are available. A better model of crustal thickness could be created by combining the seismological information with other geologic and tectonic indicators, but we can use the apparent velocity anomalies to indicate places where the crustal model is likely to be in error. Our focus is on upper mantle anomalies, but we have to be cautious in interpreting anomalies in the shallowest mantle, because there are possible trade-offs where crustal thickness is poorly constrained by other observations.

Upper mantle anomalies and small-scale convection

Delamination beneath the Sierra Nevada. In the uppermost mantle, strong low velocity anomalies exist underneath the eastern edge of the southern Sierra Nevada and the Walker Lane region from the Moho to 90 km underlain by high velocities at depths greater than 110 km (Figure 12c-e and Figure 14a,c). The anomaly in the 50-to-70-km depth range reaches an amplitude of 5-6%, which is equivalent to the contrast between the high velocity lid and the low-velocity zone, indicating a complete absence of the lithosphere at depths greater than 50 km. The change of seismic velocities from anomalously low values at shallow depths to anomalously high values at greater depth may be the result of a downwelling or detachment of cold lithosphere and an upwelling of hotter upper mantle filling the space left by the downwelling lithosphere. Surface wave inversions often yield oscillatory solutions for the vertical distribution of shear velocity with length scales or amplitudes of the oscillations below the level of resolution, which might be a factor that could exaggerate the high velocity anomaly in the 130-170

km depth range, but we are confident that the reversal is real. First, the reversal is present in the phase velocities themselves; there is a switch from pronounced, low phase velocities in the 25-50 s range to locally high velocities at periods greater than 83 s. Second, this basic pattern of reversed anomalies has been corroborated by previous body wave studies. Many investigators have reported low P and/or S wave velocities in the shallowmost mantle in this area [*Carder, 1973; Jones et al., 1994; Savage et al., 1994; Wernicke et al., 1996; Jones and Phinney, 1998; Savage et al., 2003; Boyd et al., 2004*], although the geographic extent was not fully mapped due to limited station coverage. *Jones et al. [1994]* argued that there must be a paired, deeper, high velocity anomaly, because the travel time anomalies from teleseismic events were small despite the low velocities in the shallow mantle. *Jones and Phinney [1998]* reported the hint of the top of such a body beginning at a depth of about 60 km from converted phases. *Biasi and Humphreys [1992]* found high P-wave velocities at depths exceeding ~120 km in their tomographic image, but resolution was limited in this area due to poor station coverage. More recently, *Savage et al. [2003]* reported a large jump in P-wave velocity at 75-100 km based on Pn waveforms, which would represent the bottom of the anomalously low velocity zone and top of a high velocity anomaly, in agreement with the absence of the low-velocity anomaly at 90-110 km in our model. Finally, using an array of 24 broadband seismometers spanning the southern Sierra Nevada, *Boyd et al. [2004]* imaged a dipping high velocity anomaly at depths of 100 to 200 km underlying the shallow, low velocity anomaly.

In our images (Figure 14a), the high velocity anomaly beneath the eastern Sierra Nevada and Owens Valley may be connected to the high velocity anomaly beneath the southern Central Valley, in agreement with the conclusion of Boyd et al that the anomaly dips to the east. The existence and approximate lateral dimensions of the southern Central Valley anomaly, variously termed the Isabella anomaly or the Southern Great Valley anomaly, has long been known from P-wave tomography [*Aki, 1982; Biasi and Humphreys, 1992; Benz and Zandt, 1993; Zandt and Carrigan, 1993; Jones et al., 1994; Bijwaard et al., 1998*]. All these studies as well as ours show that this high velocity anomaly within the low velocity zone is not a slab-like body paralleling the Sierra Nevada, but is limited to a roughly circular area about 120 km in diameter. The depth extent was estimated to be on the order of 230 km in the body wave studies [*Biasi and Humphreys, 1992; Zandt and Carrigan, 1993*], but the depth is well constrained to be no greater than about 130 km (Figure 12 g and h) by the reversal to anomalously slow phase velocities beginning at a period of about 83 s (Figure 9e). These slow phase velocities at long periods lead to anomalously low velocities beneath the southern Great Valley at depths exceeding 130 km, again corroborated by the detailed body wave tomography of *Boyd et al. [2004]*. The high velocity, southern Central Valley anomaly reaches a maximum amplitude of about 6% in the low-velocity zone at 90 to 110 km, essentially eliminating the contrast between lithosphere and asthenosphere at that point and thus compatible with a model of foundering or sinking of the lower lithosphere.

The evidence for delamination of the lithosphere 4-8 My ago beneath the eastern

Sierra Nevada is very strong. The absence of a crustal root, the low seismic velocities in the uppermost mantle, the change from crustal eclogitic xenoliths at depths to 65 km in the Miocene to peridotitic in the Quaternary defining an apparent adiabatic temperature gradient leading to temperatures as high as 1150 °C near the base of the current crust [Ducea and Saleeby, 1996], the presence in peridotitic xenoliths of silicic melt inclusions that appear to be melted crust [Ducea and Saleeby, 1998a], low electrical conductivities indicating the presence of melt [Park, 2004], the pulse of potassic volcanism about 3.5 Ma [Manley *et al.*, 2000], and depths of origin of Pliocene and Quaternary basaltic magmas ranging from about 40 to 120 km [Feldstein and Lange, 1999; Wang *et al.*, 2002; Elkins-Tanton and Grove, 2003] all indicate that the lower lithosphere, including the eclogitic root to the Sierra batholith, detached and sank, replaced by upwelling, asthenospheric mantle that underwent partial melting during its ascent. The Quaternary episode of basaltic volcanism beginning about 1.5 Ma is confined primarily to the eastern edge of the Sierra Nevada including Owens and Long Valley [Manley *et al.*, 2000] and coincides with the region of lowest velocities from 50 to 90 km (Figure 12d,e and Figure 15). This recent episode could represent upwelling in response to westernmost Basin and Range extension that extends to shallower depths here than elsewhere in the Basin and Range [Wang *et al.*, 2002] due to the prior removal of the lithosphere.

One of the primary remaining questions is the fate of the delaminated lithosphere. A number of papers have focused on the high velocity Central Valley Anomaly as being the location of the downwelling track of the delaminated root [Ruppert *et al.*, 1998;

Saleeby et al., 2003; *Zandt*, 2003; *Zandt et al.*, 2004]. Noting the roughly cylindrical shape of this anomaly and its proximity to the circular shaped region of Pliocene mafic potassic volcanism, *Zandt* [2003] suggested that the lithosphere detached about 3.5 Ma and sank rapidly to the base of the asthenosphere, leaving a cold "tail" along its trail that is still downwelling. He noted that once a denser blob is detached, it should sink through a low-viscosity asthenosphere in less than 1 m.y., given viscosities of 10^{20} Pa-s or less and reasonable estimates of the density contrast, so the original lower lithosphere has probably sunk out of range of the tomographic images. In this scenario, the tail has subsequently been displaced to the SSW from its origin beneath the area of potassic volcanism by the "mantle wind", part of the global asthenospheric counterflow directed to the SSW, rather than to the east as envisioned by those invoking flow driven by the subducted Farallon plate. *Zandt et al* suggested that a locally thickened crust detected with receiver function techniques, [also partially detected by *Fliedner et al.* 1996], represents lower crust viscously dragged downward by the dripping lithospheric mantle. *Saleeby et al.*, presented a variant of this model in which the sinking lithospheric drip still contains the remnants of the original, convectively removed, subbatholith mantle lithosphere. Descent in their model presumably is slowed because the drip has never fully detached from the overlying lithosphere.

We image with confidence only the southern part of the Pliocene field of potassic volcanism, but we show that lithospheric detachment was not limited to that area, continuing south as far as the latitude of the Central Valley Anomaly (Figure 12d and e).

The burst of volcanism at ~ 3.5 Ma also was not confined just to the potassic area; it continued to the southern end of the detached area indicated by the low velocity region we image at depths of 50 to 90 [Manley *et al.*, 2000]. The area of potassic volcanism thus should not be taken as a unique indicator of where detachment took place. The potassic volcanism probably was triggered by detachment and consequent upwelling, but the potassic character was caused by an unusual composition of the upwelling mantle, which had apparently been previously metasomatized by a K-rich fluid [van Kooten, 1981; Mukhopadhyay and Manton, 1994; Feldstein and Lange, 1999; Farmer *et al.*; 2002 and Elkins-Tanton and Grove; 2003]. The existence of high velocities directly beneath the delaminated region removes the motivation for identifying the Central Valley Anomaly as the destination of the delaminated lithosphere. The foundering lithosphere may sink vertically. Indeed, Boyd *et al.* [2004] identify regions of garnet pyroxenite extending deep into the mantle beneath the eastern Sierra Nevada on the basis of V_p/V_s ratios and attenuation, which they interpret as the delaminated, eclogitic, crustal root of the mountain range.

In our image, it is not totally clear that the sinking beneath the eastern Sierra is physically connected to the foundering beneath the southern Central Valley. Boyd *et al.* show a continuous band of high P velocities dipping eastward from the Central Valley anomaly, but the S-wave anomalies are not as uniform, with adjacent but perhaps distinct anomalies similar to the maxima beneath the Central Valley at 90 to 110 km and beneath the eastern Sierra at 130 to 170 km (Figures 12 f and h,i). The V-shaped cone of

thickened crust observed beneath the Central Valley by *Zandt et al.* [2004] could either be caused by vertical sinking of the local lithosphere or by the viscous drag from an eastward plunging lithosphere. More coverage is needed to fully establish the shape beneath the region of Pliocene potassic volcanism to the NNE; coverage that should become available with the deployment of USArray.

Upwelling beneath Salton Trough. A moderately low velocity anomaly is imaged beneath the Salton Trough at all depths down to 200 km. The recent surface wave tomographic study by *Tanimoto and Sheldrake* [2002] showed a similar low velocity anomaly, but the limited period range prevented good depth resolution. This anomaly has also been imaged in previous P wave tomographic studies [*Raikes*, 1980; *Humphreys and Clayton*, 1990; *Biasi and Humphreys*, 1992; *Zhao et al.*, 1996]. Our observations of this low velocity anomaly are similar to these studies in overall pattern. *Humphreys and Clayton* [1990] showed a low anomaly throughout the upper 70 to 100 km; *Zhao et al.* [1996] observed a southeast trending anomaly extending to about 150 km with largest amplitudes from 60 to 100 km. Our model has the largest velocity contrast from 70 to 110 km, with the center of the anomaly shifted to the west of the Salton Sea (Figure 12e and f). In the 90 to 130 km depth range, it is the slowest spot in southern California. At greater depths, the anomaly is elongated to the southeast and shifts to the southeast of the Salton Sea (Figure 12 h and i).

The extension of the Salton trough anomaly into the low-velocity zone suggests that there may be a component of dynamic upwelling and melting associated with the

extensional tectonics. Purely passive upwelling in response to the extension and subsequent conductive cooling near the surface would not be expected to produce an anomaly in the asthenosphere, which should already follow an adiabatic gradient. The anomaly is more pronounced and distinct in our Rayleigh-wave-derived S-wave images than in most P-wave tomographic studies (e.g. *Kohler et al.*, 2003), suggesting that melt probably plays an important role in creating it, because melt may more strongly affect S than P velocity.

Lithospheric drips beneath the Transverse Range. The well-known upper mantle high velocity anomaly beneath the Transverse Range [*Hadley and Kanamori*, 1977; *Raikes*, 1980; *Walck and Minster*, 1982; *Humphreys et al.*, 1984] is imaged from 50 to 150 km (Figure 14b). The high velocity anomaly is most pronounced at the eastern and western ends of the Transverse Range. In the western end, the high velocity extends south to the offshore region. The scale of the high velocity anomaly becomes smaller with increasing depth. Previous P-wave tomographic studies [*Humphreys and Clayton*, 1990; *Zhao et al.*, 1996; *Kohler*, 1999; *Kohler et al.* 2003] show that this feature is ~60 km thick and extends most deeply at the eastern end, in agreement with our observations, but the body wave studies indicate that the maximum depth is 200 to 250 km. Our images show that the high velocity only extends to about 150 km. One possible reason for this difference in the depth range between surface wave tomography and body wave tomography could be vertical smearing effects in the body wave tomography. Since the incident angles of teleseismic body waves are very steep usually, it is hard to constrain the depth range of

velocity anomalies accurately and they tend to be smeared to longer features along ray paths, particularly if one includes the weaker fringes of the anomalies in the interpretation. Fundamental mode Rayleigh waves also lose resolving power at these depths, but we should be able to detect an anomaly extending from 150 to 250 km. Another possible difference in the depth range cited is simply interpretation of the images. *Kohler et al.* [2003] show that the high velocity region broadens beneath 150 km, blending into an anomaly that covers much of southern California south of the Garlock fault. Therefore we conclude that the high velocity anomalies extend only to about 150, or perhaps 170, km.

The upper mantle high velocity anomaly was interpreted by *Bird and Rosenstock* [1984] as a slab-like mantle convective downwelling induced by oblique convergent motion between Pacific plate and North American plate across the San Andreas Fault, with the descending mantle decoupled from the crust. Subsequent authors [*Humphreys and Hager*, 1990; *Kohler*, 1999] argued that the entire subcrustal lithosphere on both sides of the convergent zone descends into the asthenosphere due to the gravity instability initiated by the convergence. In these simple models, the depth extent can be predicted kinematically by the integrated convergence since initiation of the bend in the San Andreas 5 to 10 m.y. ago. Our results suggest that instead of a simple, 2-D tabular form, the small scale convective instabilities take the form of localized drips that could draw in lower lithosphere from both along and across strike, breaking the direct kinematic predictability. At depths greater than 90 km, and perhaps even shallower, the

Transverse Range anomaly breaks up into two roughly circular anomalies with a gap or near gap at about 118.5°W. The western anomaly, beginning under the Channel Islands, dips to the NNE, while the eastern anomaly is nearly vertical. *Humphreys and Clayton* [1990] and *Kohler et al.* [2003] show similar breaks in their P-wave tomography images at the same longitude, although they do not find as strong a western anomaly, perhaps due to the scarcity of stations offshore. *Kohler and Davis* [1997] and *Kohler* [1999] report that there is a local zone of crustal thickening directly overlying the eastern drip, similar to that observed above the Central Valley anomaly, suggesting that crust and mantle are not completely decoupled. It is possible that other drips may have detached previously and sunk out of detection range.

Thin crust and cool lithosphere beneath the Borderlands. Beneath the California Borderland, we observe high velocity anomalies. From the Moho to 50 km, our model indicates high velocities south and east of Catalina and San Clemente islands. In this area, *Zhu and Kanamori* [2000] had no crustal control, because there are no stations where converted phases could be detected. Consequently, our interpolated crustal model has average crustal thicknesses of close to 30 km (Figure 13), but there is every reason to expect that the ~22 km thick crust adjacent to Catalina [*Nazareth and Clayton*, 2003] continues farther south along the coast, as the Catalina schist belt, representing middle crustal rocks uplifted and exposed during extension, continues at least as far as 31°S [*Bohannon and Geist*, 1998]. Thus, the velocity anomalies in the uppermost mantle layer and lower crust simply indicate that model crust should be thinner in this

area.

From 50 to 70 km beneath the Borderlands, the shear velocity in the mantle is uniformly about 2.5% faster than in the reference model, or about 4.4 km/s (Figure 12d). This increase in velocity and the 3 to 4% increase in the northern Borderlands at depths greater than 70 km are compatible with the increase in lithospheric thickness inferred from SS waveforms and SS-S traveltimes assuming constant lid and low-velocity zone velocities [*Melbourne and Helmberger, 2001*]. Most of the extension in the Borderlands occurred in early to mid-Miocene, as the transfer to the Pacific plate occurred earlier here than farther inland [*Bohannon and Geist, 1998*], giving more time for the lithosphere to cool. There may also be fragments of oceanic lithosphere captured in the Borderlands, which, together with the expected lower temperatures, could account for the higher velocities in the lithosphere. At the northern end of the Borderlands, in the vicinity of the Channel Islands, the lithospheric anomaly merges with the deeper (> 90 km) anomaly described above that we associate with a mantle drip beneath the western end of the Transverse Ranges.

Peninsular Range drip and Mojave upwelling. All of the features described above in the Sierra Nevada, Central Valley, Transverse Ranges, Salton Trough and Borderlands regions have been detected and characterized in previous seismological investigations using other techniques. One advantage of Rayleigh wave tomography is that it provides more uniform resolution that is somewhat less dependent on the local density of seismic stations than body wave tomography. Having established the credibility of the Rayleigh

wave tomography by comparison with known features, we focus here on two deep anomalies in regions of relatively sparse station coverage that have previously escaped detection: a high velocity anomaly beneath the Peninsular Range and a low velocity anomaly beneath the Mojave desert.

Beneath the northern Peninsular Range, there is a high velocity anomaly at depths greater than about 130 km (Figures 12 h,i and 14c). In our phase velocity maps, this is the strongest anomaly at the longest periods (Figure 9g), exceeding 3%, so we are probably just detecting the top of the body and cannot establish its vertical extent. Our modelling may also underestimate the depth to the top; because we restrict lateral velocity variations to the upper 200 km, a deeper anomaly that is still within the range of detection will be forced to shallower levels.

The Peninsular Range anomaly may represent a sinking drip or blob that has completely detached from the overlying lithosphere in a process that may be very similar to the delamination of the eastern root of the Sierra Nevada. The Peninsular Ranges Batholith along with the Sierra Nevada batholith formed the continuous, Mesozoic California Batholith that has subsequently been disrupted by strike-slip faulting and extension in southern California [e.g. , Silver and Chappell, 1988]. Like the Sierra Nevada batholith, the eastern Peninsular Ranges Batholith probably was underlain by an eclogitic residual root [*Gromet and Silver, 1987*]. An eclogitic root forms a gravitationally metastable layer within the lithosphere that, in the Sierra Nevada, delaminated only after extension began in the adjacent Basin and Range province.

Adjacent extension could also be the trigger for delamination of the lithosphere beneath the Peninsular Range, but extension began earlier at 15-20 Ma in the Borderlands region [Luyendyk, 1991; Bohannon and Geist, 1998] before switching eastward to the Gulf of California, so delamination may have begun sooner and progressed further. Perhaps upwelling of the asthenosphere replacing the delaminated lithosphere has ceased at shallow levels, or never reached as shallow as the Sierra Nevada detachment, because we do not see the pronounced low velocity anomalies that are present beneath the eastern edge of the Sierra Nevada at 50 to 70 km. But, perhaps the low velocity region 70 to 110 km deep west of the Salton Sea and near the San Jacinto fault represents such an upwelling zone that enhances the upwelling associated with extension in the Salton trough area, displacing it westward. Models show that lithospheric delamination does not necessarily produce melting. The occurrence of melting is dependent on the viscosity structure of the lithosphere and the release of volatiles from the descending drip [Elkins-Tanton, 2005].

The second new feature is a low velocity anomaly centered at about 35.5 °N, 117 °W in the northern Mojave desert. Like the anomaly beneath the Peninsular Range, we see it clearly in the longest period phase velocities (Figure 9f,g) and thus can only resolve the top of the anomalous body (Figure 12 h,i). It is not clear what tectonic processes created this anomaly, but it may represent convective upwelling that is required to balance downwelling elsewhere in the system.

Azimuthal anisotropy

Shear wave splitting measurements at many stations in southern California [*Savage and Silver, 1993; Ozalaybey and Savage, 1995; Liu et al. 1995; Polet and Kanamori, 2002*] show a nearly consistent fast direction close to E-W with splitting time ranging from 0.75 to 1.5 seconds. However, because the ray paths of SKS phases used in the analysis are nearly vertical, the depth distribution of anisotropy cannot be inferred from the shear wave splitting data alone. Taking advantage of the sensitivity of Rayleigh waves of different periods to structure at different depths and the fact that the fast direction for Rayleigh wave propagation should be the same as the fast direction for shear wave splitting if the anisotropic structure has a horizontal symmetry axis with orthorhombic (or higher order) symmetry, we can solve for the vertical distribution of anisotropy.

In the inversion for phase velocities, we simultaneously solve for isotropic term A_0 and azimuthal term A_1 and A_2 (eq. 1). The peak-to-peak anisotropy is $2 \times (A_1(\omega)^2 + A_2(\omega)^2)^{\frac{1}{2}} / A_0(\omega)$ and the fast direction is $\frac{1}{2} \tan^{-1} \left(\frac{A_2(\omega)}{A_1(\omega)} \right)$. Standard errors for the strength and fast direction can be calculated from the variation of A_1 and A_2 using an error propagation technique [*Clifford, 1975*]. Mathematically, we can solve for the 2-D variation of anisotropy on the scale of a grid cell. However, when we introduce 2-D anisotropy terms A_1 and A_2 , there are three times as many parameters as there are for isotropic phase velocity A_0 alone, and they are not resolved very well. From shear wave

splitting observations in southern California [Liu, *et al.* 1995; Polet and Kanamori, 2002], we know that the lateral variation of anisotropy in Southern California is quite small. Therefore it is reasonable as a first approximation to assume that anisotropy is uniform in the entire southern California region while isotropic phase velocities are allowed to vary laterally. Later we consider variations based on prescribed geographic regions to test specific hypotheses.

The average azimuthal anisotropy at various periods in southern California is shown in Figure 16. Because we assume homogeneity, the sensitivity kernel is simply proportional to path length within the study area. The standard deviations of amplitude have been plotted as error bars, which are $\sim 0.15\%$ at periods less than 67s and increase with period to 0.6% at 143 s. The standard derivations of the fast directions are $\sim 3^\circ$ at periods less than 67s and $\sim 10^\circ$ at periods longer than 67 s. At periods from 25 s to 67 s, the strength is very uniform and averages about 1.7% peak-to-peak amplitude, about half the amplitude of the azimuthal anisotropy in young seafloor in the Pacific found within local arrays [Forsyth *et al.*, 1998; Weeraratne *et al.*, 2005]. At longer periods, the strength decreases to about 1% . The variation of fast direction with period is small. At periods less than 60 s, the average direction is about $N82^\circ E$, rotating to slightly south of east at longer periods, but with larger uncertainty. The change in anisotropy with period suggests that there may be a somewhat different and weaker orientation in the asthenosphere than the lithosphere, but the change in direction is small enough that it would be difficult to detect with azimuthal variations in shear wave splitting, consistent

with the single-layer anisotropy models proposed for southern California [*Liu, et al.* 1995; *Polet and Kanamori*, 2002; *Davis*, 2003].

There is a potential tradeoff between anisotropy terms A_1 and A_2 and lateral variations in the azimuthally averaged velocity term A_0 when they are jointly inverted. In principle, in ray theory the anisotropic effects on travel time can be perfectly modeled by allowing strong lateral variations in isotropic velocities on a distance scale significantly smaller than the separation between stations. In this study, the lateral variations of phase velocities are limited by smoothing with a 65-km characteristic length, which, combined with the averaging inherent in the Fresnel zones of the response kernels and the relatively high density of stations, prevents short wavelength velocity variations from mimicking the effects of azimuthal anisotropy. With our excellent azimuthal distribution of sources, we find no significant difference between the lateral variations in A_0 inverted without azimuthal terms, shown in Figure 9, and A_0 in models that include the azimuthal terms. Thus, there is no indication that neglect of anisotropy introduces artifacts into our phase velocity maps.

At long periods, however, it is possible that lateral variations in structure influence the apparent anisotropy. For example, at 125 s the wavelength is about 500 km, which is significantly larger than the scale of velocity variations we find and greater than the width of features like the Sierra Nevada, Peninsular Range, and Great Valley. The variation of phase velocities at long periods could behave somewhat more like a laterally uniform region with shape-preferred anisotropy than a laterally heterogeneous region,

just like layered sediments produce effective transverse anisotropy when the layering is on a scale of less than one wavelength. If that were the case, we would underestimate the lateral heterogeneity and overestimate the azimuthal anisotropy due to truly small-scale structure such as lattice-preferred orientation of crystals or alignment of cracks. The change of fast directions at the longest periods to being more parallel to the plate boundary and the dominant tectonic trends could possibly be due to this layering effect on anisotropy instead of intrinsic anisotropy, although the fact that the planform of the anomalies we do resolve tends to be irregular or circular in shape rather than linear suggests that it may not be an important effect. In order to quantitatively evaluate the tradeoff, we need to investigate the effects of lateral heterogeneities on apparent anisotropy of long-period Rayleigh waves by modeling Rayleigh wave propagation through laterally heterogeneous media with the full elastic wave equations in models that simulate potential structures in southern California, which is beyond the scope of this current study.

The Rayleigh wave azimuthal anisotropy and the shear-wave splitting delay times between 0.75 and 1.5 s require that anisotropy extend through both lithosphere and asthenosphere. Assuming 4% anisotropy for upper mantle materials, *Polet and Kanamori* [2002] estimated an anisotropic layer about 100-200 km thick, according to the range of delay times. Combining information from P wave polarization [*Schulte-Pelkam, et al.*, 2001], Pn times [*Hearn, 1996*], Rayleigh and Love velocities, and SKKS and SKS splitting, *Davis* [2003] concluded that anisotropy is distributed throughout the upper 200

km of the mantle up to the base of the crust. In our study, the strength of azimuthal anisotropy is $\sim 1.7\%$ at short periods and $\sim 1\%$ at long periods. Rayleigh waves at periods shorter than 50 s are primarily sensitive to the lithosphere, including the crust. The upper crust is anisotropic, probably due to the orientation of cracks, but the maximum splitting times in the upper crust in the Los Angeles basin area are only about 0.12 s and the fast direction is \sim N-S [Li *et al.*, 1994], orthogonal to the fast direction observed for teleseismic wave splitting and azimuthal anisotropy. The lower crust is likely to be more isotropic. To yield 1.7% anisotropy of the short-period Rayleigh waves requires 2-3% shear wave anisotropy in the mantle part of the lithosphere. The contribution to shear wave splitting from the lithosphere from 30 to 90 km is thus approximately 0.25 to 0.4 s. The average degree of anisotropy in the asthenosphere must be significantly smaller. Taking an average value of $\sim 1\%$ requires that the non-lithospheric contribution to splitting extend over a depth range on the order of 300 km to produce a total average splitting of about 1.1 s.

In 1995, Liu *et al* first argued that the cause of the E-W fast orientation might be related to late Cenozoic N-S contraction in southern California as manifested in the creation of the Transverse Ranges and contraction in the Mojave block [Bartley *et al.*, 1990]. In order to more quantitatively evaluate the relationship between the fast directions with the direction of compressional stresses, Polet and Kanamori [2002] plotted the fast directions of anisotropy and the maximum compressive stress directions from the world Stress Map together. They found that the fast direction is nearly

orthogonal to the maximum compressive stress in southern California and argued that this perpendicularity is consistent with the alignment of the a-axis of olivine perpendicular to the direction of lithospheric shortening. This mechanism, however, does not explain the larger contribution to splitting from the asthenosphere, which is unlikely to be directly coupled to any lithospheric shortening. Indeed, in central California in the vicinity of the major strike-slip faults of the Bay area, two layers of anisotropy are required to explain the splitting [*Savage and Silver, 1993; Ozalaybey and Savage, 1995; Liu et al., 1995*]; although it is difficult to uniquely resolve the directions [*Hartog and Schwartz, 2001*], the fast direction in the upper layer may be aligned parallel to the San Andreas fault and the lower, sublithospheric layer E-W. In southern California, two directions are not resolved, even close to the San Andreas [*Polet and Kanamori, 2002; Davis, 2003*].

One of most likely causes of anisotropy in the asthenosphere is the flow-induced, lattice-preferred orientation of olivine. *Ozalaybey and Savage [1995]* argued that asthenospheric flow in the slabless window left behind the Farallon plate could create the E-W fast direction. *Silver and Holt [2002]*, noting the small change in orientation of SKS fast directions from slightly clockwise of E-W near the coast to ENE in the western Basin and Range including Walker Lane [*Polet and Kanamori, 2002*], attributed the change in direction to the different motions of the Pacific and North American plates relative to flow in the underlying mantle. They predicted an eastward mantle flow with velocity 5.5 ± 1.5 centimeters per year; flow which could be produced by the sinking Farallon

slab. We are not convinced that the change in orientation occurs at the plate boundary. It seems more to be a change associated with extension in the Basin and Range province. Following the model of *Silver and Holt*, we performed an experiment in which we subdivided the region into two areas divided by the San Andreas fault in which the azimuthal anisotropy of Rayleigh waves is allowed to be different. We found no significant difference in anisotropy in the two regions.

It is perhaps surprising that the shear wave splitting orientation is so uniform if there are convective upwellings and downwellings in the asthenosphere, as indicated by our surface wave tomography and previous body wave studies, that should alter the local flow directions. Perhaps the uniformity in direction is caused by a relatively uniform lithospheric fabric and the decrease in amplitude of the average azimuthal anisotropy at longer periods is associated with a more chaotic pattern in the asthenosphere. The variations in amplitude of splitting and the smaller variations in direction could be caused by local variations in the relative contributions of asthenosphere and lithosphere. *Polet and Kanamori* [2002] noted that they could not find any high-quality, split SKS phases at stations ISA and MLAC above the Isabella or Central Valley anomaly and the Mammoth Lakes/Long Valley anomalies, respectively. Thus, there may be local disruptions of the overall shearing flow between the lithosphere and deeper mantle due to small scale convection, but if the anisotropic layer extends to depths as great as 400 km and these convective features are primarily drips or local upwellings, then they may occupy a small fraction of the total volume of the anisotropic layer and cause only relatively minor

perturbations in the overall pattern of flow associated with plate motion.

Conclusions

Using Rayleigh wave phase and amplitude data, we have solved for azimuthal anisotropy and lateral variations in phase velocity in southern California. The use of finite-frequency response kernels and an approximate representation of the incoming wavefields, coupled with a high density of broadband stations and excellent azimuthal distribution of sources allows unprecedented resolution to periods as long as 140 s. A one-dimensional shear wave velocity profile based on the average phase velocities shows a low velocity zone in the upper mantle underlying a high velocity lithospheric lid. The velocity contrast between them is about 3.5%. The thickness of lithosphere is ~90 km, but the average shear velocity in the lid of 4.35 km/s is significantly less than in other regions with comparable thickness, indicating average temperatures in the lid are probably several hundred degrees hotter and that there is likely to be melt present in the asthenosphere.

In the uppermost mantle, there is a low velocity anomaly beneath the eastern edge of the southern Sierra Nevada and the adjoining Walker Lane region that is directly underlain by a high velocity anomaly. This velocity pattern supports the argument that the lithosphere detached from the crust and sank into the surrounding mantle and the lower, hotter asthenosphere upwelled and filled the space left by the sinking lithosphere, undergoing partial melt as it rose. The high velocity anomaly at depth is connected to a

high velocity anomaly beneath the southern Central Valley forming a slab-like structure. A moderate low velocity anomaly is observed beneath the Salton Trough region associated with the extensional tectonics. The well-known, high velocity anomaly associated with downwelling lithosphere beneath the Transverse Range is imaged extending down to ~ 150 km, rather than the 200 to 250 km suggested in previous studies. We also image the top of a high velocity anomaly beneath the northern Peninsular Range that may be a lithospheric drip that has fully detached from the overlying plate. Another deep anomaly, a north-south-trending, low-velocity body, is found beneath the northeastern Mojave desert. The shape of these anomalies and their association with tectonic and volcanic features on the surface strongly support the existence of small-scale convection beneath southern California and suggest that the dominant form of convection is in the form of 3-D lithospheric drips and asthenospheric upwellings rather than 2-D, slab-like sheets.

Azimuthal anisotropy is found in a joint inversion including lateral variations of phase velocities. The strength of anisotropy is $\sim 1.7\%$ at periods shorter than 67s and decreases to $\sim 1\%$ at longer periods. This strength combined with the measurements of shear-wave splitting time from other studies constrain the thickness of the anisotropic layer to be about 350 km. The average fast direction is nearly E-W, which is consistent with shear wave splitting measurements. The E-W fast direction is attributed partially to the N-S compressive stress in the lithosphere and partially to asthenospheric flow at depth, which may be locally disrupted by convective features.

References

- Aki, K., Three-dimensional seismic inhomogeneities in the lithosphere and asthenosphere: Evidence for decoupling in the lithosphere and flow in the asthenosphere, *Rev. Geophys. Space Phys.*, 20, 161-170, 1982.
- Atwater T., Plate tectonic history of southern California with emphasis on the western Transverse Ranges and Santa Rosa Island, in Weigang, P.W., ed., Contributions to the geology of the Northern Channel Islands, Southern California: American Association of Petroleum Geologists, Pacific Section, MP 45, P. 1-8, 1998.
- Bartley, J.M., A.F. Glazner, and E.R. Schermer, North-south contraction of the Mojave block and strike-slip tectonics in southern California, *Science*, 248, 1398-1401, 1990.
- Benz, H.M., and G. Zandt, Teleseismic tomography: Lithospheric structure of the San Andreas Fault system in northern and central California, in Iyer, H.M. and K. Hirahara, eds., Seismic tomography: Theory and practice, Chapman and Hall, NY, p. 440-465, 1993.
- Biasi, G.P. and E.D. Humphreys, P-wave image of the upper mantle structure of central California and southern Nevada, *Geophys. Res. Lett.*, 19, 1161-1164, 1992.
- Bijwaard, H. W. Spakman, and E.R. Engdahl, Closing the gap between regional and global travel time tomography, *J. Geophys. Res.*, 103, 30055-30078, 1998.
- Bird, P., and R.W. Rosenstock, Kinematics of present crust and mantle flow in southern California, *Geol. Soc. Am. Bull.*, 95, 946-957, 1984.

- Bohannon, R.G. and E. Geist, Upper crustal structure and Neogene tectonic development of the California continental borderland, *Geol. Soc. Am. Bull.*, 110, 779-800, 1998.
- Boyd, O. S., C. H. Jones, and A.F. Sheehan, Foundering lithosphere imaged beneath the southern Sierra Nevada, California, USA, *Science*, 305, 660-662, 2004.
- Carder, D.S., Trans-California seismic profile, Death Valley to Monterrey Bay, *Bull. Seis. Soc. Am.*, 63, 571-586, 1973.
- Clifford, A.A., *Multivariate error analysis*, John Wiley, Hoboken, N.J., 1975.
- Crough, S.T., and G.A. Thompson, Upper mantle origin of Sierra Nevada uplift, *Geology*, 5, 396-399, 1977.
- Dalton, C., and G. Ekstrom, Surface wave constraints on Q of the upper mantle: Isolating the signal of attenuation, *EOS Trans. AGU*, 84(46), *Fall Meeting Suppl.* Abstr. S22B-0444, 2003.
- Davis, P.M., Azimuthal variation in seismic anisotropy of the southern California uppermost mantle, *J. Geophys. Res.*, 108(B1), 2052, doi:10.1029/2001JB000637, 2003.
- DeBayle, E. and M. Sambridge, Inversion of massive surface wave data sets: Model construction and resolution assessment, *J. Geophys. Res.*, 109, B02316, doi:10.1029/2003JB002652, 2004.
- Ducea, M.N. and J. B. Saleeby, Buoyancy sources for a large, unrooted mountain range, the Sierra Nevada, California: Evidence from xenolith thermobarometry, *J. Geophys. Res.*, 101, 8229-8244, 1996.
- Ducea, M.N., and J.B. Saleeby, Crustal recycling beneath continental arcs: silica-rich

- glass inclusions in ultramafic xenoliths from the Sierra Nevada, California, 1998a.
- Ducea, M.N., and J.B. Saleeby, A case for delamination of the deep batholithic crust beneath the Sierra Nevada, California, *Int. Geol. Rev.*, *40*, 78-93, 1998b.
- Elkins-Tanton, L.T., and T.L. Grove, Evidence for deep melting of hydrous, metasomatized mantle: Pliocene high potassium magmas from the Sierra Nevadas, *J. Geophys. Res.*, *108*, p. 2350, doi 10.1029/2002JB002168, 2003.
- Elkins-Tanton, L.T., Continental magmatism, volatile recycling, and a heterogeneous mantle caused by lithospheric Rayleigh-Taylor instabilities, *J. Geophys. Res.*, submitted, 2005.
- Faul, U.H. and I. Jackson, The seismological signature of temperature and grain size variations in the upper mantle, *Earth Planet. Sci. Lett.*, *234*, 119-234, 2005.
- Feldstein, S.N. and R.A. Lange, Pliocene potassic magmas from the Kings River region, Sierra Nevada, California: Evidence for melting of a subduction-modified mantle, *J. Petrol.*, *40*, 1301-1320, 1999.
- Fliedner, M. M., and S. Ruppert, Three-dimensional crustal structure of the southern Sierra Nevada from seismic fan profiles and gravity modeling, *Geology*, *24*, 367-370, 1996.
- Forsyth, D.W. and Li, A., 2005. Array-analysis of two-dimensional variations in surface wave phase velocity and azimuthal anisotropy in the presence of multi-pathing interference, *Seismic Data Analysis and Imaging with Global and Local Arrays*, (A. Levander and G. Nolet, ed.), AGU Geophysical Monograph, in press.

- Forsyth, D.W., S. Webb, L. Dorman, and Y. Shen, Phase velocities of Rayleigh waves in the MELT experiment on the East Pacific Rise, *Science*, 280, 1235-1238, 1998.
- Friederich, W., Wave-theoretical inversion of teleseismic surface waves in a regional network: Phase velocity maps and a three-dimensional upper-mantle shear-wave velocity model for southern Germany, *Geophys. J. Int.*, 132, 203-225, 1998.
- Friederich, W.E., E. Wielandt, and S. Stange, Multiple forward scattering of surface waves: comparison with an exact solution and Born single-scattering methods, *Geophys. J. Int.*, 112, 264-275, 1993.
- Friederich, W., E. Wielandt, and S. Stange, Non-plane geometries of seismic surface wavefields and their implications for regional-scale surface wave tomography, *Geophys. J. Int.*, 119, 931-948, 1994.
- Friederich, W., and E. Wielandt, Interpretation of seismic surface waves in regional networks: joint estimation of wavefield geometry and local phase velocity - Method and tests, *Geophys. J. Int.*, 120, 731-744, 1995.
- Grand, S. P. and D. V. Helmberge, Upper mantle shear structure of North American, *Geophys. J. R.*, 76, 399-438, 1984.
- Gromet, L.P. and L.T. Silver, REE variations across the Peninsular Ranges batholith: implications for batholithic petrogenesis and crustal growth in magmatic arcs, *J. Petrol.*, 28, 75-125, 1987.
- Hadley, D.M. and H. Kanamori, Seismic structure of the Transverse Ranges, California, *Geol. Soc. Am. Bull.*, 88, 1461-1478, 1977.

- Hartog, R., and S.Y. Schwartz, Depth-dependent mantle anisotropy below the San Andreas fault system: apparent splitting parameters and waveforms, *J. Geophys. Res.*, 106, 4155-4167, 2001.
- Hauksson, E., Crustal structure and seismicity distribution adjacent to the Pacific and North American plate boundary in southern California, *J. Geophys. Res.* 105, 13,875-13,904, 2000.
- Hearn, T.M., Anisotropic *Pn* tomography in the western United States, *J. Geophys. Res.*, 101, 8403-8414, 1996.
- Helmberger, D., X. Song, and L. Zhu, Crustal complexity from regional waveform tomography: aftershocks of the 1992 Landers earthquake, California, *J. Geophys. Res.*, 106, 609-620, 2001.
- Humphreys, E.D., R.W. Clayton, and B.H. Hager, A tomographic image of mantle structure beneath southern California, *Geophys. Res. Lett.*, 11, 625-627, 1984.
- Humphreys, E.D. and B. H. Hager, A kinematic model for the late Cenozoic development of southern California crust and upper mantle, *J. Geophys. Res.*, 95, 19,747-19,762, 1990.
- Humphreys, E.D., and R. W. Clayton, Tomographic image of the southern California mantle, *J. Geophys. Res.*, 95, 19,725-19,746, 1990.
- Jackson, I., J.D. FitzGerald, U.H. Faul, and B.H. Tan, Grain size sensitive seismic wave attenuation in polycrystalline olivine, *J. Geophys. Res.*, 107, doi:10.1029/2001JB001225, 2002.

- Jones, C.H., H. Kanamori, and S.W. Roecker, Missing roots and mantle "drips": Regional Pn and teleseismic arrival times in the southern Sierra Nevada and vicinity, California, *J. Geophys. Res.*, *99*, 4567-4601, 1994.
- Jones, C.H., and R.A. Phinney, Seismic structure of the lithosphere from teleseismic converted arrivals observed at small arrays in the southern Sierra Nevada and vicinity, California, *J. Geophys. Res.*, *103*, 10065-10090, 1998.
- Kohler M. D., Lithospheric deformation beneath the San Gabriel Mountains in the southern California Transverse Range, *J. Geophys. Res.*, *104*, 15,025-15041, 1999.
- Kohler, M.D., and P.M. Davis, Crustal thickness variations in southern California from Los Angeles Region Seismic Experiment passive phase teleseismic travel times, *Bull. Seis. Soc. Am.*, *87*, 1330-1344, 1997.
- Kohler, M. D., H. Magistrale, and R. W. Clayton, Mantle Heterogeneities and the SCEC reference three-dimensional seismic velocity model version 3, *Bull. Seism. Soc. Am.*, *93*, 757-774, 2003.
- Larsen, S., and R. Reilinger, Age constraints for the present fault configuration in the Imperial Valley, California: Evidence for northwestward propagation of the Gulf of California rift system, *J. geophys. Res.*, *96*, 10,339-10,346, 1991.
- Li, A., D.W. Forsyth, and K. M. Fischer, Shear velocity structure and azimuthal anisotropy beneath eastern North American from Rayleigh wave inversion, *J. Geophys. Res.*, *108*(B8), 2362, doi:10.1029/2002JB002259, 2003.
- Li, Y.-G., T.-L. Teng, and T. L. Henyey, Shear wave splitting observations in the northern

- Los Angeles basin, southern California, *Bull. Seis. Soc. Am.*, 84, 307-323, 1994.
- Liu, H., Davis, P.M. and Gao, S., SKS splitting beneath southern California, *Geophys. Res. Lett.*, 22, 767-770, 1995.
- Lonsdale, P., Geology and tectonic history of the Gulf of California, in *The Geology of North America*, vol. N, *the Eastern Pacific Ocean and Hawaii*, edited by E. L. Winterer, D. M. Hussong, and R. W. Decker, pp. 449-521, Geol. Soc. Am., Boulder, Colo., 1989.
- Luyendyk, B.P., A model for Neogene crustal rotations, transtension, and transpression in southern California, *Geol. Soc. Am. Bull.*, 103, 1528-1536, 1991.
- Magistrale, H., S. Day, R. W. Clayton, and R. Graves, The SCEC southern California reference three-dimensional seismic velocity model version 2, *Bull. Seism. Soc. Am.*, 90, S65-S76, 2000.
- Manley, C.R., A.F. Glazner, and G.L. Farmer, Timing of volcanism in the Sierra Nevada of California: Evidence for Pliocene delamination of the batholithic root?, *Geology*, 28, 811-814, 2000.
- Melbourne, T., and D. Helmberger, Mantle control of plate boundary deformation, *Geophys. Res. Lett.*, 28, 4003-4006, 2001.
- Mukhopadhyay, B. and W.I. Manton, Upper-mantle fragments from beneath the Sierra Nevada batholith: partial fusion, fractional crystallization, and metasomatism in a subduction-related ancient lithosphere, *J. Petrol.*, 35, 1417-1450, 1994.
- Nazareth, J.J., and R.W. Clayton, Crustal structure of the Borderland-continent transition

- zone of southern California adjacent to Los Angeles, *J. Geophys. Res.*, *108(B8)*, 2404, doi:10.1029/2001JB000223, 2003.
- Nishimura, C.E., and D.W. Forsyth, The anisotropic structure of the upper mantle in the Pacific, *Geophys. J.*, *96*, 203-229, 1989.
- Ozalaybey, S. and Savage M.K., Shear wave splitting beneath western United States in relation to plate tectonics, *J. Geophys. Res.*, *100*, 18,135-18149, 1995.
- Paulssen, H., Crustal anisotropy in southern California from local earthquake data, *Geophys. Res. Lett.*, *31*, L01601. doi:10.1029/2003GL018654, 2004.
- Park, S.K., Mantle heterogeneity beneath eastern California from magnetotelluric measurements, *J. Geophys. Res.*, *109*, B09406, doi:10.1029/2003JB002948, 2004.
- Polet, J., and H. Kanamori, Anisotropy beneath California: shear wave splitting measurements using a dense broadband array, *Geophys. J. Int.*, *149*, 313-327, 2002.
- Polet, J., and H. Kanamori, Upper-mantle shear velocities beneath southern California determined from long-period surface waves, *Bull. Seis. Soc. Am.*, *87*, 200-209, 1997.
- Pollitz, F.F., Regional velocity structure in northern California from inversion of scattered seismic surface waves, *J. Geophys. Res.*, *104*, 15043-15072, 1999.
- Press, F., Determination of crustal structure from phase velocity of Rayleigh waves, I, Southern California, *Geol. Soc. Am. Bull.*, *67*, 1647-1658, 1956.
- Raikes, S.A., Regional variations in upper mantle structure beneath southern California, *Geophys. J. R. Astr. Soc.*, *63*, 187-216, 1980.
- Rudnick, R.L., W. F. McDonough, and R.J. O'Connell, Thermal structure, thickness and

- composition of continental lithosphere, *Chem. Geology*, *145*, 395-411, 1998.
- Ruppert, S., M.M. Flidner, and G. Zandt, Thin crust and active upper mantle beneath the southern Sierra Nevada in the western United States, *Tectonophys.*, *286*, 237-252, 1998.
- Rychert, C.A., K.M. Fischer, and S. Rondenay, A sharp lithosphere-asthenosphere boundary imaged beneath eastern North America, *Nature*, 2005.
- Saito, M., DISPER80: A subroutine package for the calculation of seismic normal-mode solutions, in, *Seismological Algorithms*, edited by Doornbos, D. J., Academic Press, 293-319, 1988.
- Saltus, R., and A. Lachenbruch, Thermal evolution of the Sierra Nevada: Tectonic implications of new heat flow data, *Tectonics*, *10*, 325-344, 1991.
- Savage, B., C. Ji, and D. V. Helmberger, Velocity variation in the uppermost mantle beneath the southern Sierra Nevada and Walker Lane, *J. Geophys. Res.*, *108*(B7), doi: 10.1029/2001JB001393, 2003.
- Savage, M. K., and P. G. Silver, Mantle deformation and tectonics: constraints from seismic anisotropy in the western United States, *Phys. Earth Planet. Inter.*, *78*, 207-227, 1993.
- Savage, M.K., L. Li, J.P. Eaton, C.H. Jones, and J.N. Brune, Earthquake refraction profiles of the root of the Sierra Nevada, *Tectonics*, *13*, 803-817, 1994.
- Schulte-Pelkum, V., G. Masters, and P. Shearer, Upper mantle anisotropy from long-period P polarization, *J. Geophys. Res.*, *106*, 21917-21934, 2001.

- Shapiro, N.M., M. Campillo, A. Paul, S.K. Singh, D. Jongmans, and F.J. Sanchez-Sesma, Surface-wave propagation across the Mexican Volcanic Belt and the origin of the long-period seismic-wave amplification in the Valley of Mexico, *Geophys. J. Int.*, *128*, 151-166, 1997.
- Sieminski, a., J.-J. Leveque, and E. Debayle, Can finite-frequency effects be accounted for in ray theory surface wave tomography?, *Geophys. Res. Lett.*, *31*, L24614, doi:10.1029/2004GL021402, 2004.
- Silver, L.T., and B.W. Chappell, The Peninsular Ranges Batholith: an insight into the evolution of the Cordilleran batholiths of southwestern North America, *Trans. Roy. Soc. Edinburgh: Earth Sci.*, *79*, 105-121, 1988.
- Silver, P.G., and W.E. Holt, The mantle flow field beneath western North America, *Science*, *295*, 1054-1057, 2002.
- Smith, M.L., and F.A. Dahlen, The azimuthal dependence of Love and Rayleigh wave propagation in a slightly anisotropic medium, *J. Geophys. Res.*, *78*, 3321-3333, 1973.
- Stixrude, L., and C. Lithgow-Bertelloni, Mineralogy and elasticity of the oceanic upper mantle: Origin of the low-velocity zone, *J. Geophys. Res.*, *110*, B03204, doi:10.1029/2004JB002965, 2005.
- Tanimoto T., and K. P. Sheldrake, Three-dimensional S-wave velocity structure in southern California, *J. Geophys. Res.*, *29*(8), 10.1029/2001GL013486, 2002.
- Tarantola, A., and B. Valette, Generalized non-linear problems solved using the least-squares criterion, *Rev. Geophys. Sp. Phys.*, *20*, 219-232, 1982.

- Van der Lee, S., High-resolution estimates of lithospheric thickness from Missouri to Massachusetts, USA, *Earth Planet. Sci. Lett.*, 203, 15-23, 2002.
- Van Kooten, G.K., Mineralogy, petrology, and geochemistry of an ultra-potassic basaltic suite, central Sierra Nevada, California, USA, *J. Petrol.*, 21, 651-684, 1980.
- Walck, M.C. and J.B. Minster, Relative array analysis of upper mantle lateral velocity variations in southern California, *J. Geophys. Res.*, 87, 1754-1772, 1982.
- Wang, J and T. Teng, Surface wave profiling of the lithosphere beneath the Mojave desert using TERRAscope data, *J. Geophys. Res.*, 99, 743-750, 1994.
- Wang, K., T. Plank, J. D. Walker, and E. I. Smith, A mantle melting profile across the Basin and Range, SW USA, *J. Geophys. Res.*, 107(B1), 10.1029/2001JB000209, 2002.
- Weeraratne, D.S., D.W. Forsyth, K.M. Fischer and A. A. Nyblade, Evidence for an upper mantle plume beneath the Tanzanian craton from Rayleigh wave tomography, *J. Geophys. Res.*, 108(B9), doi:10.1029/2002JB002273, 2003.
- Wernicke, B., et al., Origin of high mountains in the continents: The southern Sierra Nevada, *Science*, 271, 190-193, 1996.
- Wielandt, E., Propagation and structural interpretation of non-plane waves, *Geophys. J. Int.*, 113, 45-53, 1993.
- Yang Y. and D.W Forsyth, Regional tomographic inversion of the amplitude and phase of Rayleigh waves with 2-D sensitivity kernels, submitted to *Geophys. J. Int.*. 2005.
- Zandt, G., The southern Sierra Nevada drip and the mantle wind direction beneath the southwestern United States, *Int. Geology Rev.*, 45, 213-224, 2003.

- Zandt, G., and C.R. Carrigan, Small-scale convective instability and upper mantle viscosity under California, *Science*, 261, 460-463, 1993.
- Zandt, G., H. Gilbert, T. J. Owens, M. Ducea, J. Saleeby and C. H. Jones, Active foundering of a continental arc root beneath the southern Sierra Nevada in California, *Nature*, 431, 41-46, 2004.
- Zhao D., H. Kanamori, and E. Humphreys, Simultaneous inversion of local and teleseismic data for the crust and mantle structure of southern California, *Phys. Earth Planet. Inter.*, 93, 191-214, 1996.
- Zhao, D. and H. Kanamori, P-wave image of the crust and uppermost mantle in southern California, *Geophys. Res. Lett.*, 19, 2329-2332, 1992.
- Zhou Y., Dahlen, F.A. & Nolet, G., 2004. 3-D sensitivity kernels for surface-wave observables, *Geophys. J. Int.*, 158, 142-168.
- Zhu, L. and H. Kanamori, Moho Depth variation in southern California from teleseismic receiver functions, *J. Geophys. Res.*, 105, 2969-2980, 2000.

Figure Captions

Figure 1. Topography of southern California. The locations of major tectonic provinces and faults (continuous lines) are labeled. Triangles represent broadband three-component seismic stations used in this study.

Figure 2. Azimuthal equidistant projection of earthquakes used in this study. The plot is centered on the center of the selected stations. The straight lines connecting each event to the array center represent the great-circle ray paths. Note the good azimuthal

coverage of the events.

Figure 3. Great-circle ray paths in southern California at periods of 50 s. White triangles represent stations. Note the dense crossing paths in the array area.

Figure 4. The variation of station site responses with periods for four stations. Each line represents one station. One standard uncertainties are shown with error bars. The instrumental response has been removed before the inversion. Typical variation pattern of station site responses is shown as bold lines, large deviating from one at short periods and gradually approaching one at long periods. The station responses for the two thin lines show reverse pattern, which are probably caused by wrong instrumental response correction.

Figure 5. Map views of station site responses of Rayleigh waves at periods of 25 s. The variation in amplitude is up to a factor of two, with the lowest amplitudes near the coast and in southernmost California and the highest amplitudes in the Owens Valley/Long Valley region.

Figure 6. 2-D sensitivity kernels for a 20 mHz plane Rayleigh wave. (Top panels) map views of kernels at surface. Black triangles denote receivers; white arrows indicate the incoming direction of the plane Rayleigh wave. (Bottom panels) Cross-section profiles of kernels along the bold lines marked in top panels.

Figure 7. Grid nodes used in Rayleigh-wave phase velocity inversions. Grid spacing is described in the text. Note the gridded area is larger than the station-covered area.

Figure 8. Average phase velocities in southern California at 11 periods from 25 to 143

s. Error bars represent two standard deviations.

Figure 9. Maps of Rayleigh wave phase velocities and phase velocity uncertainties.

The phase velocity maps are shown at seven periods: (a) 25 s, (b) 33 s, (c) 50 s, (d) 67 s, (e) 83 s, (f) 100 s, and (g) 125 s. Velocity anomalies are calculated relative to the average phase velocities of southern California shown in Figure 8. (h) shows twice standard errors of phase velocities at 50 s. The phase velocity maps are masked using 1% error contour at period of 50 s.

Figure 10. One-dimensional shear wave velocity profiles. The model of TNA is plotted as a dashed line. The solid line represents our reference model in southern California obtained using the TNA model as starting model.

Figure 11. Resolution kernels of shear velocity inversion for the reference model at depths of 40 km (circles and dotted line), 80 km (stars and solid line) and 140 km (diamonds and dashed line).

Figure 12. Maps of shear-wave velocity anomalies in the nine layers from surface to depth of 170 km. The velocity anomalies are relative to the 1-D reference model shown in Figure 10 (solid line). The white bold lines in 12d are locations of vertical cross-sections shown in Figure 14. In 12e, Abbreviations for major shear-wave velocity anomalies are labeled as the southern Sierra Nevada and Walker Lane anomaly (SNWLA), the Great Valley anomaly (GVA), the eastern Transverse Range anomaly (ETRA), the western Transverse Range anomaly (WTRA), and the Salton Trough anomaly (STA).

Figure 13. Map of the crustal thickness. The starting crustal model for the inversion is from *Zhu and Kanomori* [1992].

Figure 14. Vertical cross-sections of shear wave velocity structures. The locations of the three profiles are delineated in Figure 13d. Abbreviations for major tectonic units are labeled on the top of cross-sections as the Great Valley (GV), the Sierra Nevada (SN), the Owen Valley (OV), the eastern Transverse Range (ETR), the western Transverse Range (WTR), and the Peninsular Range (PR).

Figure 15. Distribution of Volcanism (black dots) in southern Sierra Nevada during Quaternary (1.5-0 Ma) period. Bold line outlines area with which Pliocene (chiefly 4-3 Ma) volcanism was prevalent; note that Quaternary volcanic fields (LV-Long Valley, BP-Big Pine, GT-Golden Trout, C-Coso) are all within area of Pliocene event. Dashed line outlines the area of Pliocene potassic volcanism. Colors show shear-wave velocity anomalies at depths of 70-90 km as shown in Figure 12d. Note that the Quaternary volcanism coincides the region of lowest velocities.

Figure 16. Variations of uniform azimuthal anisotropy with period in southern California. The vertical solid bars with caps represent one standard deviation of strength. Fast directions of azimuthal anisotropy are indicated by the orientations of black bars as if in a map view with north up on the diagram; is shown as two shaded bars at each period. Note that one standard deviations for the fast directions are very small at short periods.

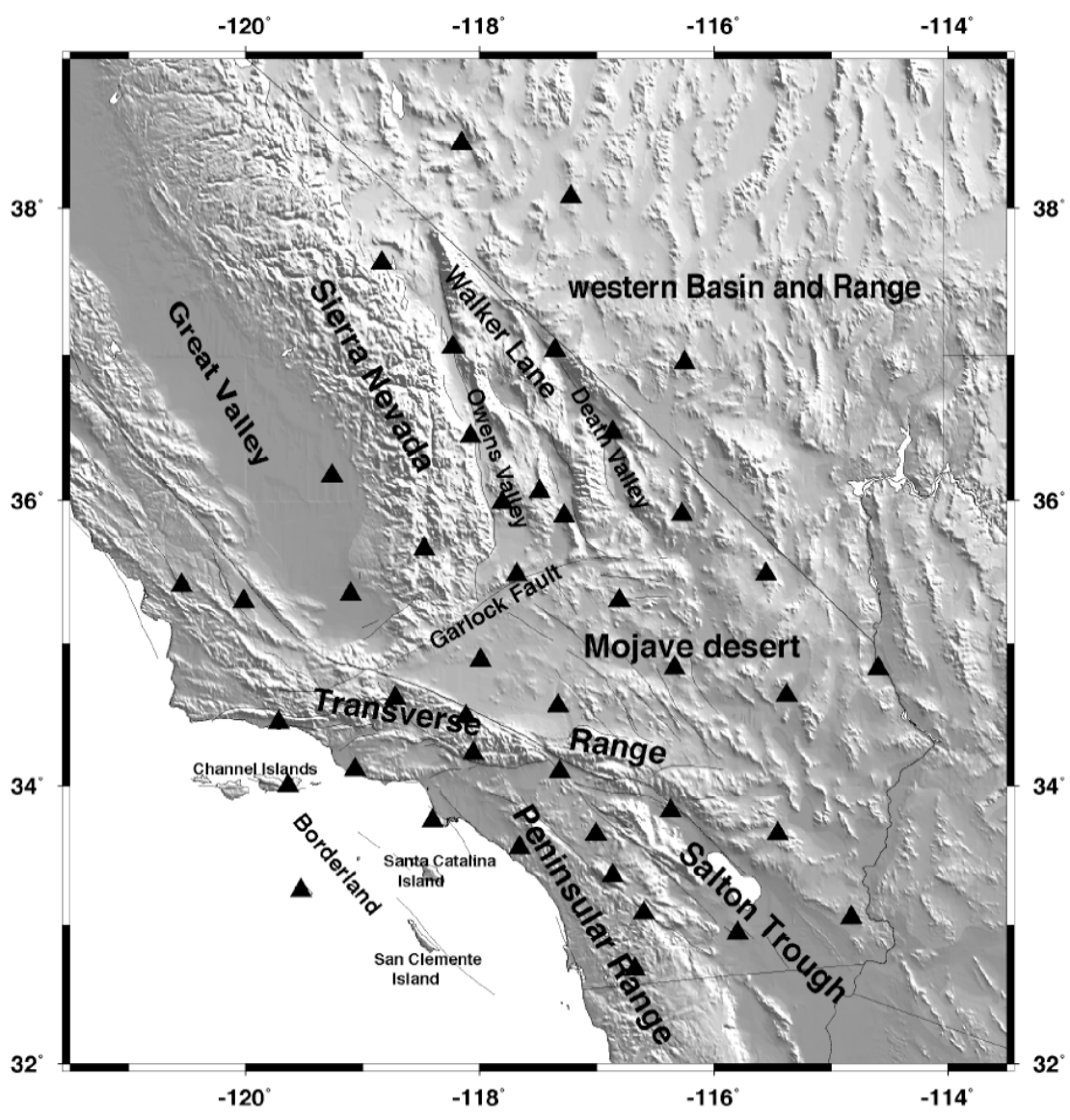


Figure 1

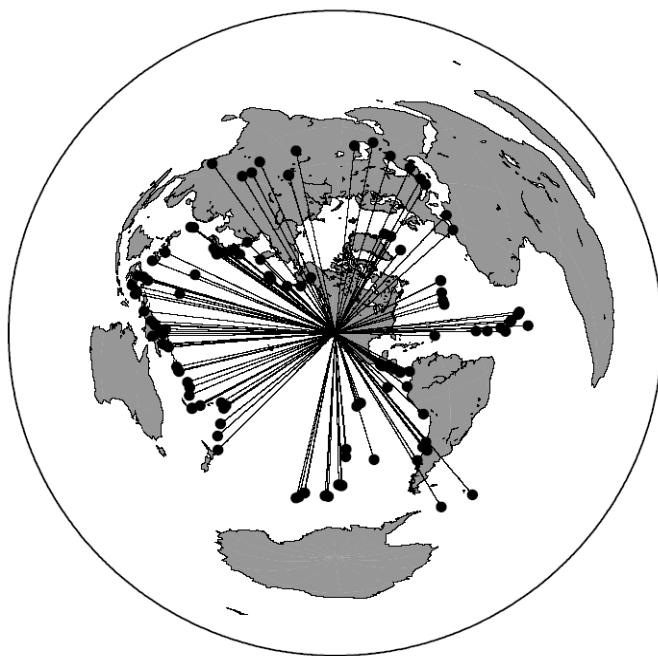


Figure 2

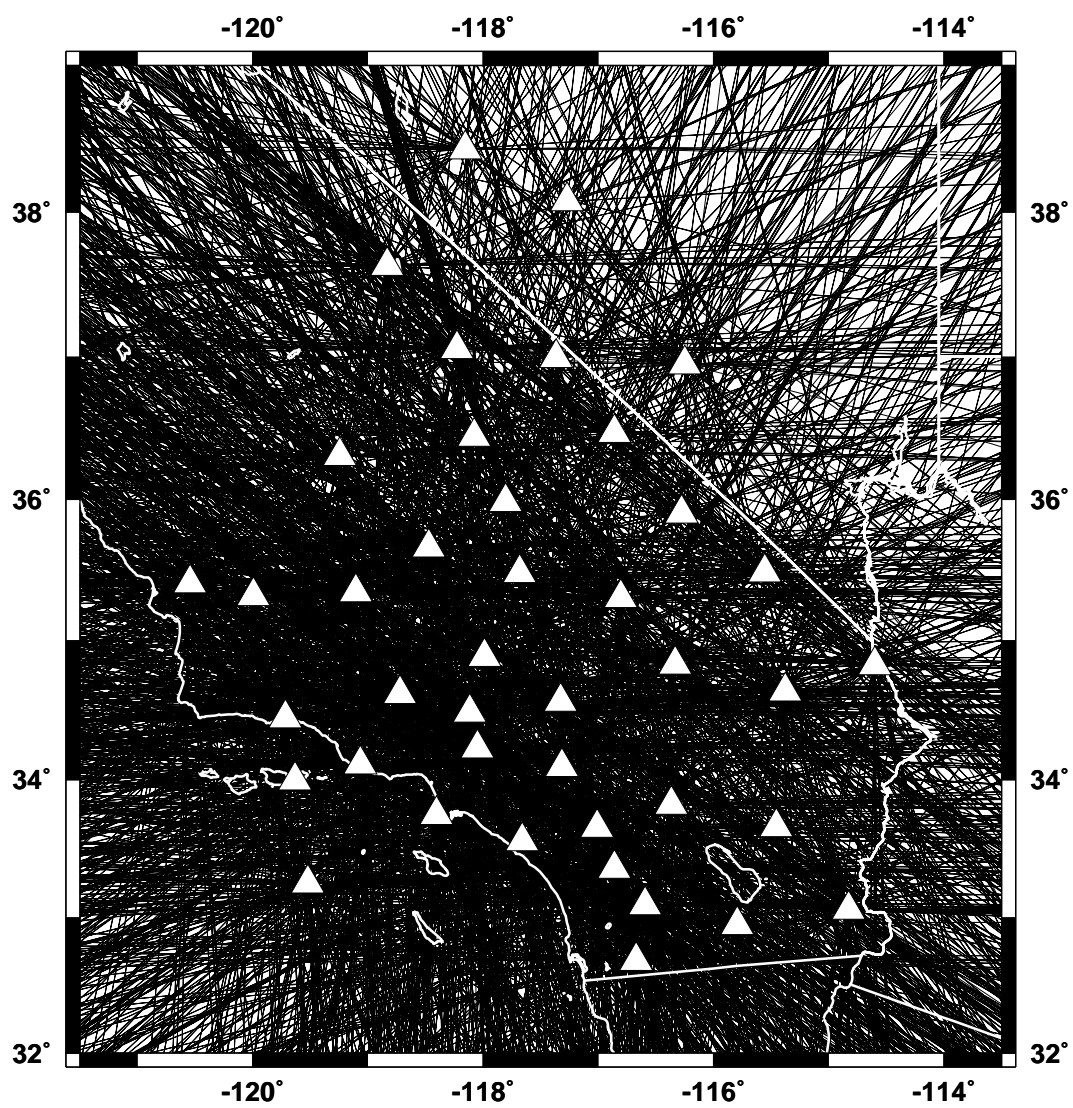


Figure 3

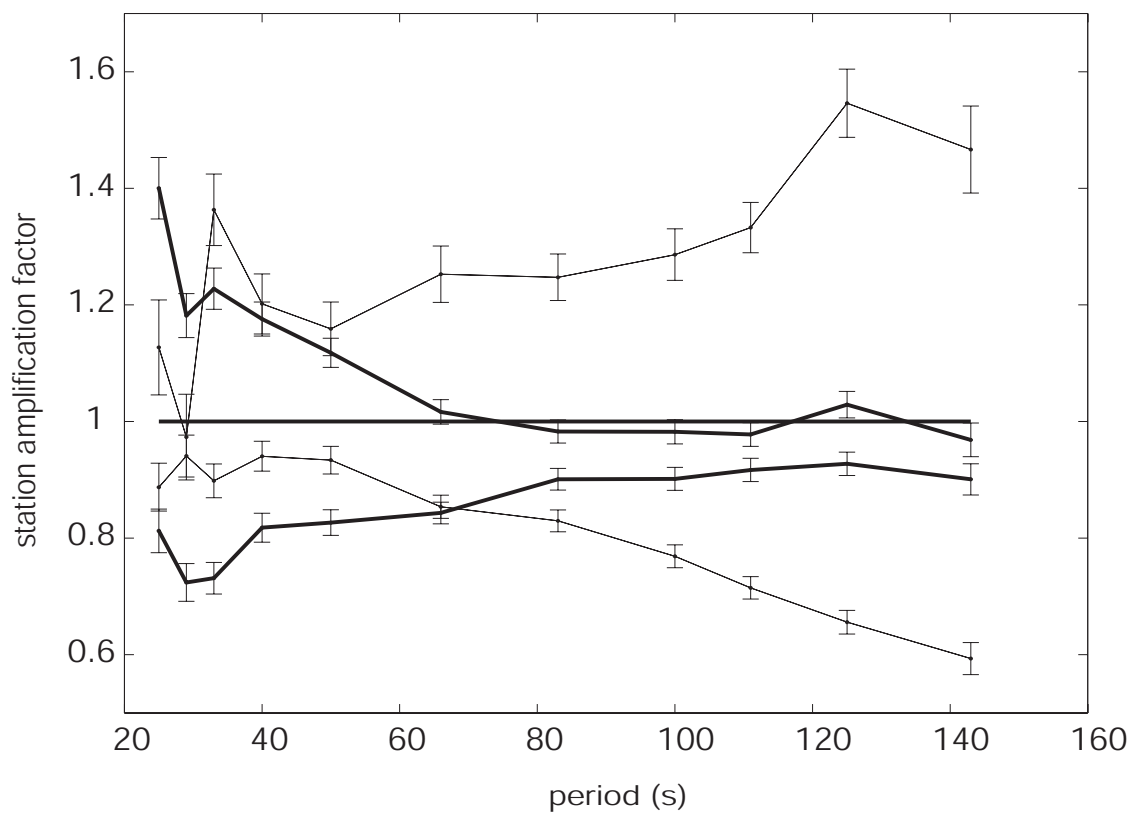


Figure 4

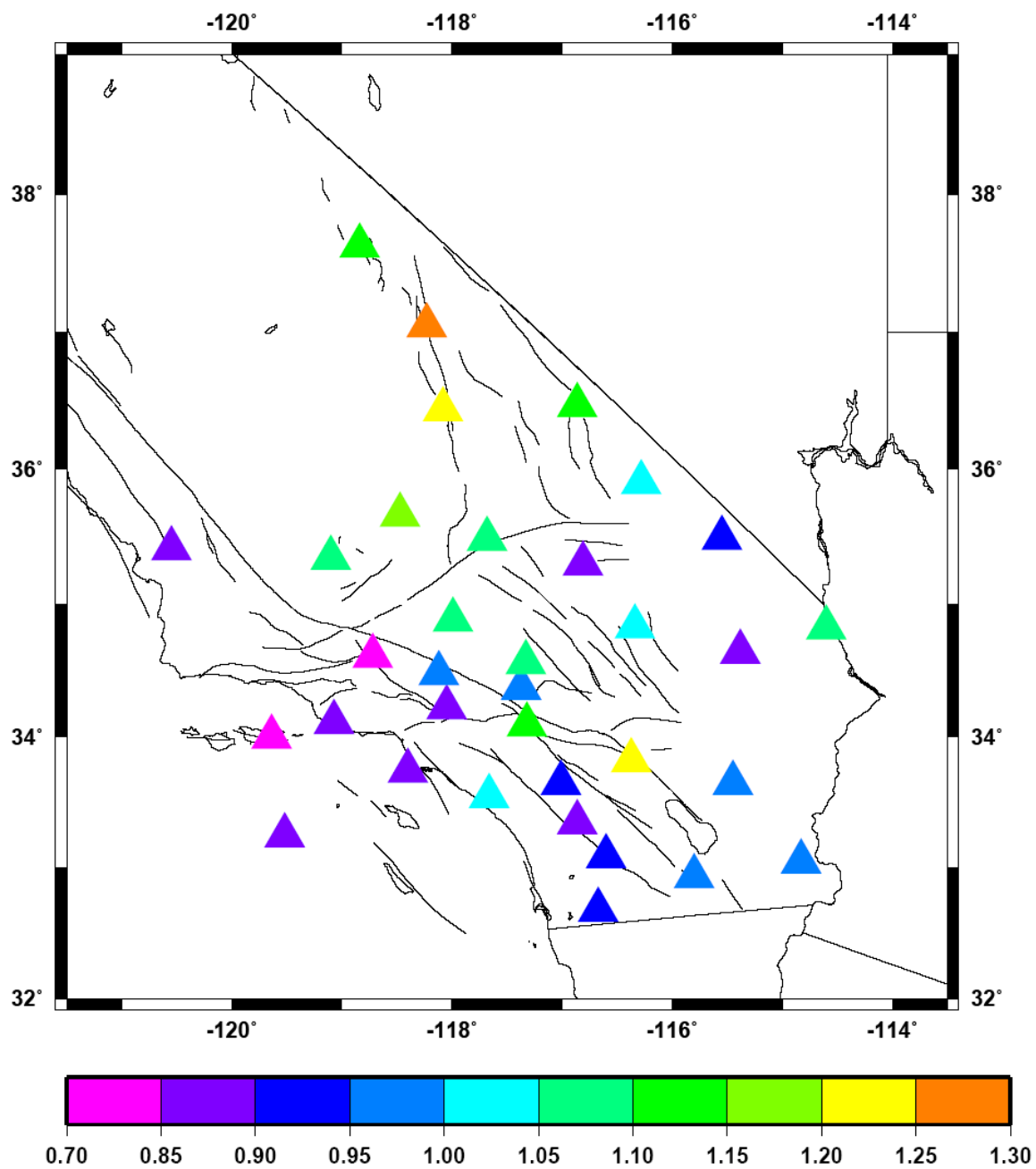


Figure 5

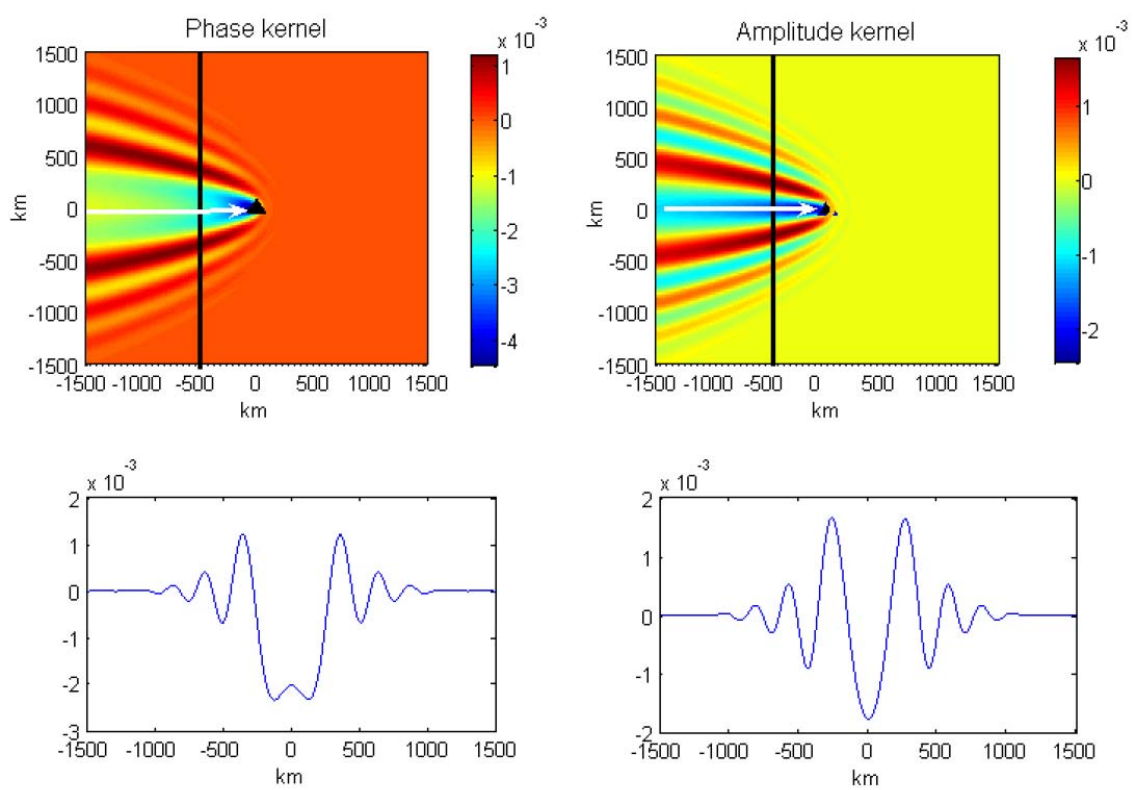


Figure 6

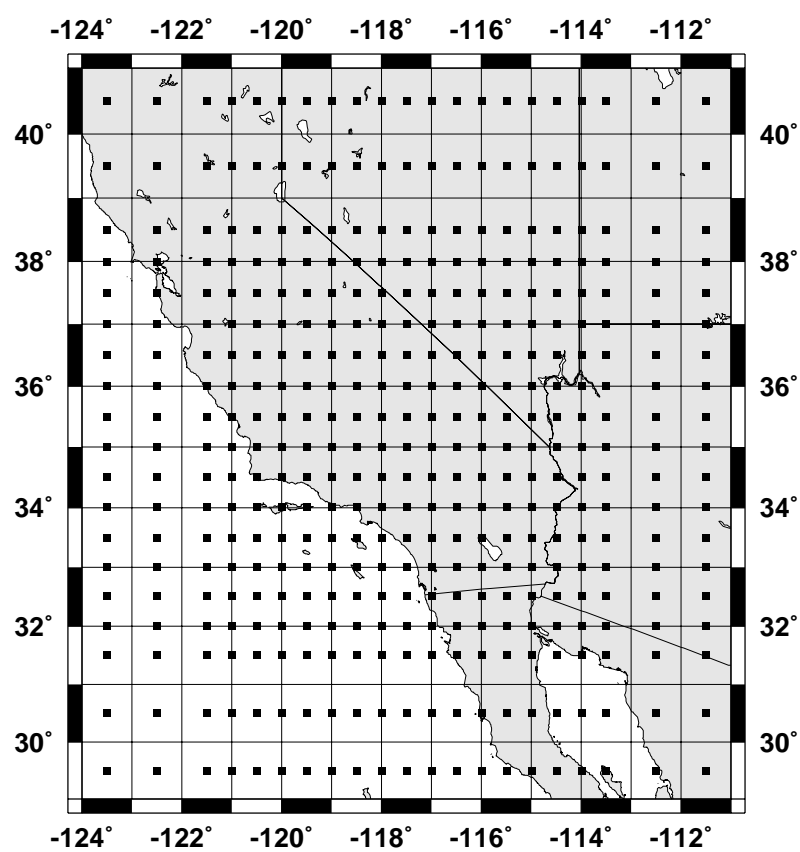


Figure 7

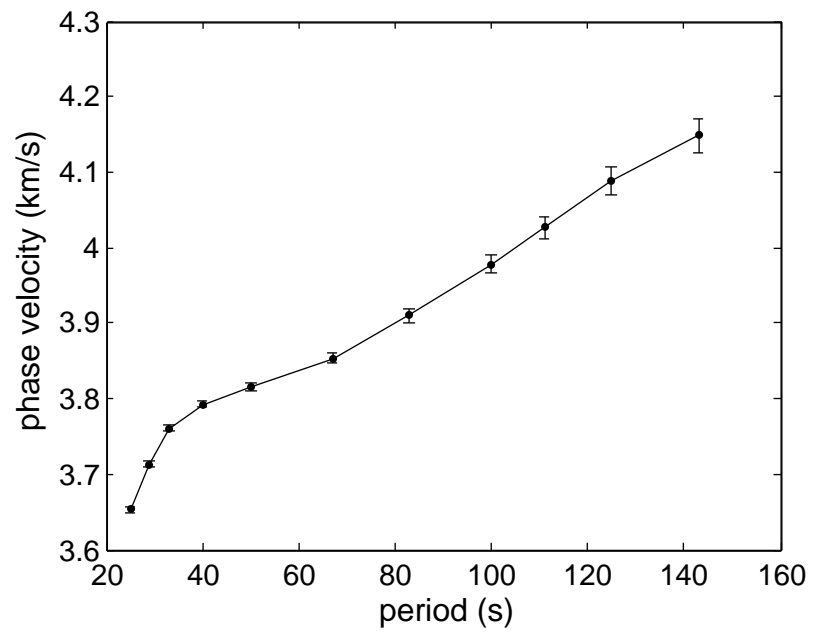


Figure 8

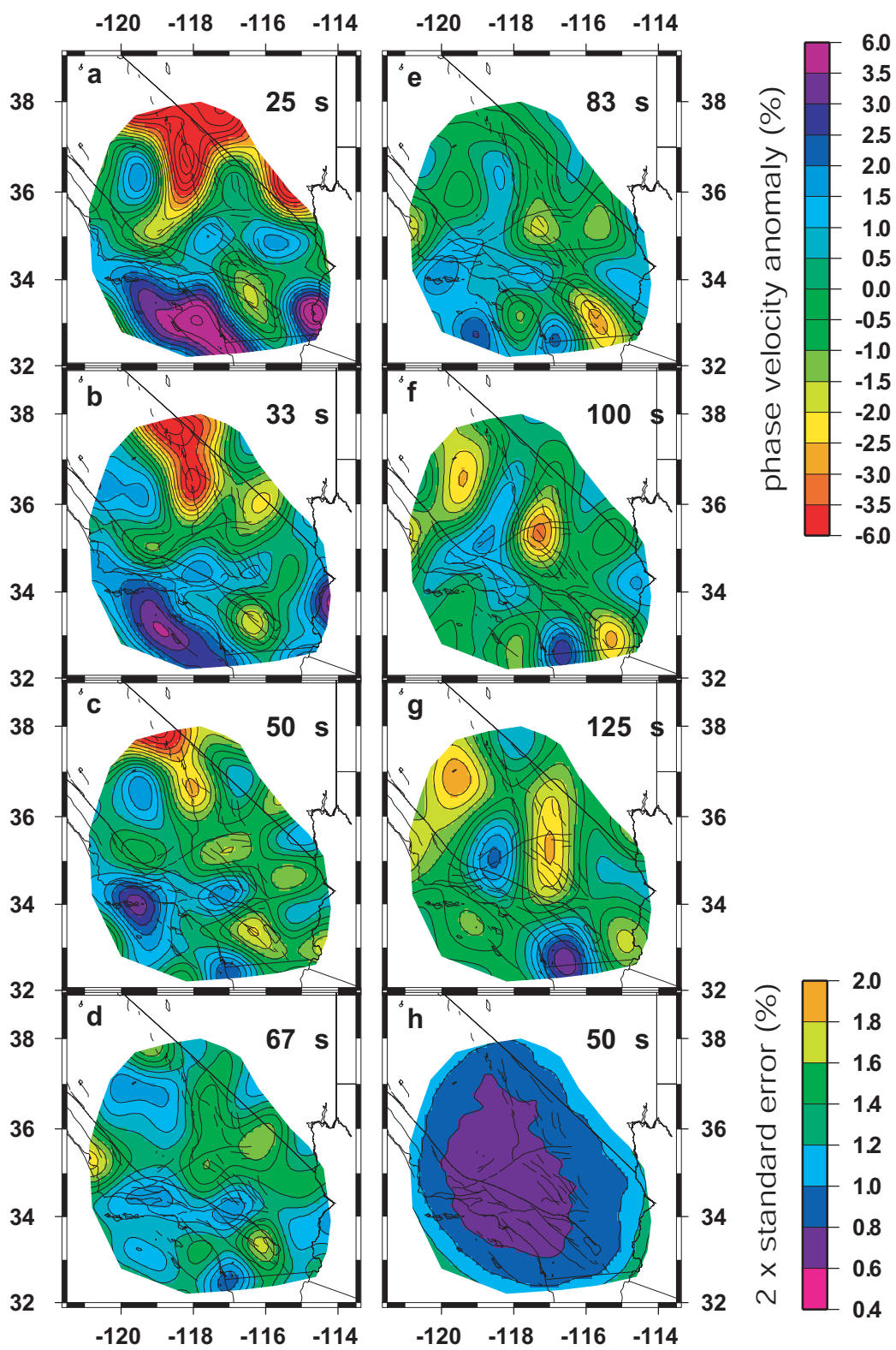


Figure 9

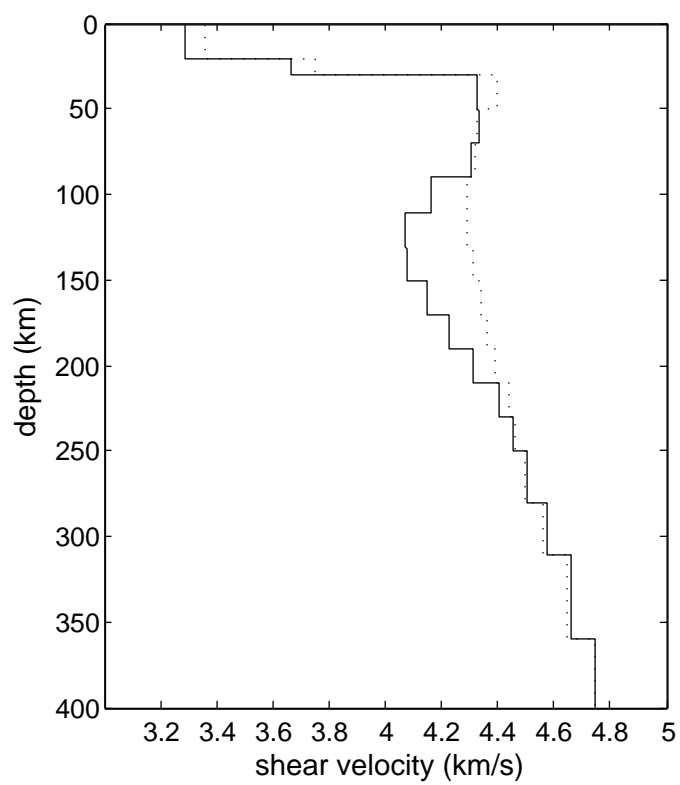


Figure 10

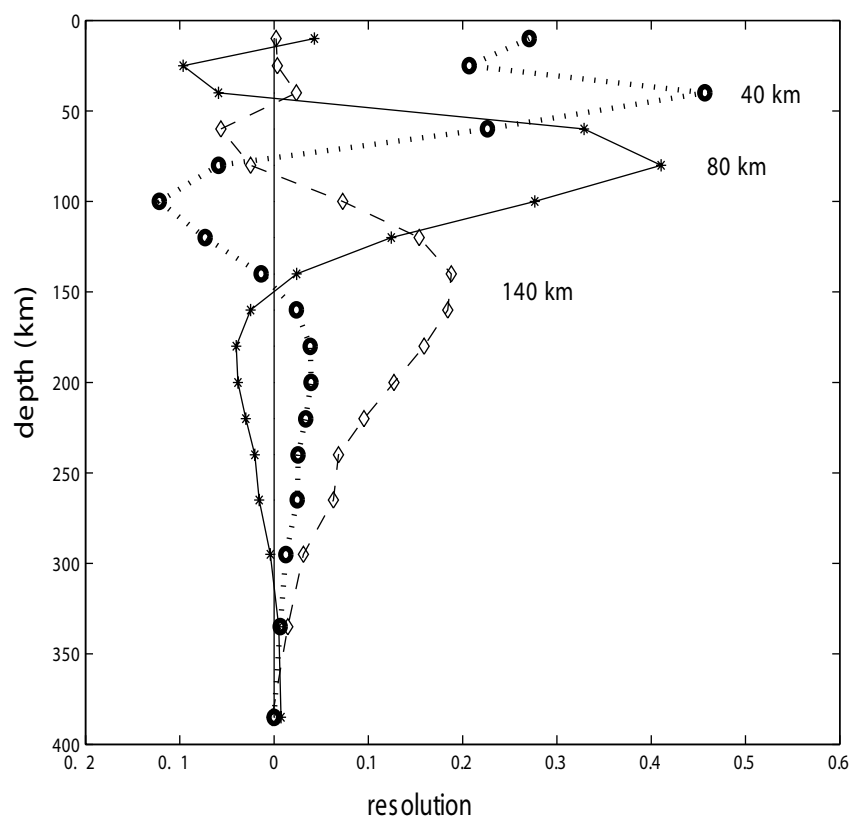


Figure 11

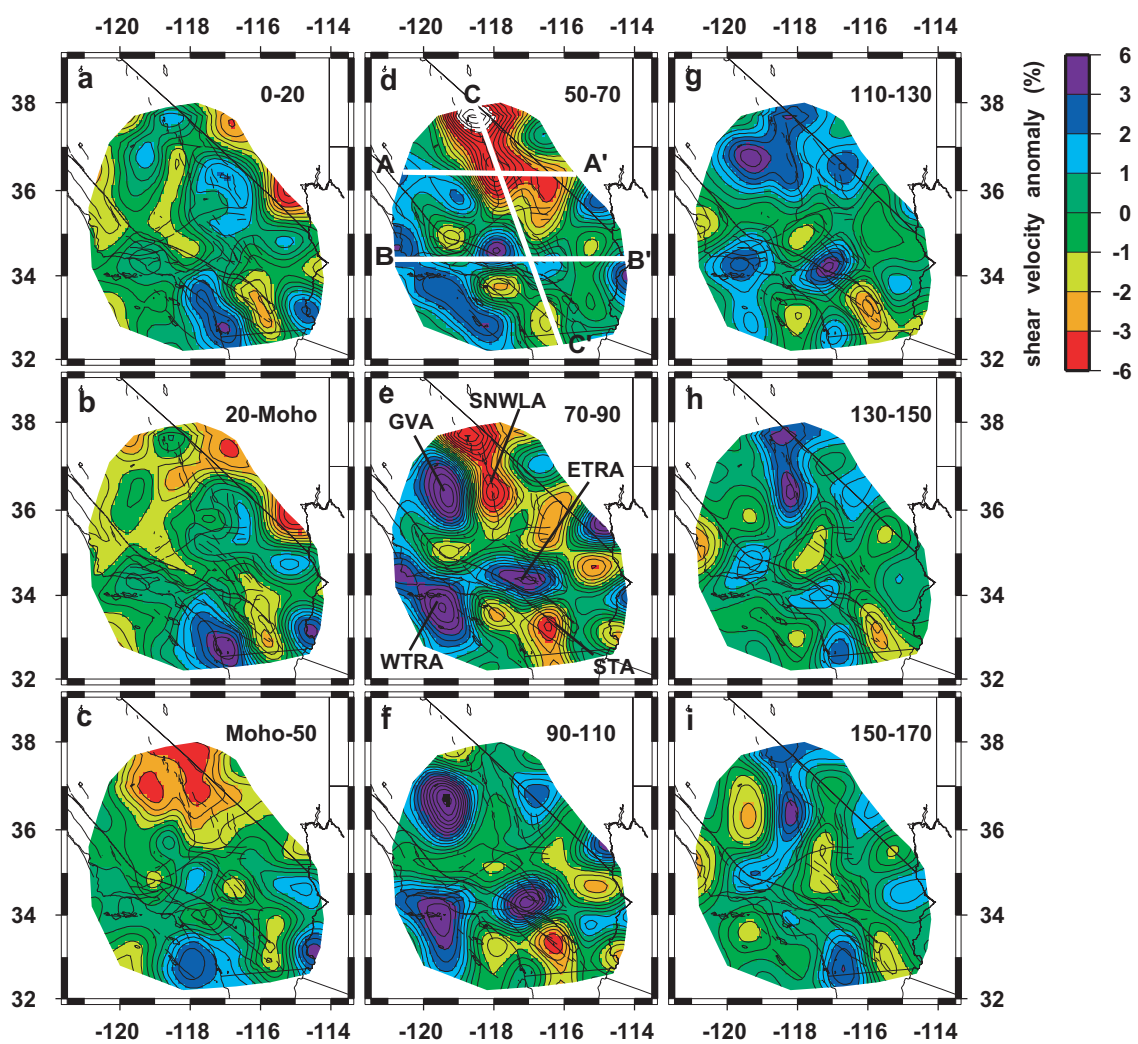


Figure 12

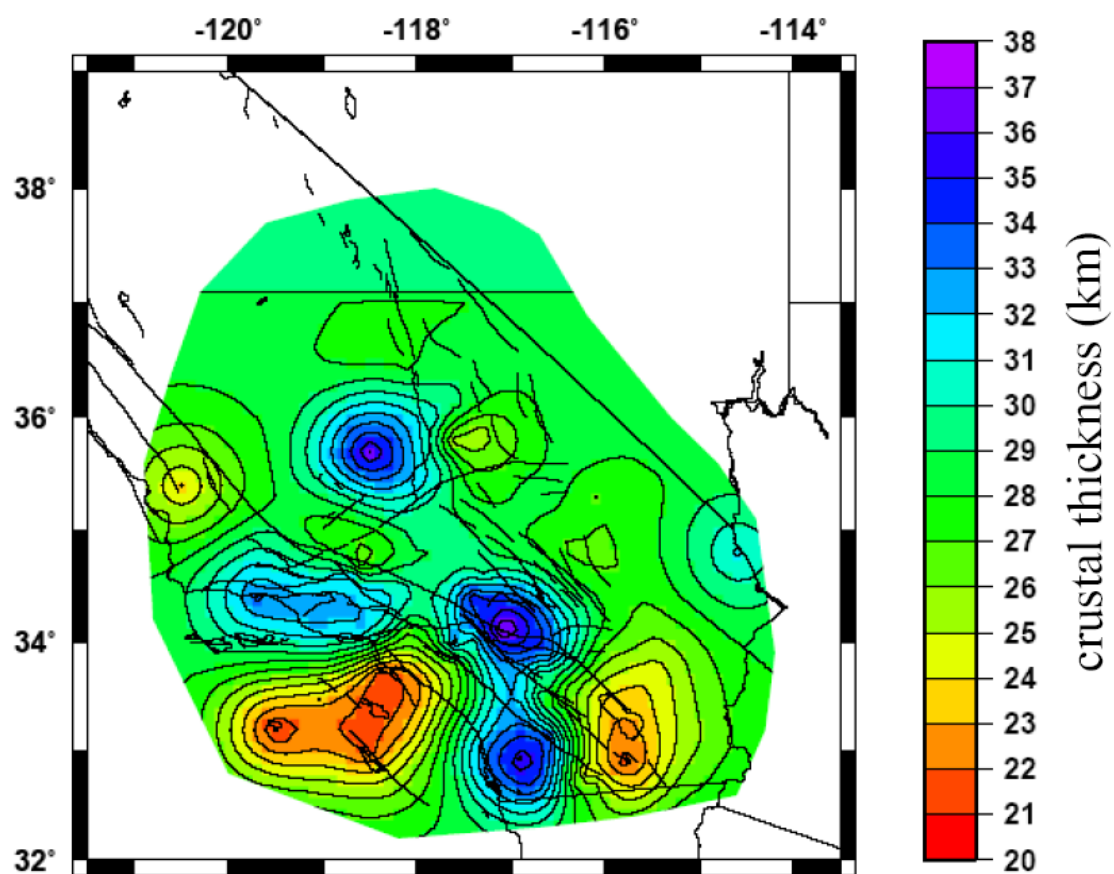


Figure 13

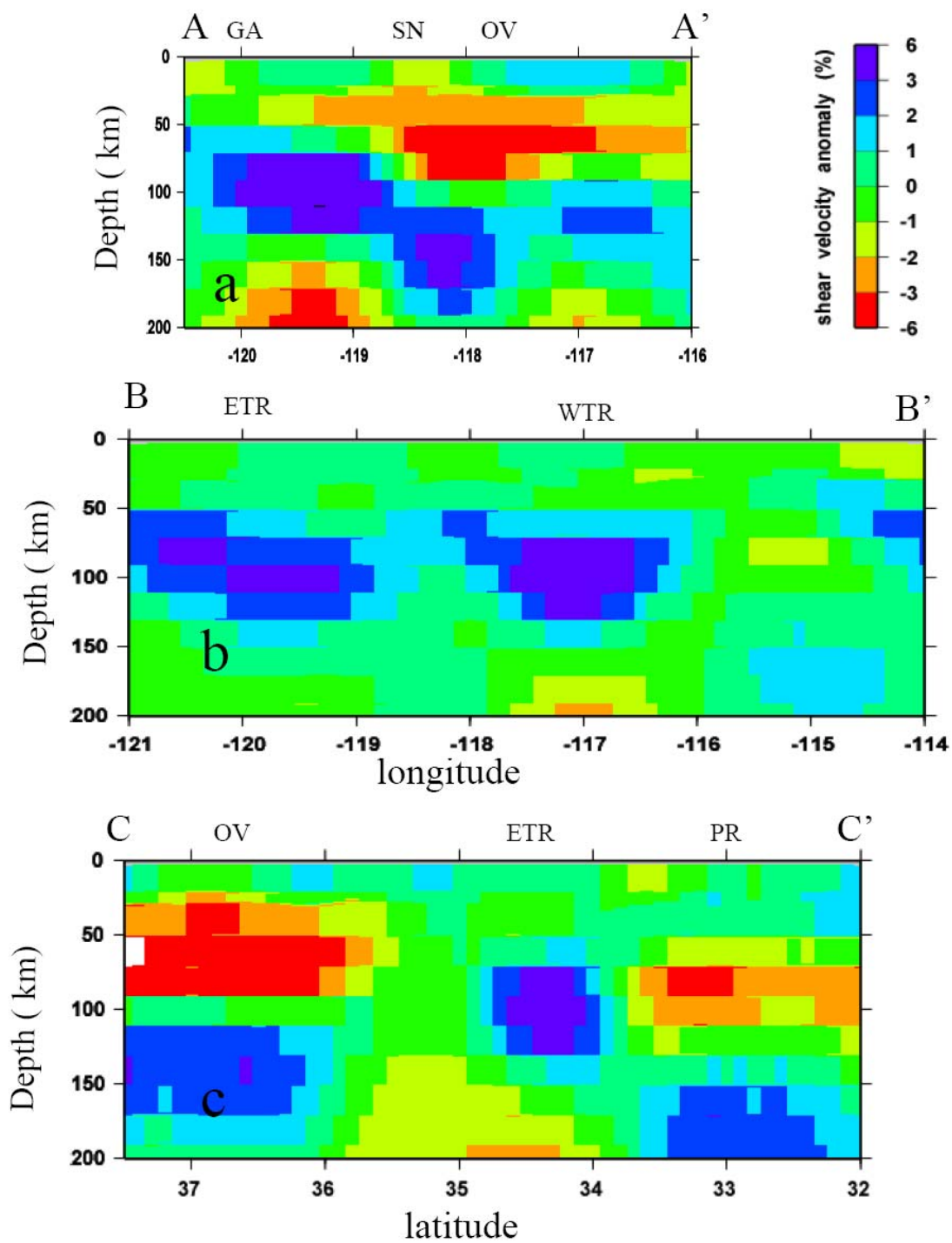


Figure 14

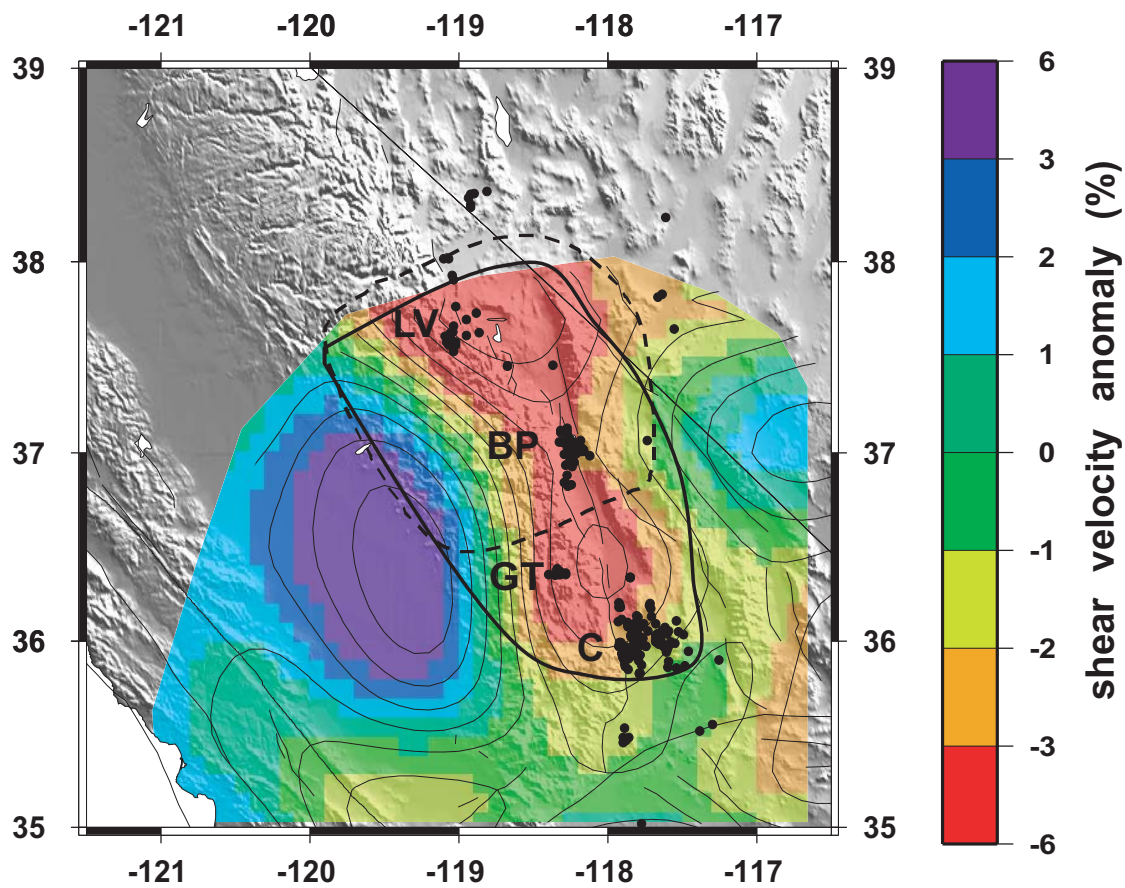


Figure 15

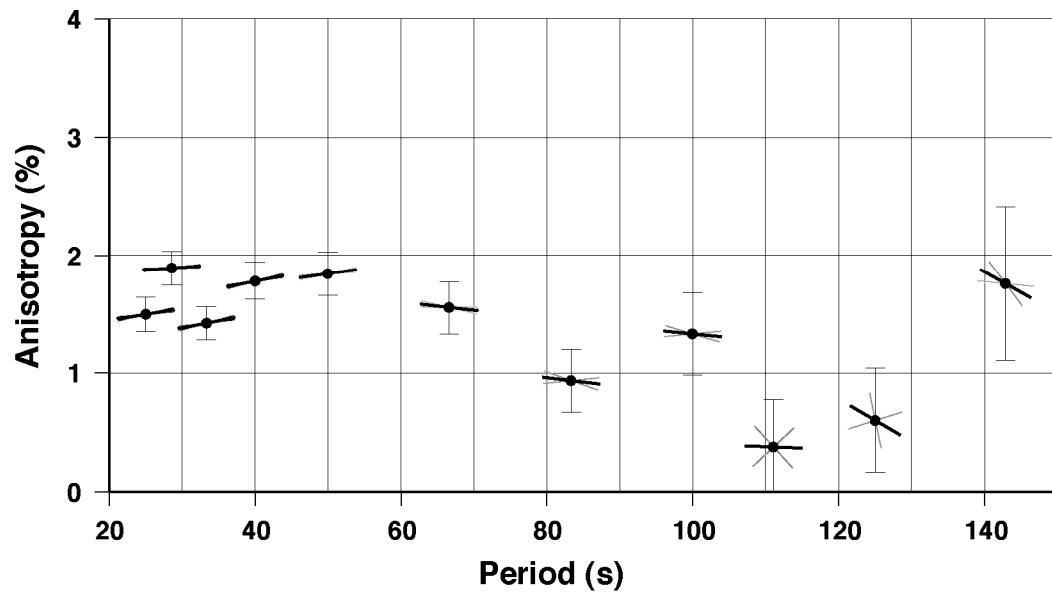


Figure 16

Chapter 3

Seismic attenuation and velocity constraints on the formation of oceanic
lithosphere and the origin of the low-velocity zone

Yingjie Yang and Donald W. Forsyth

Department of Geological Sciences

Brown University

Providence, Rhode Island 02912

Dayanthie S. Weeraratne

Department of Terrestrial Magnetism

Carnegie Institution of Washington

Washington, DC 20015-1305

Abstract

Seismic attenuation has long been neglected in traditional seismic tomography since attenuation effects on amplitude are too hard to separate from other effects such as multi-pathing, focusing/defocusing and scattering. However, attenuation is an important property of Earth's materials and can provide us additional knowledge other than elastic velocities about temperature, fluid content, phase changes, and density of solid-state defects in the crust and mantle. Fundamental mode surface wave studies at different periods allow us to constrain regional and vertical variation of the quality factor Q . We use 2-D sensitivity kernels for surface waves based on single-scattering (Born) approximation to account for the effects of scattering on amplitude in regional surface wave studies.

We invert phase and amplitude data of Rayleigh waves for shear wave velocities and attenuation (Q_{μ}^{-1}) in very young (less than 10 Ma) Pacific regions using teleseismic sources recorded by ocean-bottom seismometers (OBSs). There is a high seismic velocity lid underlain by a low velocity zone. Q_{μ} shows a similar variation pattern: large Q_{μ} at depths shallower than 50 km and much smaller Q_{μ} at depths greater than 60 km. Models that attribute the origin of the low velocity zone beneath old seafloor solely to temperature and pressure effects predict Q_{μ} values an order of magnitude too low beneath young seafloor. An alternative model considering the variation of water content in the upper mantle can explain partially the variation pattern of velocities and attenuation. Partial melting in the shallow upper mantle at mid-oceanic ridges during the production

of the oceanic crust effectively removes the water in the MORB source region and leads to a “dry” depleted peridotite layer underlain by a “wet” fertile peridotite. The presence of water in the asthenosphere lowers Q_{μ} and seismic velocity beneath old seafloor, so that the effects attributed to thermal variations are much smaller and thus attenuation in the hot, young lithosphere is less pronounced. In addition to seismic reduction owing to attenuation, ~1% partial melting is required to explain the minimum value of shear wave velocities in the low velocity zone beneath young seafloor. The ~1% melt is produced in the depth range between the “wet” solidus and the “dry” solidus due to the presence of relatively small amount of water. Our seismic observations provide strong constraints on the argument that the structure of oceanic plates is controlled by compositional as well as thermal parameters.

Introduction

One of the key questions in plate tectonics is the origin of the low velocity zone (LVZ) in the upper mantle. The LVZ was first recognized by *Gutenberg* [1959]. Since then, the LVZ has been observed in many seismological studies, particularly in tectonic and oceanic regions. The LVZ is also a region of high attenuation of seismic waves, low viscosity and high electrical conductivity [*Shankland and Waff*, 1977] and is thus commonly associated with the asthenosphere. The low viscosity asthenosphere can lubricate the motion of the cold, highly viscous or elastic overlying plates and thus may be the key factor that leads to convection in the earth taking the form of plate tectonics

[*Richards et al.*, 2001]. Because the influences controlling viscosity and attenuation of seismic waves probably also control the rheology of the mantle materials, a better understanding of origin of the LVZ can help us to understand the interaction between the lithosphere and sub-lithosphere upper mantle.

Early studies attributed the pronounced oceanic low-velocity zone to the presence of partial melt in the upper mantle [e.g. *Anderson and Sammis*, 1970], noting that laboratory measurements of the temperature dependence of elastic coefficients in mantle minerals at ultrasonic frequencies implied that the decrease in velocity expected for reasonable geotherms was not sufficient to explain the large drop in velocities in the LVZ. *Karato and Jung* [1998], however, argued that the presence of a small amount of melt has no significant effect on seismic velocity for the range of melt fraction expected over most of the upper mantle, and proposed instead that water dissolved in minerals such as olivine can significantly reduce seismic wave velocities through anelastic relaxation. More recently, *Stixrude and Lithgow-Bertelloni* [2004] and *Faul and Jackson* [2005] have attributed the origin of the LVZ primarily to the increase in temperature with depth, suggesting that neither water nor melt is required if anelastic effects at seismic frequencies are taken into account. Anelasticity causes the attenuation of seismic waves, so measurements of the decay of seismic surface waves provide a key test of these hypotheses for the origin of the LVZ.

With the great increase in the availability of high quality broadband data in the recent years, there have been numerous tomographic studies performed on both global and

regional scales. However, far fewer studies have focused on the anelasticity of the earth. Anelasticity is one of important properties of earth materials, providing us information about thermal structure and the presence of partial melting or other fluids complementary to that provided by elastic velocities. Since attenuation causes dispersion in seismic velocities, attenuation information is also required to reconcile tomography results from studies using different seismic waveforms and frequencies.

It is hard to measure the attenuation of seismic waves reliably due to the difficulty of separating intrinsic attenuation effects on amplitude from other effects such as site or station responses and scattering or focusing/defocusing caused by elastic heterogeneities. The attenuation of surface waves offers the promise of revealing the vertical distribution of the quality factor Q in the upper mantle, but measuring it on a regional basis can be extremely difficult because the wavelength of the waves may be of the same order as the dimensions of the region of interest. Consequently, relatively little energy is lost as the wave propagates across the study area. In recently years, there have been a few 3-D global attenuation studies using surface waves. For example, *Billien et al.* [2000] obtained global Rayleigh wave attenuation structures by simultaneous inversion of phases and amplitudes; *Selby and Woodhouse* [2002] gave a 3-D shear quality factor, Q_{μ} , model of the upper mantle based on amplitude measurements of Rayleigh waves; and *Gung and Romanowicz* [2004] presented a degree-8 3-D Q model based on waveform inversion of three-component surface waves. Fundamental mode surface waves have also been used on regional scales to obtain attenuation values and constrain Q_{μ} variations with depth.

One common method used to obtain regional attenuation coefficients is the two-station method, which measures the difference of amplitude between two stations lying along a great-circle path from the earthquake source [e.g., *Cong and Mitchell, 1998*]. The two-station method assumes that surface waves propagate along great-circle paths and there are no strong heterogeneities between the two stations or multipathing between source and receiver. Thus, the method requires events with special locations and the study region to be nearly homogenous, which limits its application. Because all source events share the same path between receiver pairs, there is no way of checking for focusing within the study area.

Recently, with the development of finite-frequency scattering theory for surface waves [*Zhou et al., 2004*], *Yang and Forsyth* [2005] developed a regional-scale surface wave tomography method that accounts for focusing effects within the study area. The scattering or focusing of surface waves by elastic structures are accurately described by 2-D sensitivity kernels based on the Born approximation. By using many stations and sources at a variety of azimuths, we can detect the velocity heterogeneities that cause focusing and so we can separate the scattering and focusing/defocusing effects on amplitude from attenuation.

In this study, we simultaneously invert for lateral variations in phase velocities and attenuation coefficients in very young seafloor (less than 10 Ma) using phase and amplitude data of fundamental mode Rayleigh waves. The attenuation coefficients are used to invert for Q_{μ} in the upper mantle. Shear wave Q_{μ} and velocities are used together

to constrain the formation of oceanic plate and the origin of low velocity zone (LVZ) in the oceanic plate. These observations represent the first measurement of attenuation of surface waves within a regional array of seismometers in the oceans. Because the arrays are in young seafloor where the lithosphere is thin and temperatures in the uppermost mantle are high, the observations provide a critical test of the hypothesis that properties of the low velocity zone are primarily controlled by temperature.

Methodology and data acquisition

The decay of the amplitude of surface waves due to attenuation along propagation paths can be expressed as $e^{-\gamma x}$, where γ is the attenuation coefficient and x is the propagation distance. The quality factor of Rayleigh waves, Q_R , is related to γ_R by $\gamma_R = \pi / uTQ_R$, where T is period, and u is group velocity. Attenuation effects on amplitude are so small on a regional scale that they are often obscured by other phenomena. Inverting for attenuation without considering focusing can introduce systematic bias, sometimes even resulting in negative values. *Yang and Forsyth* [2005] have shown that the 2-D sensitivity kernels derived by *Zhou et al.* [2004] can be employed to represent the focusing effects caused by elastic heterogeneities with scales on the order of a wavelength. We informally use the term focusing to refer to the amplitude variations caused by heterogeneities within the array that are large enough to be resolved by tomography. Scattering effects from heterogeneities with dimensions much smaller than a wavelength will be indistinguishable from intrinsic attenuation. Both

phase and amplitude can be predicted accurately for a plane Rayleigh wave propagating through heterogeneous structures.

In our inversion, we solve for lateral changes in phase velocity simultaneously with attenuation in order to account for focusing effects. Attenuation is assumed to be a function only of distance of propagation in the form $e^{-\gamma x}$, while we use the full 2-D, finite frequency response kernels for phase velocity and focusing. Another factor affecting amplitude is station site response owing to the difference in structure beneath each station or slight differences in seismometer response. We include an additional amplitude parameter for each station analogous to station static corrections for time delays in body wave tomography, except that this site response term is frequency dependent. To account for the scattering effects outside the study regions, a two-plane wave approximation is employed to represent the complexity of the incoming wavefield. *Forsyth and Li* [2005] have shown the two-plane wave approximation can represent the incoming wavefield relatively well for Rayleigh waves propagating to an array near the East Pacific Rise, and *Yang and Forsyth* [2005] demonstrated that this approach yielded good tomographic resolution of structure within an array for waves that had propagated through a randomly heterogeneous medium before entering the study region. The simultaneous inversion for lateral variations in phase velocity, attenuation coefficients, wavefield parameters describing the two-plane waves, and station site responses using many earthquake sources allow us to accurately detect the variation of amplitude due to attenuation within a distance of 2 – 3 wavelengths. Amplitude decay of surface waves at our periods of

interest, ~ 16 to 67 s, is small in a regional array with an extent of a few hundred kilometers. With average array dimensions of ~ 400 km for the experiments described below, the decrease in amplitude across the array ranges from about 4% to 15%. This diminution is not resolvable using a single event or station pair. With many events incident from various directions recorded at multiple stations, we can resolve the average attenuation coefficient very well.

We study a region of very young seafloor in the southeastern Pacific (Figure 1) in which two ocean-bottom seismometer experiments (OBS) have been conducted. Attenuation is expected to be high due to high temperature in the young oceanic upper mantle and to decrease with distance from the ridge axis due to the cooling of the oceanic lithosphere. For a period of six months in 1995-1996, the Mantle Electromagnetic and Tomography (MELT) seismic team deployed two linear arrays of OBSs (marked with white triangles in Figure 1) across the southern East Pacific Rise to investigate magma generation beneath mid-oceanic ridges. Rayleigh wave data recorded at as many as 39 stations from 23 earthquakes distributed around the margins of the Pacific have been used to invert for lateral variations in phase velocities (Figure 2) [Forsyth, *et al.*, 1998]. The total number of ray paths employed is 703, but the number of records with good signal-to-noise ratio decreases with increasing period. In a region centered about 400 km west of the East Pacific Rise, the GLIMPSE experiment deployed an array of portable ocean-bottom seismometers for a year located on 4-9 Ma old seafloor including two intraplate volcanic ridge systems, the Sojourn and the Hotu Matua volcanic complexes, to

study the origin of gravity lineations and intraplate volcanic ridges on the Pacific plate. 155 events with good signal-to-noise ratios located around the margin of the Pacific plate were recorded at up to 11 stations and used to invert for phase velocities and azimuthal anisotropy (Figure 2) [Weeraratne *et al.*, 2005]. The total number of seismograms we employ from GLIMPSE ranges from a maximum of 1400 at 25 s to 230 at 67 s.

In processing the seismograms, instrument responses are normalized according to provided response parameters. In the MELT experiment, several different types of OBS were deployed. We derived empirical correction factors for each group instrument responses by comparing waveforms at closely spaced stations and by including phase and amplitude correction factors in the inversion. Only vertical components of Rayleigh waves (or in some cases, pressure variations recorded on differential pressure gauges) are used for inversion, since the vertical components have higher signal-to-noise ratio and are not contaminated by Love wave interference. The selected vertical-component seismograms are filtered with a series of narrow-bandpass (10mHz), zero-phase-shift, Butterworth filters centered at frequencies of interest. All of the filtered vertical-component seismograms are checked individually and only those with signal-to-noise ratio larger than 3 are selected. Fundamental mode Rayleigh waves are isolated from other seismic phases by cutting the seismograms using a boxcar window with a 50-s half cosine taper added to each end. The width of the boxcar window is different for each period. The filtered and windowed seismograms are converted to the frequency domain by Fourier transform to obtain phase and amplitude data. Amplitude is

corrected for geometric spreading before inversion. Details of the processing and inversion procedure are given in *Forsyth and Li* [2005], *Yang and Forsyth* [2005a,b], and *Weeraratne et al.* [2005].

Attenuation coefficients and phase velocities

Although the two OBS arrays are adjacent, they share no common stations or sources, so we have performed separate inversions for the two arrays. Interpretation of the lateral variations in phase velocities within the arrays is the topic of other papers, but we show examples of the 2-D pattern of phase velocities for one period in Figure 3. At this short period, phase velocities within the MELT array are lowest along the East Pacific Rise spreading center and increase asymmetrically with distance from the axis [*Forsyth et al.*, 1998]. In the off-axis GLIMPSE array, there are pronounced low-velocity anomalies associated with intraplate volcanic ridges and seamounts that are forming to the west of the East Pacific Rise [*Weeraratne et al.*, 2005]. The lateral variations of phase velocities in the vicinity of the arrays are large, more than 10%, which can cause substantial scattering for the incoming Rayleigh waves. Thus, simultaneous inversion for phase velocities along with attenuation is essential.

To demonstrate that attenuation is resolvable and required by the data, we first perform an inversion with no attenuation factor. The inversion includes the wave parameters that describe interference and amplitude variations due to the complexity of the incoming wave fronts, station site corrections, and phase velocity variations that are

adjusted to try to match both the observed phases and the observed amplitudes through the effects of focusing. Although a minor effect, the amplitudes are also corrected for the effects of geometrical spreading on a sphere. The observed amplitudes for each event are normalized by the rms value of all observed amplitudes for that event to keep all the amplitudes at the same scale independent of magnitude. We then examine the average residual amplitudes as a function of distance across the array. In Figure 4, we bin the residuals in 50 km distance intervals measured from the nearest station to each source event for the GLIMPSE array at 16 s period. There is a clear, systematic decrease in residual amplitude with increasing distance from the source, indicating that attenuation is required by the data. The true decay with distance is somewhat underestimated in this experiment since all the other variables in the inversion have been adjusted as much as possible to match the amplitudes, and, thus, to mimic attenuation as much as possible with a combination of other effects.

Figure 5 displays the average attenuation coefficients for the two arrays. Attenuation coefficients at all periods are less than 5×10^{-4} . Attenuation coefficients decrease with increasing period, which is expected due to the approximate inverse proportionality to period if Q_R is constant and the greater depth of sensitivity for longer wavelengths. At periods shorter than 40 s, attenuation is larger in the MELT region than in the GLIMPSE region. At periods longer than 40 s, attenuation is similar in both regions, but poorly resolved in MELT.

Attenuation of Rayleigh waves is the integrated effect of intrinsic shear wave

quality factor (Q_{μ}) over a range of depths. The bulk attenuation coefficient is normally considered to be negligible. The attenuation coefficient of Rayleigh waves at individual periods can be represented as a sum of shear wave dissipation (Q_{ul}^{-1}) in each layer from the surface to great depth as given by,

$$\gamma_R = \frac{\pi}{C_R^2 T} \sum_{l=1}^N \left[\left(\beta_l \frac{\partial C_R}{\partial \beta_l} \right)_{\omega \rho \beta} + \frac{1}{2} \left(\alpha_l \frac{\partial C_R}{\partial \alpha_l} \right)_{\omega \rho \beta} \right] Q_{\mu l}^{-1} \quad (1)$$

where ρ , ω and l are density, angular frequency, and layer number respectively [Mitchell,1995]; and the partial derivatives of phase velocity, C_R , with respect to shear velocity, β , or compressional velocity, α , include both the effects of intrinsic sensitivity and layer thickness.

We invert attenuation coefficients at various periods for the shear wave quality factor Q_{μ} in each layer. The model parameters of Q_{μ}^{-1} are slightly damped by assigning prior standard deviations of 0.06 in the diagonal terms of model covariance matrix, i.e., a priori standard deviations roughly comparable in size to the value of the starting model, and smoothed by adding off-diagonal terms to the model covariance matrix that enforce 0.3 correlation in changes of Q_{μ}^{-1} in the adjacent layers. Shear wave velocities (β_l) and compressional wave velocities (α_l) can be inverted from the average phase velocities, and the phase velocity partial derivatives in each layer are computed using the algorithm of *Saito* [1988].

1-D shear wave velocity models for the average vertical structure in both arrays are plotted in Figure 6. Compressional velocities are fixed in the crust based on seismic

refraction measurements and are assumed to be proportional to shear wave velocity in the mantle, an assumption that has little effect on the inferred Q or shear structure. A low velocity zone is observed underlying a high-velocity lid with negative gradient. If we take the depth of the maximum velocity gradient as the base of the lid, it is 20-25 km for MELT and ~ 40 km for GLIMPSE. The minimum shear wave velocity reaches ~ 4.0 km/s at ~ 70 -80 km in both arrays, and the highest velocity reaches ~ 4.4 km/s in the lid. Since we are lacking long-period Rayleigh waves, the resolution of structure is poor below ~ 150 km in GLIMPSE and ~ 100 km in MELT. Thus we do not show the profile at depths greater than 150 km. GLIMPSE data are better to longer periods and greater depth because an improvement in design reduced instrument noise. Details of the inversion for phase velocity are given in *Weeraratne et al.* [2005].

Figure 7 shows an example of a particular Q_μ model and the resolution kernels for the GLIMPSE region. The starting model for this example had constant Q_μ value of 75 at all depths. The resolution kernels for attenuation are similar for the MELT regions. The resolution kernels become wider with increasing depth, because the sensitivity range of Rayleigh waves increases with period. The fit of the predicted attenuation coefficients to observed attenuation coefficients is excellent at all periods for GLIMPSE (Figure 4). For MELT, the scatter in observed values from point-to-point is somewhat larger than expected for the size of the formal standard deviations. This variation probably stems from fewer sources with poorer azimuthal distribution in the MELT Experiment and thus a greater variation in path coverage when particular events have to be eliminated at

individual periods due to poor signal-to-noise ratios.

Since the inversion for Q_{μ} is an underdetermined problem, we test the effect of initial values of Q_{μ} on the resultant Q_{μ} by using a variety of starting values. The resolved models with different starting values are plotted in Figure 8. The effects of starting values on Q_{μ} models are small at depths shallower than 100 km, but become larger at depths greater than 100 km, which means that our resolution of Q_{μ} at depths greater than 100 km is poor. In order to have model values as close to the real values as possible, we incorporate a priori information, choosing 70 as the starting value, which is the value obtained for the upper 150 km of the mantle beneath the East Pacific Rise from a study of multibounce SH phases [*Ding and Grand, 1993*] and coincides with the averages of 60-90 in the asthenosphere in various global models [see summary in *Romanowicz and Durek, 2000*].

Particular solutions to the inverse problem for Q_{μ} structure may contain features that are suggested, but not required, by oscillations in the data or that are inherited from the starting model. For example, the structure for GLIMPSE has a small peak in Q_{μ} at about 35 km and MELT has a subdued minimum centered at about 70 km that is not present in GLIMPSE (Figure 9). It is tempting to interpret these details in terms of physical properties like differences in melt concentration or water content, but before doing so, it is important to consider what features are statistically resolvable. Because the resolution kernels are reasonably compact, in the sense of not having significant sidelobes, we can summarize the required features in terms of overlapping averages over

resolvable depth ranges, i.e., ranges over which the diagonal elements of the resolution matrix sum to 1.0 pieces of independent information about the system. These resolvable averages and their standard deviations are illustrated in Figures 9c and 9f and do not depend significantly on the starting model. The initial inversion is actually in terms of Q_{μ}^{-1} because there is a linear relationship between γ_R and Q_{μ}^{-1} ; when we translate the results to plot the traditional Q_{μ} versus depth, the uncertainties become asymmetric about the average value.

The required features of the attenuation structures are significant decreases in Q_{μ} with increasing depth, greater attenuation beneath the young seafloor of the MELT array than beneath GLIMPSE, and higher minimum values of Q_{μ} beneath both arrays than are predicted for recent models attributing the origin of the oceanic low velocity zone to the effects of temperature and anelasticity (see discussion below of models of the origin of the LVZ). Both the increase in attenuation with depth and the decrease associated with the greater average age of the GLIMPSE region suggest that the cooling of the oceanic mantle may play a role, although significant conductive cooling is not expected to extend to depths greater than about 30 km in seafloor younger than 10 Ma. The decrease with increasing depth could also be attributed to a decrease in water content, as discussed below. At the 95% confidence level, the average Q_{μ} in the 20-60 km depth range must be greater than about 90 beneath MELT and about 110 beneath GLIMPSE. The best estimates for Q_{μ} in the ~55-120 km depth range are about 87 for MELT and 113 for GLIMPSE, somewhat higher than averages of 60-90 in the asthenosphere in various

global 1-D models [see summary in *Romanowicz and Durek, 2000*] or the value of 70 obtained for the upper 150 km of the mantle beneath the East Pacific Rise from a study of multibounce SH phases [*Ding and Grand, 1993*]. Although the 95% confidence limits on our values overlap the values in these previous studies, they barely reach the most likely range estimated by *Resovsky et al. [2005]* for the global average. Thus, we speculate that the offset may be real, caused by the contribution to apparent attenuation from scattering in the global studies, which has relatively little effect on measurements in local, *in situ* arrays like GLIMPSE and MELT if focusing is properly accounted for. At the longest periods in our study, however, there is not much offset in Q_R from the values at the shortest periods of the global studies near the East Pacific Rise, suggesting that the biggest difference is that our study extends to shorter periods giving higher resolution of the upper 100 km.

These Q_μ models and uncertainties assume that intrinsic attenuation is independent of frequency, as is traditional for most seismological studies. Fundamental mode surface wave observations cannot distinguish between the effects of variations in attenuation caused by frequency dependence of the attenuation mechanism and those caused by depth dependence. The form of the frequency dependence is unclear and should depend on the physical mechanism responsible for the dissipation. Recent experiments suggest that temperature and grain-boundary-sliding effects may take the form $Q^{-1} \propto \omega^{-\alpha}$, with α in the range 0.1 - 0.3. *Jackson et al [2002]* find best fitting value of α to be ~ 0.26 for olivine in the seismic frequency band. Our observations span a

factor of about 4 in frequency; a value of $\alpha = 0.26$ would cause approximately a 30% decrease in Q_R from the shortest period to the longest that would masquerade in our inversion as a decrease in Q_μ with increasing depth. Correcting for this frequency dependence, assuming that this is the dominant mechanism of attenuation, would reduce the contrast between the average velocity from 20 to 40 km and 55 to 120 km by a factor of about two. If this large frequency dependence is correct, it could help provide an explanation for the offset between asthenospheric values in global models and in our study; most of the global studies employ periods greater than about 80 s, while our maximum period is 67 s. Because the mechanism and coefficients are not perfectly known, rather than correcting the data to a common reference frequency, we prefer the alternative approach of finding the apparent attenuation structure neglecting the frequency dependence, then comparing the structure to predictions that incorporate the frequency dependence of the particular model.

Models for the origin of the LVZ

The upper LVZ is characterized by a negative seismic velocity gradient: seismic velocity decreases with depth. In the Earth, there are two major competing factors controlling seismic velocity variation with depth: temperature and pressure. Both of them increase with depth in the Earth. Increasing temperature decreases seismic velocity; whereas increasing pressure decreases seismic velocity. When the temperature gradient is large enough, the temperature effect will overwhelm the pressure effect and lead to

negative seismic velocity gradients. The problem is whether temperature and pressure effects alone are enough to explain the LVZ. The answer is still debated.

For example, *Anderson and Sammis* [1970] argued that the thermal gradient required by the LVZ is too large to satisfy heat flow through the upper mantle and attributed the LVZ partially to the presence of a small amount of melt. They also noted that partial melting in the LVZ could relate to the high concentration of water due to dehydration of hydrated trace minerals. However, *Karato and Jung* [1998] argued that the presence of a small amount of melt has no significant effect on seismic velocity for the range of melt fraction expected over most upper mantle, and proposed instead that water dissolved in solid minerals can significantly reduce seismic wave velocities through anelastic relaxation. At the small melt fraction expected in most of the Earth's upper mantle, *Karato and Jung* [1998] speculated that partial melting will increase seismic wave velocities through the removal of water from minerals such as olivine. They concluded that the LVZ is a layer where no significant melt is present and a high concentration of water is retained. The process of forming the crust removes the melt from the overlying lithosphere, creating a high velocity lid. On the other hand, based on finite element calculation considering the geometries of partial melt included in samples taken directly from laboratory experiments, *Hammond and Humphreys* [2000] showed that V_p and V_s can be reduced at least 3.6% and 7.9% per percent partial melt, respectively. Melt effects on seismic velocity greatly depend on the distribution and geometries of partial melt [*Schmeling*, 1985], which may be not correctly modeled in the experiments referred

to by *Karato and Jung* [1998].

Recently, by comparing their calculations with seismic observations for shear wave velocity in 100 Ma old oceanic lithosphere, *Stixrude and Lithgow-Bertelloni* [2004] argued that the LVZ is the natural result of pressure and temperature effects on elastic wave velocity. By extrapolating their calculation to younger lithosphere, they claimed that a solid-state low velocity zone provides a satisfactory explanation of shear velocities except in the immediate vicinity of mid-oceanic ridges, where partial melt probably occurs. Similarly, *Faul and Jackson* [2005] also claimed that the LVZ can be explained by solid-state mechanisms without the presence of partial melt or fluid. They took seismic attenuation into account in constructing a model for the origin of the LVZ beneath both old oceanic and continental regions, and showed that the model can reproduce the overall pattern of velocity variations with age in the oceanic mantle. However, neither sets of authors explain the abrupt decrease in velocity observed at the base of old oceanic lithosphere [*Revenaugh and Jordan*, 1991; *Gaherty et al.*, 1996; *Collins et al.*, 2001; *Li et al.*, 2004] and both appeal to anelasticity to play a major role in the reducing velocities in the LVZ, with the implication that where high temperatures prevail beneath young seafloor, Q_{μ} should be very low. With the availability of regional shear wave velocities and attenuation data discussed in preceding sections, we try to constrain the origin of LVZ observed in the young oceanic plate.

Model predictions of shear velocity and attenuation

Faul and Jackson [2005] developed a model to calculate shear wave velocity (V_s) and attenuation (Q_μ) for melt-free polycrystalline aggregates of olivine at upper mantle temperature and seismic frequencies by fitting experimental shear modulus and attenuation data [*Jackson et al.*, 2002]. We use the same model to calculate shear wave velocity V_s and Q_μ for the GLIMPSE and MELT regions, and then compare the results of these calculations with our seismological observations.

Following *Faul and Jackson* [2005], the geotherms in the oceanic settings can be modeled as a conductive layer (lithosphere) overlying a convective layer (asthenosphere) joined smoothly by a transition layer. The temperature profile within the conductive layers can be described by the half-space cooling model,

$$T = T_0 + (T_{ad} - T_0) \operatorname{erf}\left(\frac{z}{2\sqrt{(\kappa t)}}\right), \quad (2)$$

where $T_0 = 0$ °C is the temperature at the ocean floor, T_{ad} is the initial adiabatic temperature of the upper mantle, z is depth, t is the age of ocean floor and $\kappa = 1 \times 10^{-6} \text{ m}^2 \text{ s}^{-1}$ is the thermal diffusivity. Adiabatic temperatures are calculated using

$$T_{ad} \approx T_p \left(1 + \frac{\alpha_T g z}{c_p}\right), \quad (3)$$

where T_p is the potential temperature, z is the depth and g is the acceleration of gravity. α_T is the coefficient of thermal expansion and c_p is the specific heat at constant pressure, both of which are assumed to be independent of pressure and temperature. We

choose $T_p = 1300$ °C to coincide with the model of *Faul and Jackson* [2005], and in agreement with other recent thermal models for young seafloor in the Pacific. We set 2 Ma and 6 Ma as the average seafloor ages for the MELT and GLIMPSE regions respectively.

Results and discussions

Expressions relating shear velocity and Q_μ to temperature and pressure are given by *Faul and Jackson* [2005]; the forms of the relationships are more complicated than the simple $Q^{-1} \sim \omega^{-\alpha}$ proportionality often assumed. The model calculations include the approximate effects of the intrinsic frequency dependence of Q by associating a characteristic frequency at each depth with the frequency of the Rayleigh wave most sensitive to structure at that depth.

Figure 9 shows temperature, shear velocity, and Q_μ calculated for young oceanic lithosphere in the MELT and GLIMPSE regions for the *Faul and Jackson* model compared to observed shear wave velocity and attenuation from our Rayleigh wave observations. Predicted shear wave velocities exhibit negative gradients in the uppermost mantle due to the large temperature gradient in the conductively cooling layer. The depth of the velocity minimum increases with seafloor age. At greater depths, shear wave velocities increase with depth due to the effects of pressure on seismic velocities overwhelming the effects of temperature. Although the model approximately reproduces the velocity variations in young seafloor, in detail, there are some differences. For

example, the depth of the predicted velocity minimum is shallower than the depth of the observed minimum. The predicted minimum is ~30 km in the MELT region and ~50 km in the GLIMPSE region, whereas the depth of the observed minimum is ~70-80 km in both regions. Although the models match the shear velocities reasonably well, they predict attenuation that is much greater than observed (Figure 9c,f). The predicted values of Q_{μ} are about 20 at depths greater than ~20 km in the MELT array and ~35 km in the GLIMPSE array. These predicted values are well below the 99% confidence limits in either the 20 to 60 or 55 to 120 km depth ranges of both arrays. The implication is that the anelastic effects of temperature variations are not primarily responsible for the oceanic low velocity zone.

If the temperature dependence of attenuation and velocity is large enough to match the velocity and Q structure of 100 Ma oceanic upper mantle, then there should be very low Q in the hot, young mantle near mid-ocean ridges, which simply is not observed. We conclude that the temperature dependence of attenuation must be less than predicted and that some other mechanism must be at least partially responsible for the drop in velocity and attenuation beneath the lithosphere in old seafloor and for the variation in velocity with age of the seafloor.

A high velocity lid with thickness ~60 km is observed beneath ~100 Ma old seafloor by *Gaherty et al.* [1999]. They argued that the transition from lid to LVZ is not solely controlled by temperature since the lid should be much thicker in the old oceanic plate than in the young oceanic plate if temperature is the dominant controlling factor. We find

a thickness of ~ 40 km on the west side of the East Pacific Rise where the seafloor subsides anomalously slowly [The MELT Seismic Team, 1998] and there is a 60-km-thick, electrically resistive layer on the east side [Evans et al., 2005] where subsidence is normal. The relatively uniform thickness of the high velocity lid beneath young and old seafloor implies that the lid is formed near the spreading ridge and remains nearly constant in thickness with distance away from ridge, although the average velocities increase. The mechanism behind the initial formation of the lid could be related to the extraction of water from olivine by partial melting. Since the solubility of water in the melt is 2-3 orders of magnitude greater than in the mantle minerals [Hirth and Kohlstedt, 1996], partial melting above the depth of “dry” solidus (~ 65 km) and removal of the melt to form the crust at the spreading center can effectively dry out the upper mantle. Hirth and Kohlstedt [1996] showed that the viscosity of “dry” olivine aggregate could be 2 or 3 orders of magnitude larger than the “damp” olivine aggregate in the MORB source region, which could produce a high viscosity lid above the dry solidus at about ~ 65 km beneath young oceanic regions. The observation beneath East Pacific Rise of high electrical resistivity above 60 km and low, anisotropic resistivity deeper than 60 km supports the argument that the base of an oceanic plate is not only controlled by temperature but also by chemical composition, particularly water content [Evans et al., 2005].

Based on the model of extraction of water, there should be a corresponding sharp change of attenuation between lid and LVZ since water can significantly enhance

anelasticity of an olivine aggregate. The decrease in Q with depth may be at least partially attributable to an increase in water content. Experimental studies of existing data on Q [Sato *et al.*, 1989a; and Jackson *et al.*, 1992] and theoretical analysis suggest that water should enhance attenuation significantly. Jackson *et al.* [1992] found that dunite specimens that were pre-dried have Q values 2-3 times larger than specimens that were not pre-dried. Water reduces seismic velocity indirectly via enhancing the anelasticity of the olivine aggregate in the upper mantle. We investigate whether anelasticity due to water or some other agent can explain the low shear wave velocities we observe beneath young seafloor.

The effects of temperature (T) and pressure (P) on seismic velocities including both anharmonicity and anelasticity can be expressed as [Minster and Anderson, 1981]:

$$V_s(\omega, T, P) = V_0(T, P) \left[1 - \frac{1}{2} \cot\left(\frac{\pi\alpha}{2}\right) Q^{-1}(\omega, T, P) \right], \quad (4)$$

where $V_0(T, P)$ is the seismic wave velocity including only anharmonic effects. The anharmonic effects are independent of frequency and have been well constrained from laboratory experiments. The second part on the right hand is the anelastic effect due to seismic wave attenuation assuming that dissipation (Q^{-1}) is dependent on frequency with the form, $Q^{-1} \sim \omega^{-\alpha}$. Laboratory experiments and seismic observations suggest $\alpha = 0.1 - 0.3$. We set the value of α to 0.15 in the following calculations. Adopting a value of 0.26 [Jackson *et al.*, 2002] produces a smaller effect.

Based on self-consistent computation of phase equilibrium and physical properties,

Stixrude and Lithgow-Bertelloni [2005] developed a new model of seismic velocities in the oceanic upper mantle based on expected mineral abundance and reactions. In the vicinity of the LVZ, they found that the anharmonic shear velocity along oceanic geotherms in the upper mantle can be approximated by the equation,

$$V_o = 4.77 + 0.0380(P, z/29.8) - 0.000378(T - 300), \quad (5)$$

with pressure P in GPa, depth z in km, temperature T in K, and velocity V_o in km/s.

Stixrude and Lithgow-Bertelloni [2005] showed that these predicted anharmonic velocities underpredict the extent of the LVZ, i.e., do not predict low enough velocities beneath seafloor of 100 Ma age. They concluded, without specifying the mechanism responsible for the high attenuation, that the anelastic effect of attenuation on velocity is probably responsible for the discrepancy. Adopting their approximate velocity model, we show that neither the direct effects of temperature on elasticity nor the indirect effects of anelasticity explain the low velocities observed beneath young seafloor.

The calculated elastic velocities (V_o) using equation (4) and V_s with anelastic correction using the preferred Q_μ models (Figure 9c and f) are plotted in Figure 10 along with the observed shear wave velocities for both regions. The anelastic correction using the observed dissipation (Q_μ^{-1}) for shear velocity is about 0.05-0.1 km/s. The observed shear wave velocities are much lower than the calculated V_s . The greatest difference between the observed and the predicted occurs at the depth of minimum velocity with discrepancy of 0.25 to 0.35 km/s. The discrepancy would be larger with $\alpha = 0.26$ or slightly smaller using *Ding and Grand's* [1993] average Q value of ~ 70 at all depths.

The large discrepancy between the observations and predictions implies that there are other factors affecting seismic velocities. One possible factor is the uncertainty in the mantle potential temperature and the lithospheric geotherm. However, the approximate relationship (equation 5) shows that the change of shear wave velocity is 0.038 km/s per 100 °K, which requires about 750 degrees to satisfy the ~0.3 km/s discrepancy, much too large to be possible in upper mantle. Another factor to reduce seismic velocities is the presence of partial melt beneath the young oceanic plate. Partial melting has often been invoked to explain the origin of the low velocity zone [Anderson and Sammis, 1969; Sato *et al.* 1989b]. Partial melt has two different effects on seismic velocity: the direct effect due to the difference of elastic properties between melt and solid, and the indirect effects due to the enhanced anelasticity with the presence of partial melt, which have been included in the anelastic correction in the preceding paragraph. The anelastic effect depends sensitively on the mechanism of attenuation associated with melting [Jackson *et al.*, 2004; Faul *et al.*, 2004]. If it is melt squirt, then the dissipation peak may lie outside the seismic frequency band and cause little velocity dissipation. The effect of melting-related grain boundary sliding may be much larger. The direct velocity reduction depends on the aspect ratio of the melt pockets [Schmeling, 1985]. Hammond and Humphreys [2000] have shown that direct V_s reduction per percent partial melt are at least 7.9% for realistic melt distributions and even higher values for velocity reduction are possible above 1% melt fraction. Partial melting is expected above ~115 km depth [Hirth and Kohlstedt, 1996] in the upper mantle within the “wet” melting regime where

there is upwelling beneath a spreading ridge. The amount of partial melt in the depth range is not well constrained. *Hirth and Kohlstedt* [1996] estimated that 1% to 2% melt could be produced in the depth interval between the “dry” solidus (~65 km) and the water-influenced solidus (~115 km). However, *Plank and Langmuir* [1992] estimated that only 0.1-0.2% melt is present.

If we assume the discrepancy of shear velocities is totally due to the presence of partial melt and the direct effects of partial melt on seismic velocities is predictable by the model of *Hammond and Humphrey* [2000], we can calculate melt fraction at different depths. Calculated melting fraction from the shear wave discrepancy based on the assumptions is plotted in Figure 11. Melt fraction increases with depth in the uppermost mantle, and then reaches maximum value about 1% at the depth (~70 km) of velocity minimum. Note that velocities and therefore melt fractions are poorly constrained at depths >100 km in the MELT array. Melt fraction decreases with increasing depth below the velocity minimum. The range of melt fraction is consistent with the estimation by *Hirth and Kohlstedt* [1996], and substantially higher than the value of *Plank and Langmuir* [1992].

Less than 1% melt resident in the uppermost mantle shallower than ~65 km implies that melt is extracted very efficiently as the compositions of basalts require 10% to 20% melting of the MORB source. *Hirth and Kohlstedt* [1996] suggested that high viscosity due to the extraction of water by partial melting at depths above “dry” solidus might be large enough to produce lateral pressure gradients, which enable focusing melting

migration to the ridge axis, while the relatively low viscosity within the depth range between the “dry” solidus and “wet” solidus leads to inefficient removing of melt, and retentions of melt in the LVZ source region.

Based on above analysis, partial melt and water content are required to explain the observed LVZ beneath the young Pacific plate. For the old Pacific plate, *Faul and Jackson* [2005] argued that the LVZ can be explained by solid-state mechanisms without the presence of melt or fluid. However, to match the shear wave velocity minimum in the LVZ beneath 100 Ma old seafloor, high attenuation with Q_μ lower than 50 is required in their model. The attenuation correction is a critical parameter in matching the velocity minimum. Extrapolation of temperature and pressure conditions for their model to young seafloor predicts $Q_\mu \sim 20$. Since our observation of Q_μ is much larger than 50 in the young oceanic plate, it is reasonable to consider that Q_μ in the low velocity zone beneath old seafloor like 100 Ma should be higher than 50 and/or that some mechanism other than simply increasing temperature is responsible for the low Q and low shear wave velocity. Higher Q_μ will lead to smaller reduction in seismic velocities, so that partial melt or water is required to reduce seismic velocities to the minimum value beneath old seafloor. To better constrain the origin of LVZ in older seafloor, regional attenuation (Q_μ) should be investigated.

Conclusions

We invert phase and amplitude data of Rayleigh waves recorded at ocean-bottom

seismometers (OBS) in very young (less than 10 Ma) seafloor in two arrays near the East Pacific Rise, the MELT array and the GLIMPSE array, for shear wave velocity (V_s) and attenuation (Q_μ). The finite-frequency scattering of surface waves due to elastic heterogeneities is taken into account with 2-D sensitivity kernels. The scattering effects on amplitude can be separated from the attenuation effects on amplitude in the simultaneous inversion for lateral phase velocity and attenuation.

A high velocity lid with negative gradient in the uppermost mantle overlying a low velocity zone is observed in both regions. The highest velocity in the high velocity lid reaches 4.4 km/s. The minimum of shear wave velocity in the low velocity zone is ~ 4.0 km/s. Our Q_μ models exhibit a sharp change over the depth range of 40 to 60 km. The change of Q_μ and S-wave velocity with depth is partly due to the change of water content in the upper mantle as a result of the extraction of water by large fractional melting above ~ 65 km. Anelasticity effects on seismic velocities from attenuation are not sufficient to explain the observed low velocity zone. $\sim 1\%$ partial melting present in the low velocity zone is required to satisfy the minimum value of shear wave velocity. A combined model with partial melt in the depth range between the 'dry' solidus and 'wet' solidus and dehydration of peridotite above the 'dry' solidus can explain the origin of observed low velocity zone.

References

- Anderson, D.L. and C. Sammis, Partial melting in the upper mantle, *Phys. Earth Planet. Inter.*, 3, 41-50, 1970.
- Anderson, D.L., and C. Sammis, The low velocity zone, *Geofisica International*, 9, 3-19, 1969.
- Billien, M., J.-J. Leveque, and J. Grampert, Global maps of Rayleigh wave attenuation for periods between 40 and 150 seconds, *Geophys. Res. Lett.*, 27, 3619-3622, 2000.
- Collins, J.A., F.L. Vernon, J.A. Orcutt, R.A. Stephen, K.R. Peal, F.B. Wooding, F.N. Spiess, and J.A. Hildebrand, Broadband seismology in the oceans: Lessons from the Ocean Seismic Network Pilot Experiment. *Geophys. Res. Lett.*, 28, 49-52, doi: 10.1029/2000GL011638, 2001.
- Cong, L., and B.J. Mitchell, Seismic velocity and Q structure of the middle eastern crust and upper mantle from surface wave dispersion and attenuation, *Pure appl. Geophys.*, 153, 503-538, 1998.
- Ding, X.-Y., and S.P. Grand, Upper mantle Q structure beneath the East Pacific Rise, *J. Geophys. Res.*, 98, 1973-1985, 1993.
- Evans, R.L., G. Hirth, K. Baba, D. Forsyth, A. Chave, and R. Mackie, Geophysical evidence from the MELT area for compositional controls on oceanic plates, *Nature*, in press, 2005.

Faul, U.H., and I. Jackson, The seismological signature of temperature and grain size variations in the upper mantle, *Earth Planet. Sci. Lett.*, 234, 119-134, 2005.

Faul, U.H., J.D. Fitz Gerald, and I. Jackson, Shear wave attenuation and dispersion in melt-bearing olivine polycrystals:2. Microstructural interpretation and seismological implications, *J. Geophys. Res.*, 109, B06202, doi:10.1029/2003JB002407, 2004.

Forsyth, D.W. and A. Li. Array-analysis of two-dimensional variations in surface wave phase velocity and azimuthal anisotropy in the presence of multi-pathing interference, *Seismic Data Analysis and Imaging with Global and Local Arrays*, (A. Levander and G. Nolet, ed.), AGU Geophysical Monograph, in press, 2005

Forsyth, D.W., S. Webb, L. Dorman, and Y. Shen, Phase velocities of Rayleigh waves in the MELT experiment on the East Pacific Rise, *Science* 280,1235-1238,1998.

Gaherty, J.B., M. Kato, and T.H. Jordan, Seismological structure of the upper mantle: a regional comparison of seismic layering, *Phys. Earth. Planet. Int.*, 110, 21-41,1999.

Gaherty, J.B., T.H. Jordan, and L.S. Gee, Seismic structure of the upper mantle in a central Pacific corridor, *J. Geophys. Res.*, 101, 22291-22309, 1996.

Gung, Y., and B. Romanowicz, Q tomography of the upper mantle using three-component long-period waveforms, *Geophys. J. Int.*,157, 813-830, 2004.

Gutenberg, B., *Physics of the Earth's Interior*, Academic Press, New York, 1959.

Hammond, W.C., and E.D Humphreys, Upper mantle seismic wave attenuation: Effects of

- realistic partial melt distribution, *J. Geophys. Res.*, 105, 10,987-10,999, 2000.
- Hirth, G., and D.L. Kohlstedt, Water in the oceanic upper mantle: implications for rheology, melt extraction and the evolution of the lithosphere, *Earth Planet. Sci. Lett.* 144, 93-108, 1996.
- Jackson, I., J.D. Fitz Gerald, U.H. Faul, and B.H. Tan, Grain-size-sensitive seismic wave attenuation in polycrystalline olivine, *J. Geophys. Res.*, 107(B12), 2360, doi:10.1029/2001JB001225, 2002.
- Jackson, I., M.S. Paterson, and J.D. FitzGerald, Seismic wave dispersion and attenuation in Aheim dunite: an experimental study, *Geophys. J. Int.* 108, 517-534, 1992.
- Jackson, I., U.H. Faul, J.D. Fitz Gerald, and B.H. Tan, Shear wave attenuation and dispersion in melt-bearing olivine polycrystals: 1. Specimen fabrication and mechanical testing, *J. Geophys. Res.*, 109, B06201, doi:10.1029/2003JB002406, 2004.
- Karato, S. and H. Jung, Water, partial melting and the origin of the seismic low velocity and high attenuation zone in the upper mantle, *Earth Planet. Sci. Lett.* 157, 193-207, 1998.
- Li, X., R. Kind, X. Yuan, I. Wolbern, and W. Hanka, Rejuvenation of the lithosphere by the Hawaiian plume, *Nature*, 427, 827-829, 2004.
- MELT Seismic Team, Imaging the deep seismic structure beneath a mid-ocean ridge: The MELT Experiment, *Science*, 280, 1215-1218, 1998.
- Minster, J.B., and D.L. Anderson, A model of dislocation-controlled rheology for the

- mantle, *Philos. Trans. R. Soc.*, London A 299, 319-356, 1981.
- Mitchell, B.J., Anelastic structure and evolution of the continental crust and upper mantle from seismic surface wave attenuation, *Rev. Geophys.*, 33, 441-462, 1995.
- Plank, T., and C.H. Langmuir, Effects of the melting regime on the composition of the oceanic crust, *J. Geophys. Res.*, 97, 19749-19770, 1992.
- Resovsky, J., J. Trampert, and R.D. Van der Hilst, Error bars for the global seismic Q profile, *Earth Planet. Sci. Lett.*, 230, 413-423, 2005.
- Revenaugh, J., and T.H. Jordan, Mantle layering from ScS reverberations, 3. The upper mantle, *J. Geophys. Res.*, 96, 19781-19810, 1991.
- Richards, M.A., W.S. Yang, J.R. Baumgardner, and H.P. Bunge, Role of a low-viscosity zone in stabilizing plate tectonics: Implications for comparative terrestrial planetology, *Geochem. Geophys. Geosyst.*, 2, 2001.
- Ritsema, J., and H. J. van Heijst, Seismic imaging of structural heterogeneity in Earth's mantle: Evidence for large-scale mantle flow, *Science Progress*, 83, 243-259, 2000.
- Romanowicz, B., and J.J. Durek, Seismological constraints on attenuation in the Earth: A review, in *Earth's Deep Interior, Mineral Physics and Tomography from the Atomic to the Global Scale*, *Geophys. Monogr. Ser.*, 117, edited by S. Karato et al., pp. 161-180, AGU, Washington, D.C., 2000.

Saito, M., DISPER80: A subroutine package for the calculation of seismic normal-mode solutions, *seismological algorithms*, edited by Doornbos, D. J., Academic Press, 293-319, 1988.

Sato, H., I.S. Sacks, T. Murase, G. Muncill, H. Fukuyama, Qp-melting temperature relation in peridotite at high pressure and temperature: attenuation mechanism and implications for the mechanical properties of the upper mantle, *J. Geophys. Res.*, 94, 10647-10661, 1989a.

Sato, H., I. S. Sacks, and T. Murase, The use of laboratory velocity data for estimating temperature and partial melt fraction in the low-velocity zone – comparison with heat-flow and electrical-conductivity studies, *J. Geophys. Res.*, 94, 5689-5704, 1989b.

Schmeling, H., Numerical experiments on the influence of partial melt on elastic, anelastic, and electric properties of rocks, part I., Elasticity and anelasticity, *Phys. Earth Planet. Int.*, 41, 34-57, 1985.

Selby, N.D. and J.H. Woodhouse, The Q structure of the upper mantle: Constraints from Rayleigh wave amplitudes, *J. Geophys. Res.*, 107(B5), 2097, doi:10.1029/2001JB000257, 2002.

Shankland, T.J., and H.S. Waff, Partial melting and elasticity-conductivity anomalies in upper mantle, *J. Geophys. Res.*, 82, 5409-5417, 1977.

Stixrude L., and C. Lithgow-Bertelloni, Mineralogy and elasticity of the oceanic upper

mantle: Origin of the low-velocity zone, *J. Geophys. Res.*, 110, B03204, doi:10.1029/2004JB002965, 2005.

Weeraratne, D.S., D.W. Forsyth, and Y. Yang, Rayleigh wave tomography of the upper mantle beneath intraplate seamount chains in the south Pacific, to be submitted to *J. Geophys. Res.*, 2005

Yang Y., and D.W. Forsyth, Regional tomographic inversion of amplitude and phase of Rayleigh waves with 2-D sensitivity kernels, submitted to *Geophys. J. Int.*, 2005.

Zhou Y., F.A. Dahlen, and G. Nolet, 3-D sensitivity kernels for surface-wave observables, *Geophys. J. Int.*, 158, 142-168, 2004.

Figure Captions

1. Locations of the two OBS arrays marked with the small gray squares in the global map. The color in the global map shows shear velocity model at the depth of 100 km from *Ritsema et al.* [2000]. The bottom image shows the bathymetry for the study region with white circles and triangles representing the MELT array and red triangles representing the GLIMSPE array.
2. Azimuthal equidistant projections of earthquakes (a and c) and great-circle ray paths (b and d) at a period of 25 s in the MELT region (top) and the GLIMPSE region (bottom). Triangles and circles represent deployed OBSs. The white line in (b) marks

- the spreading center.
3. Tomographic images of Rayleigh wave phase velocities at a period of 18 s in the MELT (top) and GLIMSPE (bottom) regions. Triangles and circles represent deployed OBSs. The white line in (a) marks the spreading center. Black contours in (b) shown the bathymetry. Note the great lateral variations in phase velocities.
 4. Variation of residual amplitudes with propagating distances at a period of 16 s in the GLIMSPE region. Each circle represents the average residual amplitude in each 50-km distance interval over all used events. Error bars represent the standard deviations of the average residual amplitudes. Note the systematic decay trend of residuals with distances.
 5. Attenuation coefficients determined from Rayleigh waves. Thin solid line with circles and thin dashed line with triangles are the observed values for the GLIMSPE array and the MELT region respectively. Bold solid line and bold dash line is the predicted values for the GLIMSPE region and the MELT region respectively.
 6. 1-D shear velocity models beneath the GLIMPSE region (solid line with circles) and the MELT region (dashed line with triangles).
 7. Q_{μ} model (left) and resolution kernels (right) for the GLIMSPE region. The resolution kernels are plotted for depths of 15, 30, 50, 70 and 90 km. Well-resolved average Q_{μ} models in three depth intervals are plotted in the left. The rank of resolution is close to one for each average Q_{μ} . The horizontal extent of each rectangle represents standard errors. The middle line in each rectangle represents the best-resolved

- average value of Q_{μ} at that depth interval.
8. Q_{μ} models obtained using different starting values at the GLIMPSE region. The starting values are shown in the legend.
 9. Calculated temperature (a and d), shear wave velocity (b and e) and Q_{μ} (c and f) profiles based on the model of *Faul and Jackson* [2005] for the MELT array (top panels) and the GLIMPSE array (bottom panels). The dashed line in (a) and (e) shows the 1300°C adiabat. Observed shear-wave velocity and Q_{μ} from our study are plotted together in corresponding panels using bold lines. Well-resolved average Q_{μ} models in three depth intervals are plotted at (c) and (f) for the MELT array and GLIMPSE array respectively. The meaning of each rectangle is the same as figure 4.
 10. Calculated elastic velocity V_0 (dashed line) and shear velocity V_s (thin solid line) with anelastic corrections beneath the MELT region (left) and GLIMPSE region (right). The attenuation Q_{μ} for anelastic corrections is shown in fig.2. For comparison, observed shear wave velocity is plotted using bold lines. Note that the observed shear velocity (bold lines) is much slower than the calculated shear velocity V_s .
 11. Calculated melt fraction based on shear wave discrepancy between seismic observations and model predictions beneath the MELT region (dashed line) and GLIMPSE region (solid line).

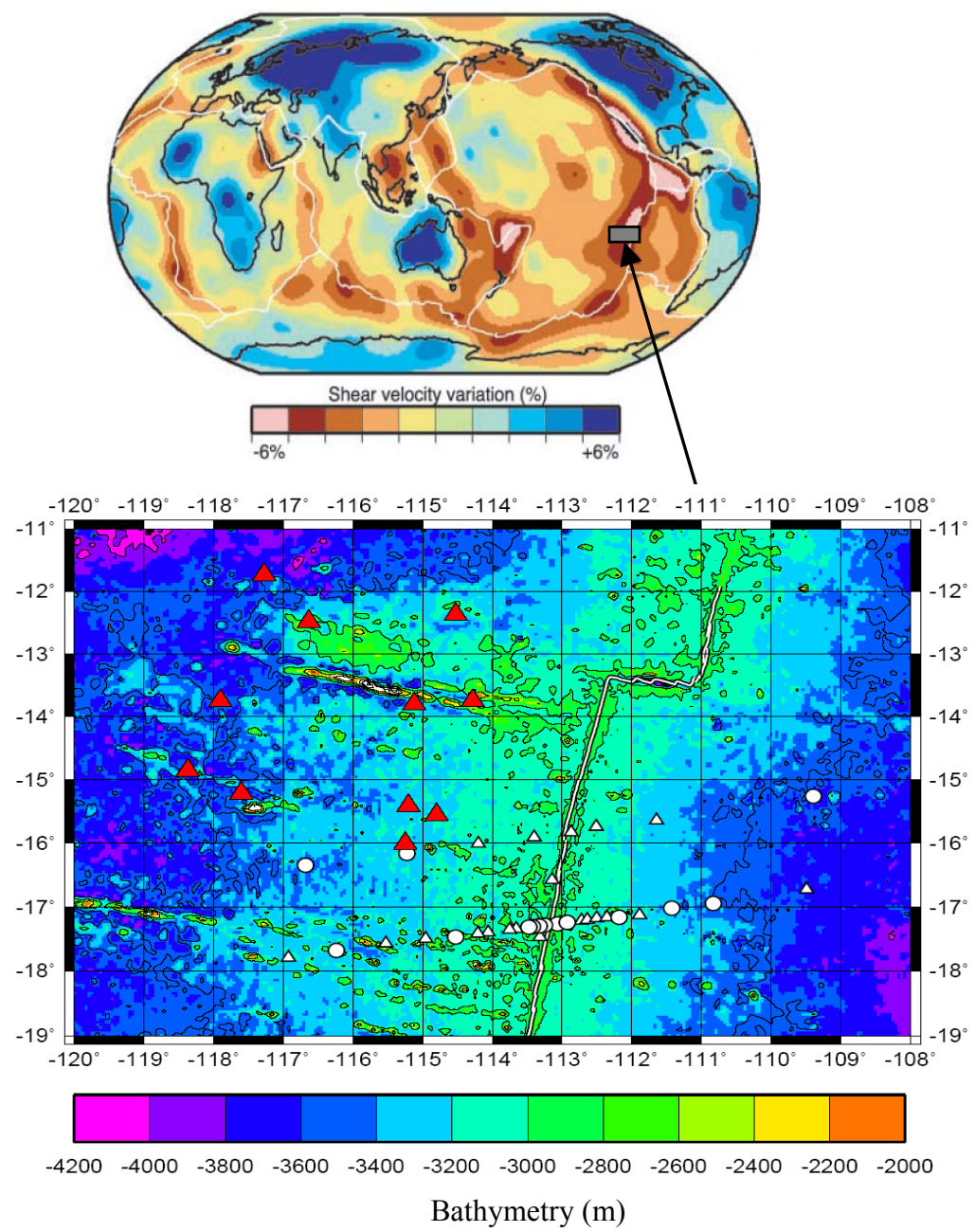
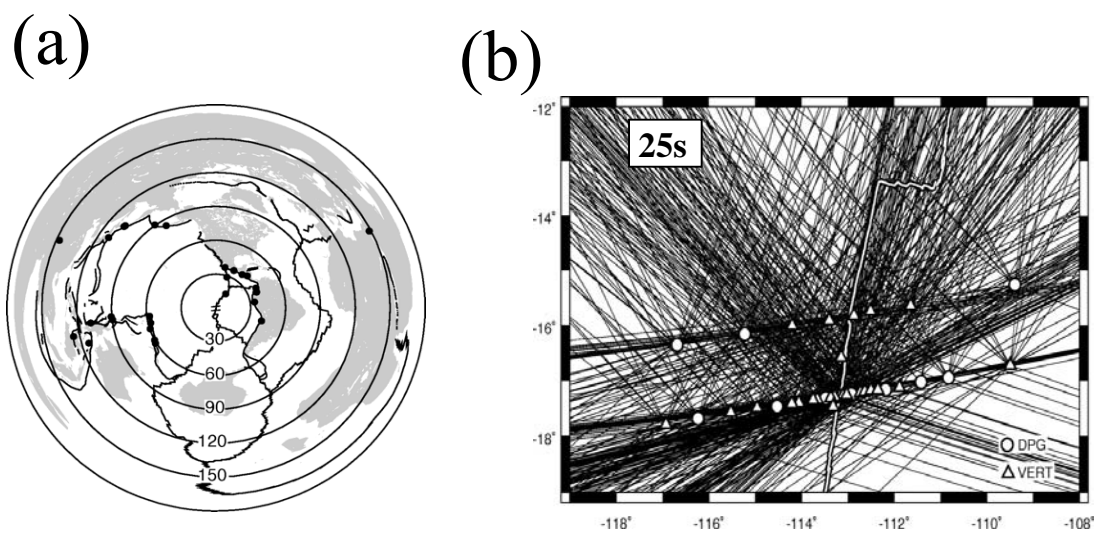


Figure 1

MELT



GLIMPSE

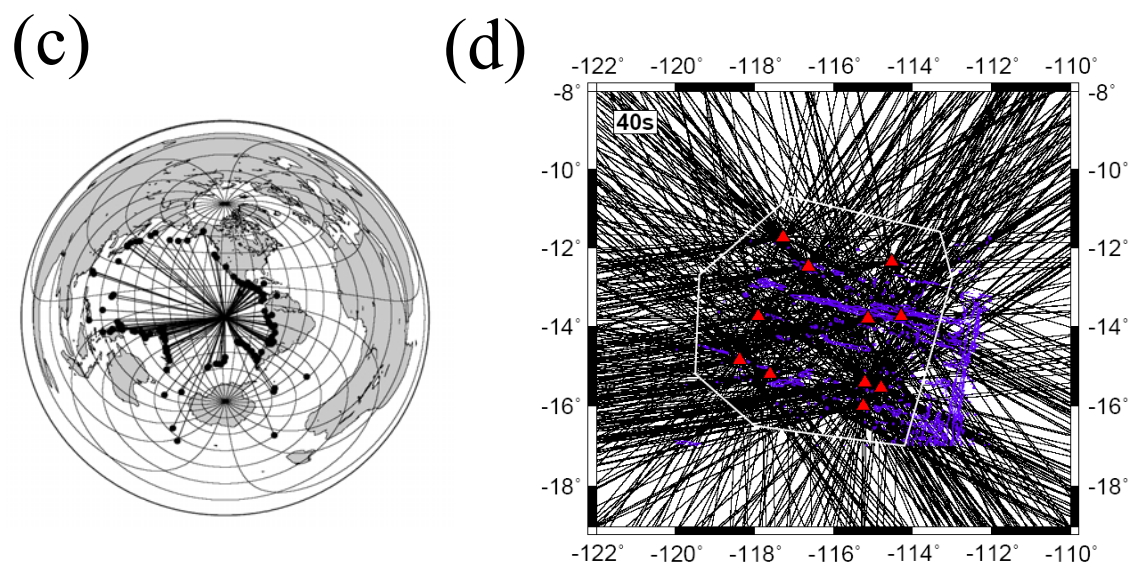


Figure 2

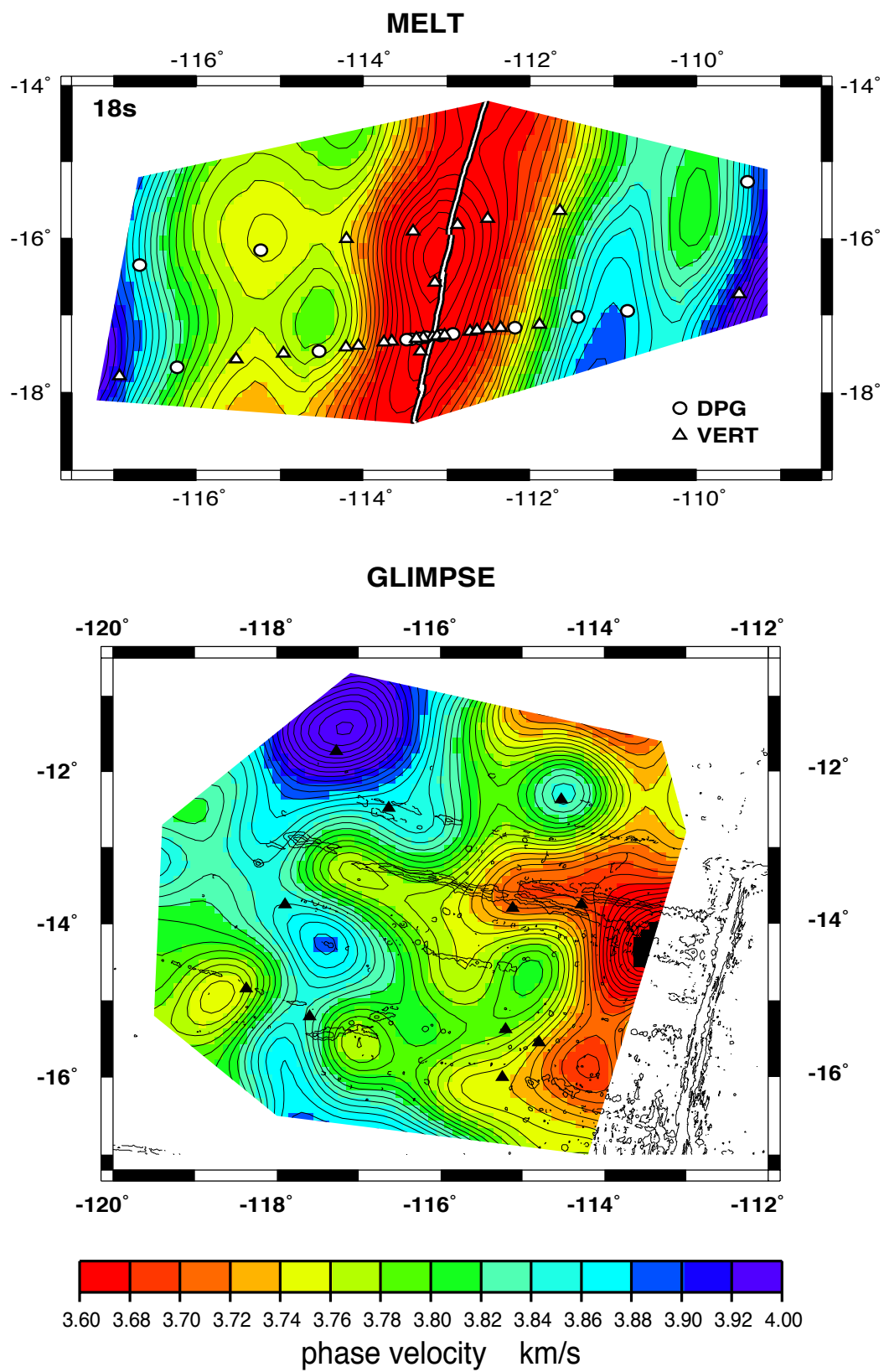


Figure 3

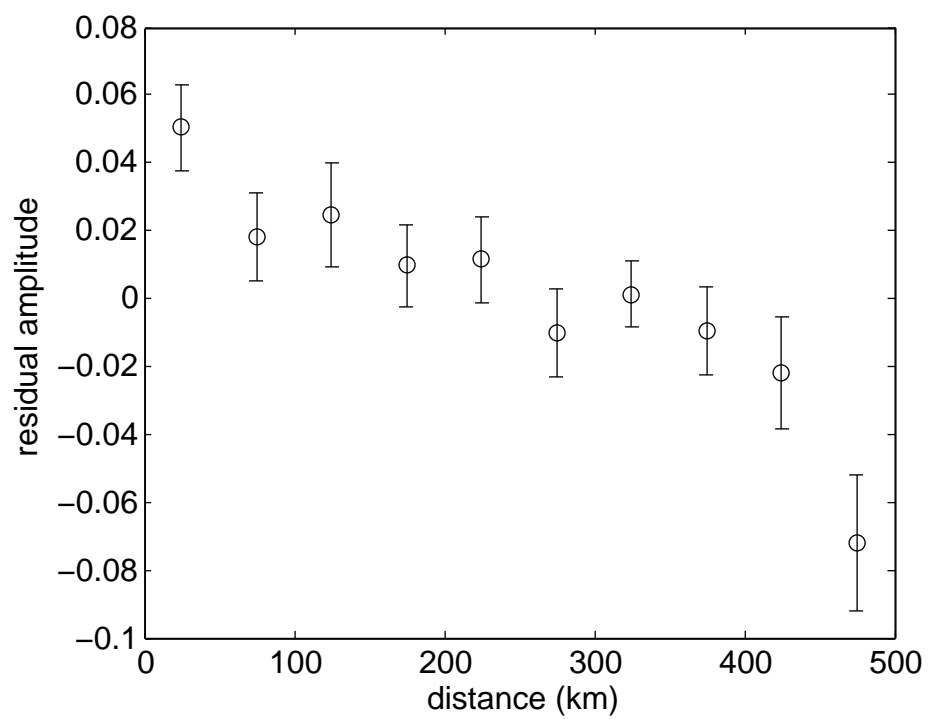


Figure 4

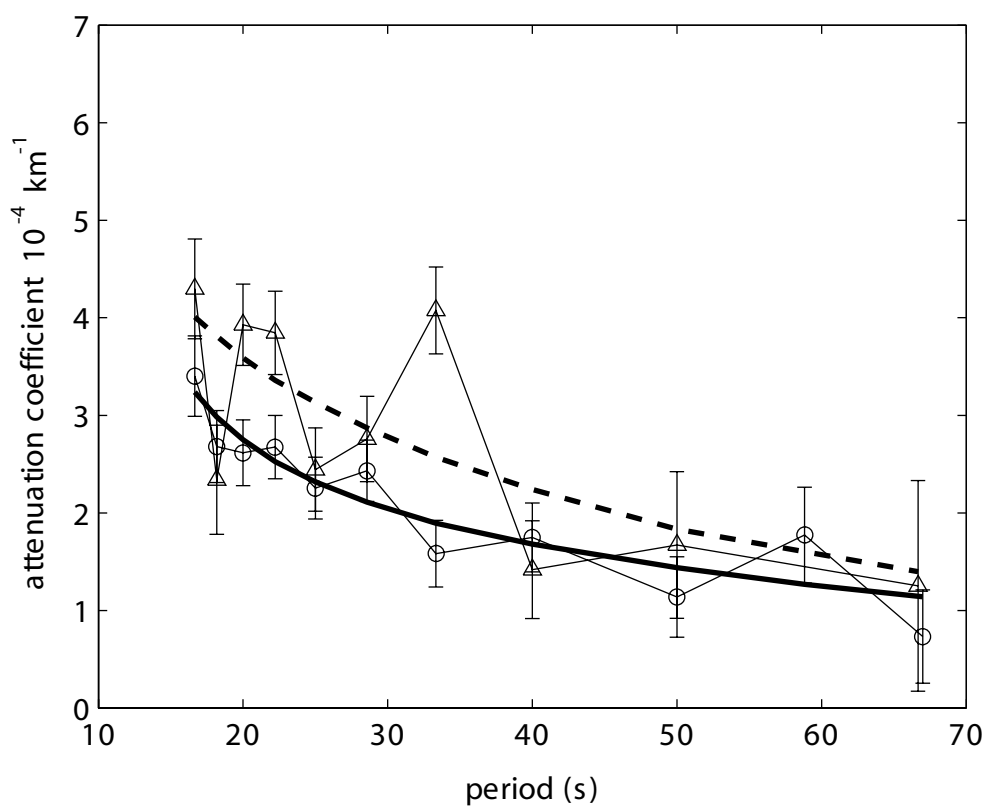


Figure 5

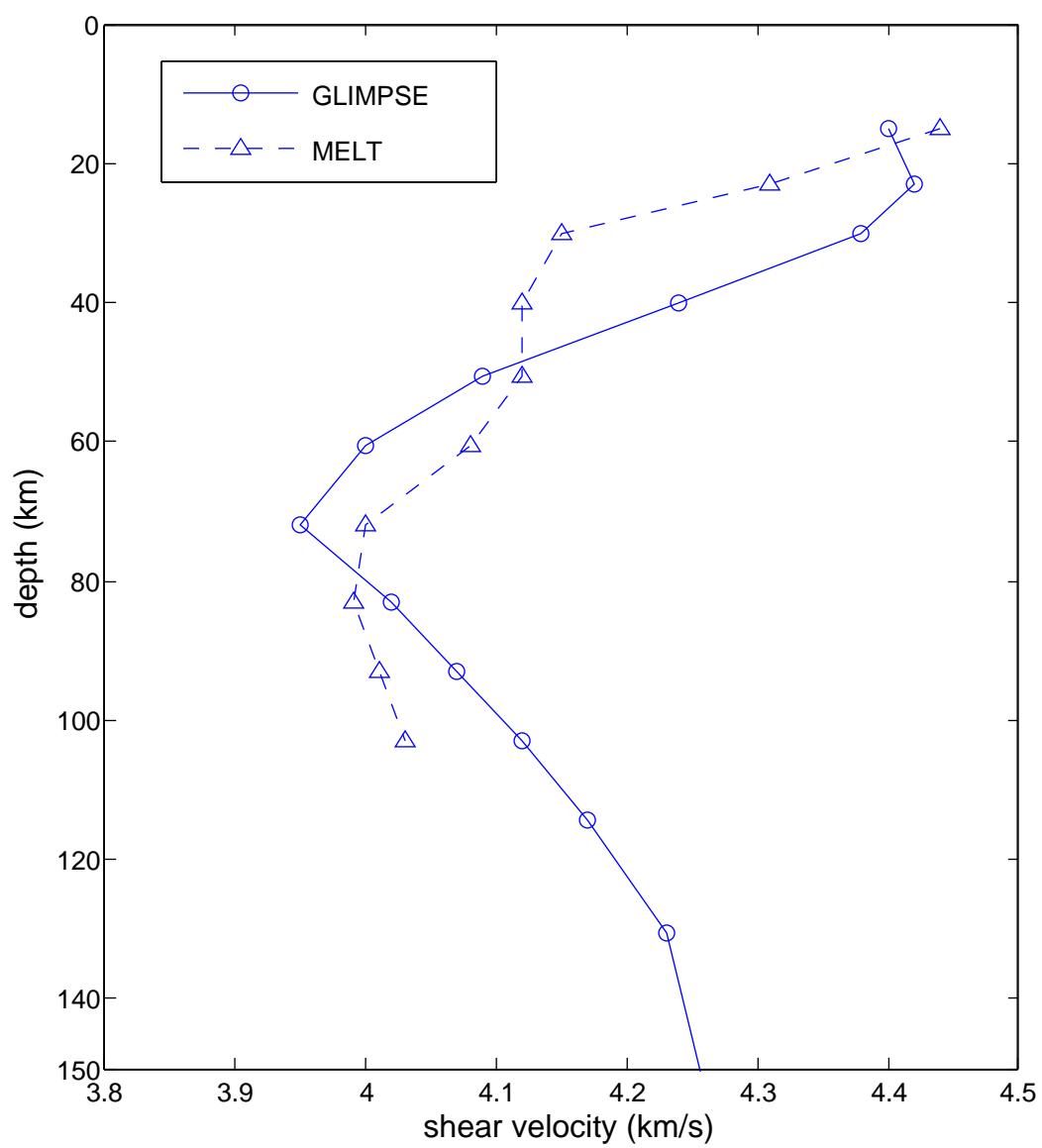


Figure 6

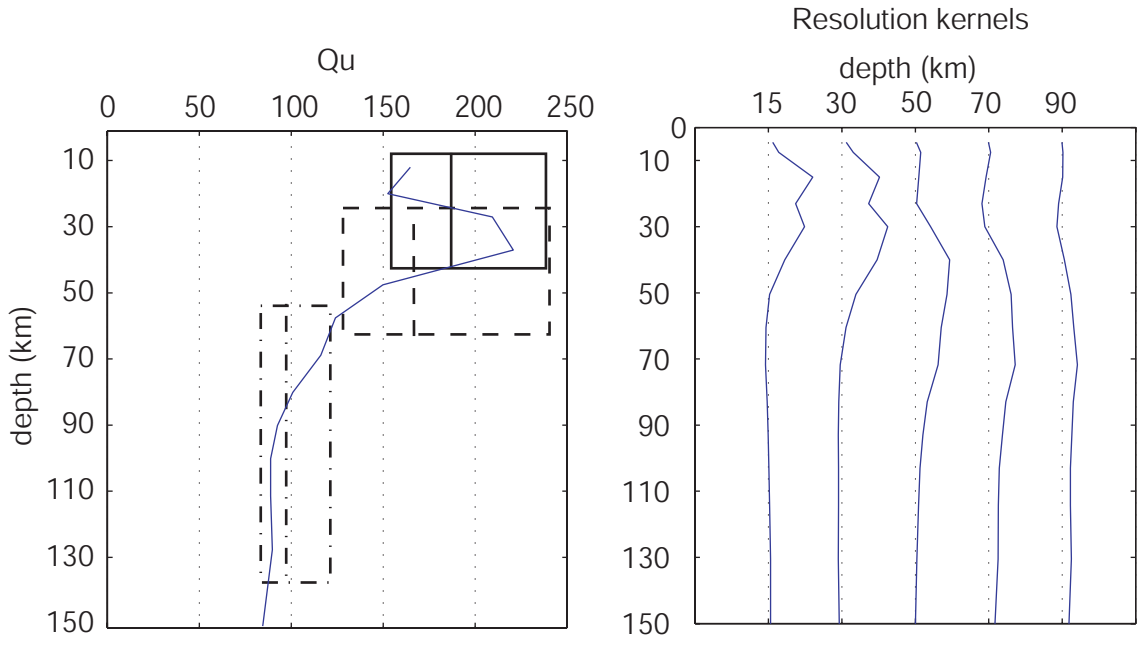


Figure 7

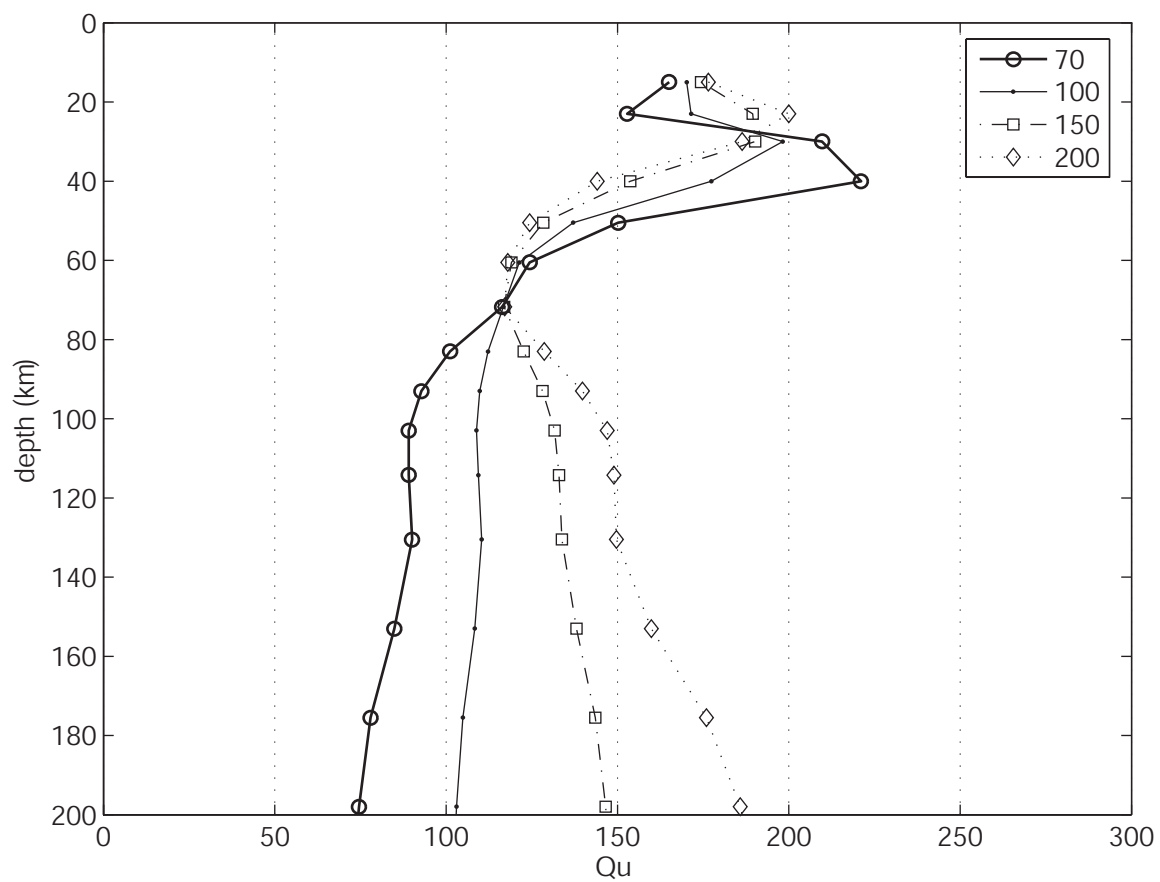


Figure 8

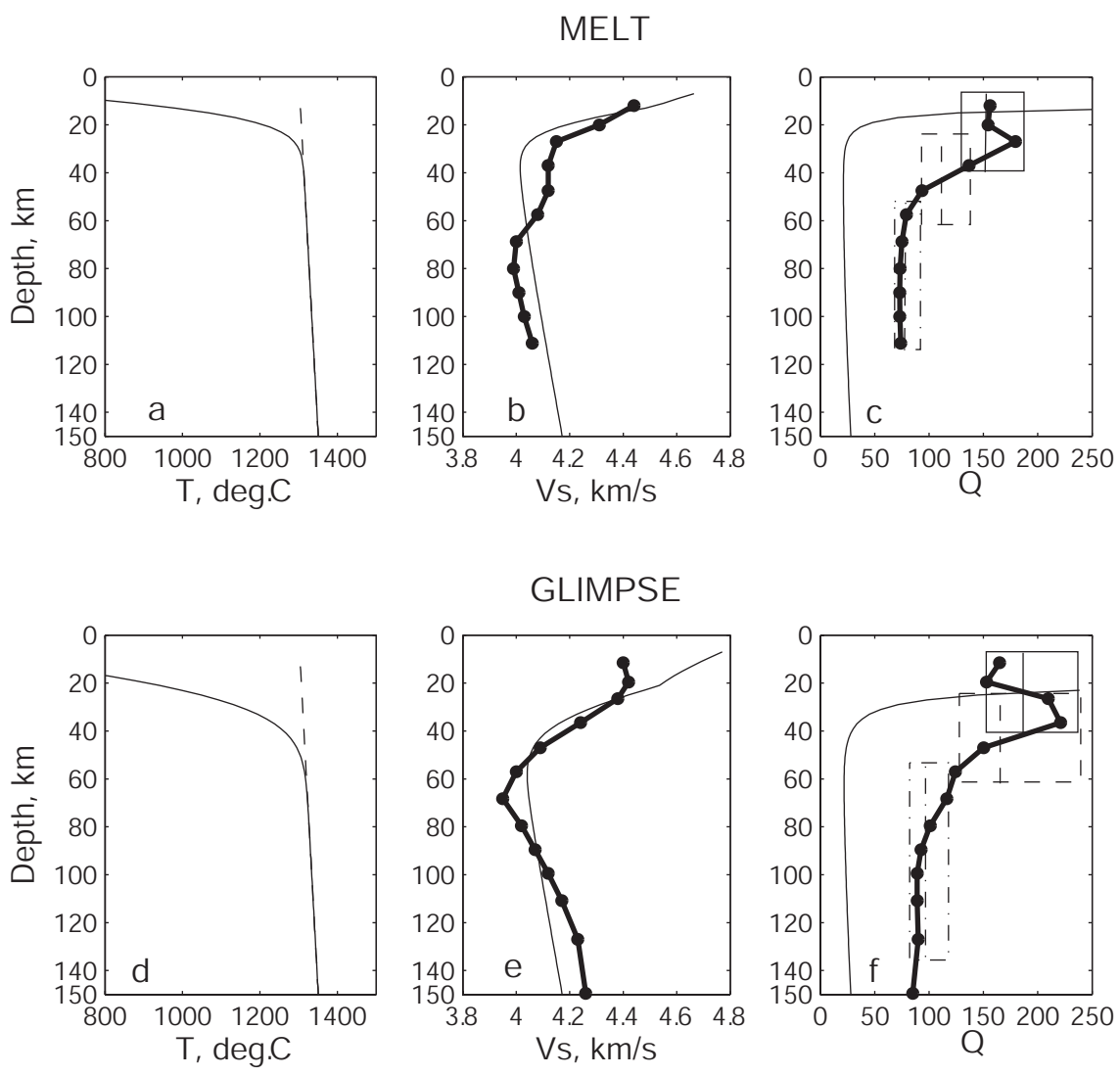


Figure 9

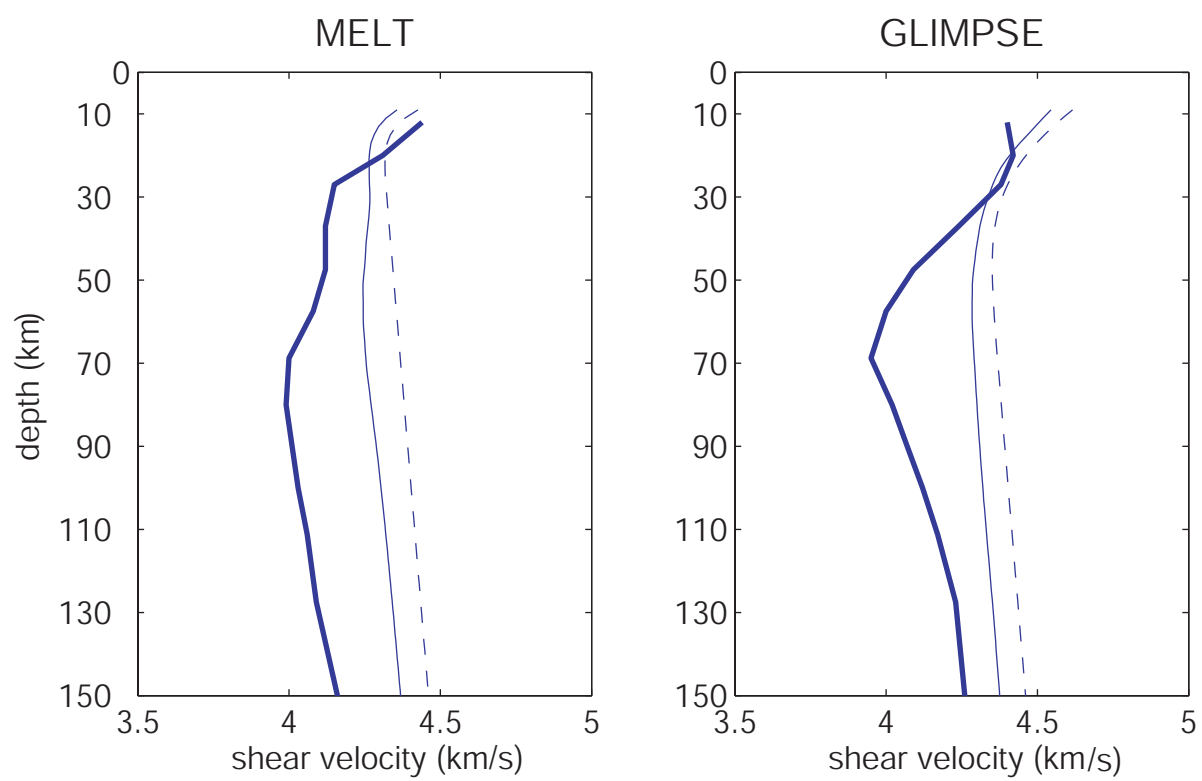


Figure 10

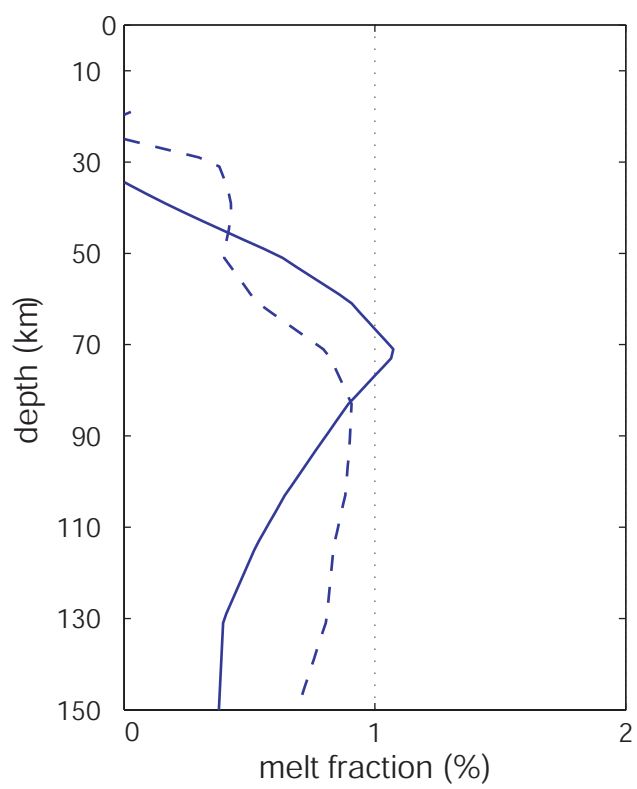


Figure 11

Appendix

Improving epicentral and magnitude estimation of earthquakes from T-phases
by considering the excitation function

Yingjie Yang, Donald W. Forsyth
Department of Geological Sciences
Brown University
Providence, RI 02912 USA

Published in BSSA, 93,2106-2122,2003

Abstract

A standard technique for locating events with T-phases is to pick the peak energy of T-phases as the arrival time, then proceed as if it was an unscattered phase originating at the epicenter. The peak energy arrival time, however, can shift to different parts of the wavetrain due to incoherent scattering. We show that a 50% reduction in variance relative to picks of peak arrival times can be achieved by fitting an assumed functional shape to the log of the entire envelope of the T-phase.

We test the stability of this approach by comparing relative event locations based on this method with those determined by cross-correlating waveforms of Rayleigh and Love surface waves recorded teleseismically using a swarm of earthquakes at the northern end of the Easter microplate as an example. Relative event locations show that there is no systematic bias in T-phase locations. The T-phase location and detection can be extended to much smaller events than are detectable by surface waves.

We estimate T-phase maximum amplitudes of about 50 events within the swarm from the amplitude of the fitted functions rather than directly from the seismograms. Twenty four of these events are large enough to estimate their magnitudes by surface wave analysis. The empirical analysis shows the log of T-phase maximum amplitude and surface wave magnitude (M_s) exhibit a relatively uniform linear relationship with much less scatter than in previously published T-phase-amplitude-versus-magnitude studies. The reduction in scatter is due to both the stability of the functional estimate of amplitude and the use of a swarm of earthquakes with similar depth, mechanism and source-receiver geometry.

The observed T-phase coda for shallow earthquakes can be synthesized using a simple model of multiple-reverberation seafloor-scattering. The results show that scattering of energy at a rough seafloor from multiple reverberations in the water column is significant in T-phase generation even where the water depths are relatively uniform.

Introduction

The T-phase is a seismically generated acoustic wave that propagates over great distance in the ocean water column (SOFAR channel) with little loss in signal strength (Tolstoy and Ewing, 1950). When seismic energy crosses the seafloor interface into the overlying water column, part of the energy is trapped in the ocean water column. According to ray theory, the transmitted acoustic energy from seismic energy propagates almost vertically due to the great velocity contrast between crust and water. Though T-phases have been observed for a long time, the coupling mechanism from almost vertical acoustic wave to horizontal T-phase is still not thoroughly understood. Two possible physical mechanisms have been proposed to explain how the energy can propagate horizontally and become trapped in the SOFAR channel. One of them is downslope conversion (Johnson et al., 1963; Talandier and Okal, 1998); acoustic energy experiences multiple reflections between the sea surface and sloping seafloor, gradually propagating more horizontally. The other is seafloor scattering (Walker et al., 1992; de Groot-Hedlin and Orcutt, 1999); seismic energy is scattered into the ocean sound channel from rough seafloor close to the epicentral region, exciting modes with dominant displacement in the

water column. This scattering process may also be represented by coupling and conversion between modes (Park et al., 2001). Although the detailed mechanism for generating the T-phase at the seafloor is not thoroughly understood, many empirical studies are still done using T-phase data to locate seismic sources or estimate source strength.

Since there is little loss in signal strength of T-phases when propagating through the water column, they can be used to detect and locate the oceanic seismicity associated with small tectonic events that cannot be sensed by land-based seismic stations (Fox et al, 1994). T-phases have been used in a large number of investigations in the field of oceanic tectonics and volcanism: monitoring activity of seafloor spreading centers at the Juan de Fuca Ridge (Fox and Radford, 1995) and at Mohns Ridge (Blackman, et al 2000); detection of submarine volcanism (Norris and Johnson, 1969; Talandier and Okal, 1987; Talandier and Okal, 1996), etc. The most basic issue in these studies is how to locate events accurately using T-phases.

One standard way to locate earthquakes using T-phases is to pick the peak energy as the arrival time of the T-phase, then proceed as if it were an unscattered and undispersed phase originating at the epicentral area despite the fact that the typical T-phase has durations of tens of seconds, growing gradually in amplitude after an unclear onset. Such an approach has been shown to have no apparent bias in epicenter location (Slack et al, 1999; Fox et al, 2000). Due to incoherent interference between waves excited or scattered from different locations, however, the peak energy arrival time can shift to different parts of the wavetrain even for stations only a few kilometers apart, forcing operator

identification of particular features in the waveform.

On December 3, 1995, three events in a swarm at the northern end of the Easter microplate were large enough to be located teleseismically (Fig.1) and catalogued in the routine earthquake bulletins of the National Earthquake Information Center (NEIC) and the International Seismological Center (ISC): an m_b 3.9 foreshock, the 4.7 mainshock and a 4.1 aftershock. Ocean-bottom seismometers (OBSs) deployed by the MELT experiment (the MELT Seismic Team, 1998) (Fig.1) recorded this swarm and these records provide us the unique opportunity to study the ability to detect and locate events using T-phases. T-phases from many other events were also detected during the experiment (Shen, 2002), but this swarm offers the best opportunity for comparing T-phase locations with those based on surface waves and teleseismic arrivals.

The purpose of this study is to develop an empirical function to fit the envelope of T-phases to better estimate their arrival time and maximum amplitude. Then, we can detect and locate events in the swarm using T-phase arrival times and analyze the relationship between T-phase maximum amplitude and earthquake size. To evaluate the reliability of T-phase locations, we compare these locations with those based on surface waves. In order to understand the T-phase excitation so that our empirical technique could be applied to a more general tectonic setting, the mechanism of T-phase excitation is discussed and a simple illustrative model is developed to synthesize the T-phase coda.

MELT OBS array

In 1995/1996, the MELT Seismic Team deployed two linear arrays of ocean-bottom seismometers across the southern East Pacific Rise to investigate magma generation beneath mid-ocean ridges (Fig.1). Each station was equipped with a three-component seismometer as well as either a hydrophone or differential pressure gauge (DPG), although not every component functioned properly at every station. These OBSs recorded continuously and thus captured the entire earthquake sequence at the northern end of the Easter microplate including the three events large enough to be reported in earthquake bulletins (Fig.1). These records show many small events large enough for T-phases and surface waves to be recorded, even though body waves (P and S) normally used in location do not stand out above the noise. There are many even smaller events only large enough to be detected by T-phases.

The vertical component records are used for analysis of T-phases instead of hydrophone data because approximately two thirds of the pressure recorders were DPGs and DPGs have poor high frequency response. Although in detail there are some differences in the waveforms of T-phases recorded simultaneously on both hydrophones and vertical seismometers, the overall character and peak energy arrivals are the same. Although the T-phases are traveling primarily horizontally, any minute pressure change in the water column at the seafloor induces some component of vertical motion.

The sampling frequency of the OBSs is 16 samples per second, limiting our study frequency to at most 8 Hz. Further distortion is introduced by analog, anti-aliasing filters;

thus we limit our T-phase analysis to 2-6 Hz, even though T-phases have been observed with higher frequencies. The OBS records are supplemented by T-phases recorded at Global Seismic Network station RPN on Easter Island (Fig.1), giving a much broader azimuthal distribution.

T-phases recorded by the OBS

A quick examination of the smoothed envelopes of T-phases from the mainshock at the northern end of the Easter microplate recorded at some of the OBSs illustrates the great variability in the waveforms, even at nearby stations (Fig. 2). One traditional way of picking arrival times is to pick the peak energy arrival. Closely spaced stations S14 and S16 (Fig.1) both have clear, narrow arrivals of peak energy, 20 to 30 seconds after the onset of the T-phase (Fig. 2). The time difference between arrival times of these peaks, however, is too great to be consistent with a single direct wave traveling to stations whose distances to the epicenter differ by less than 3 km (the stations are about 10 km apart, total epicentral distance is on the order of 650 km.). The envelopes at other closely spaced station pairs have even less resemblance (see S33 and S35 in Fig. 2). This great variability in waveform probably stems from the interference of multiple mode waves traveling from multiple points of excitation or transmission on the seafloor near the source, effectively creating signal-generated noise in the wave shape.

If the noise in the envelope shape is signal generated, then it should increase in amplitude with increasing amplitude of the signal and it should be approximately

log-normal. Figure 3 demonstrates that this is the case; for a typical station, after taking the log of the envelope, noise is approximately constant throughout the record. There is an overall gradual growth in amplitude of the envelope, followed by an even slower gradual decay. Specific peaks in amplitude of the envelope correspond to fortuitous constructive interference between waves and should not be assigned any great significance, i.e., should not be viewed as characteristic times to be picked in locating the event. When viewed in log-space, the individual peaks in amplitude appear as nothing more than minor noise fluctuations on the overall pattern of growth and decay of the envelope.

The overall pattern of growth and decay of the envelope of T-phases is probably the result of seafloor scattering. The bathymetry in the vicinity of the source locations in the swarm is rough on a small scale but is relatively uniform in depth with no more than 1 km relief between peaks and troughs of fracture zone ridges and valleys. There is no big promontory around the source location extending up into SOFAR channel that would be a dominant location for excitation of hydroacoustic energy. Hence, seismic energy scattered into the water column at the seafloor should decrease systematically with the distance of scattering points from the epicenter. The scattering points with the strongest energy lie near the epicenter and result in the maximum amplitude arrival of the T-phase envelope. However, the strongest scattering point may deviate from the epicentral point in presence of small-scale variations in bathymetry. The energy in the growth part of the T-phase comes from the scattering points that are closer to stations, because the seismic waves travel faster in the rock than acoustic waves in the water column, whereas the energy in the decay part

comes from scattering points that are farther from stations, or, as we shall see later, from scattering after multiple reverberations. Thus the arrival time of maximum amplitude should correspond to the arrival time of T-phases traveling from the epicenter to a station. The problem is how to best estimate this maximum in the presence of interference that can shift the absolute peak.

Empirical model

Our solution to the problem of identifying the peak of the envelope is to fit an empirical function to the shape of the envelope, thus utilizing the entire signal, not just a single peak. The overall, approximately linear growth and slower gradual decay of the log of the envelope suggests fitting the signal with an empirical function of exponential growth followed by decay with a different time constant. We find that the decay of the log of envelope tends to be more rapid at the beginning than later, so a simple exponential decay is not an adequate description. The envelope is thus described by background noise plus exponential growth followed by modified exponential decay with a different time constant.

The amplitude of the envelope, $A(t)$, as function of time is given by

$$t \leq t_0$$

$$A = \left[A_0^2 + A_1^2 \exp\left(\frac{-2\{t_0 - t\}}{t_b}\right) \right]^{\frac{1}{2}} \quad (1)$$

$$t > t_0$$

$$A = \left[A_0^2 + A_1^2 \exp \left\{ -2 * \left(\frac{t - t_0}{t_c} \right)^\gamma \right\} \right]^{\frac{1}{2}} \quad (2)$$

Variables:

A_0	Amplitude of Background Noise
A_1	Maximum Amplitude of Signal
t_0	Characteristic Arrival Time of Peak
t_b	Characteristic Growth Time
t_c	Characteristic Decay Time
γ	Coefficient Modifying Decay

Since both background noise and signal have random phase, we consider the amplitude of the envelope as the root mean square of these two contributors instead of adding the amplitude of noise and signal linearly.

An additional factor would have to be added for large earthquakes with long-duration sources, but the largest earthquake in this study is $m_b \sim 4.5$, for which the source duration is negligible compared to the duration of the hydroacoustic signal (Okal and Talandier, 1986).

Thus, instead of basing the pick of arrival time on a particular peak amplitude which may depend on highly variable wave interference or excitation from a single bathymetric feature, we base it on the overall shape of the signal, identifying the peak of the model shape as the arrival time after optimizing amplitudes, growth and decay times.

Evaluation of the empirical model

The least squares fitting of the function is performed on the log of the envelope so that residuals or error will be approximately normally distributed and undue emphasis will not be placed on trying to match an individual peak in amplitude caused by random, constructive interference. Figure 4 shows an example comparison of the log of model amplitude envelope and the log of observed amplitude envelope. As is demonstrated, the log of the model amplitude envelope is in good agreement with the log of observed amplitude envelope. In finding the optimum fit, i.e., inverting for the best values of the model parameters, we employ a grid search for t_0 because the shift in slope of the function at this point makes the problem highly non-linear, leading to local minima that defeat usual, simple approaches to finding the absolute minimum misfit. At each trial value of t_0 , we perform a standard, linear, iterative least squares inversion for the values of the other parameters; an approach that always converges rapidly.

One way to judge the quality of arrival time picks is to examine the variance of the travel-time residuals. Within the array, travel-times are a linear function of epicentral distance (Fig. 5) and the residuals from a linear fit are equivalent to travel-time residuals. Arrival times based on the peak of the model function yield a small reduction in variance compared to arrival time based on picking the peak energy (Fig. 6), allowing different characteristic t_b , t_c and γ for each record. The amplitude (A_1) tends to decrease somewhat with increasing epicentral distance (Fig. 7a), but it has no apparent variation with azimuth

or depth of receivers and the scatter due to local site and instrument responses dominates the variance over the relatively small distance and depth ranges in this experiment. More importantly, for the purposes of event location, the overall shape of the envelope is nearly constant. Note, for example, the overall similarity between the envelope for station S30, the deepest and one of the most distant stations, and that for S50, one of the shallowest and closest (Fig. 2). No systematic variation of t_b , t_c or γ with epicentral distance or water depth of the receiver is found (Fig. 7), thus the overall shape may be regarded as a characteristic of excitation in the source region, little modified by propagation, at least in the distance range represented in this experiment. Because there is no systematic trend and there is trade-off or covariance in the inversion between arrival time and growth time, decay time and decay coefficient, we try fixing the growth (t_b), decay time (t_c) and decay coefficient (γ) to the average value of all the seismograms.

We note that the tradeoff between decay time and decay coefficient is particularly large, thus in the inversion we first fix γ to the average value for all the seismograms, then invert to get the average values for all the seismograms of t_b and t_c , and finally fix all three parameters. Eliminating the trade-off in arrival time with other factors by fixing the shape in this way yields a dramatic reduction in variance of about 50% compared to picking the peak arrival time (Fig. 6). Clearly, fitting a functional form to the envelope yields much more stable arrival time picks, which should significantly improve estimates of epicentral location based on T-phases.

This reduction in variance of the travel time residual and the lack of systematic

dependence on epicentral distance, sensor azimuth or sensor depth indicates that the shape is principally generated at or near the source during excitation.. The variations of t_b and t_c from the average may indicate the shape is somewhat modified due to local scattering and propagation effects in the vicinity of the stations. We notice no significant variation in shape of the envelope for different frequency bands and the shape at island station RPN is indistinguishable from the OBS population, indicating that the excitation time function is nearly independent of mode.

Further improvement would be possible if the variability in waveforms at individual stations could be predicted. The potential for improvement can be demonstrated by a comparative or relative event study of closed spaced events. Here we describe results from the mainshock and two of the aftershocks in the earthquake sequence at the northern end of the Easter microplate. Using the fixed-shape approach to picking arrival times, we find arrival times for each event. In addition to picking times at the ocean-bottom seismometer stations, we also pick arrivals at GSN station RPN, which is a similar distance away to the southeast (Fig. 1). RPN lies in the middle of Easter Island about 5 to 10 km from the shore, so there must be conversion from acoustic waves to seismic waves at the sloping seafloor off the northwest shore (Talandier and Okal,1998). In this study, however, we employ a relative location technique and only need to obtain the arrival time relative to the mainshock. Since the events within this swarm are very close to each other, the station correction or delay at RPN is common to all events and can be ignored. Taking the time difference between different events at the same station, we find differential times that are

used to find relative event locations of the aftershocks relative to the mainshock. For T-phase velocity, we assume it is equal along all the paths from epicenter to stations, a reasonable assumption, since, in this entire study region, the water depth is relatively uniform and the variations of water temperature, pressure and salinity are slight. We estimate the T-phase velocity from the slope of the travel time-versus-distance regression of T-phases.

The variance from residuals of the relative event locations is much smaller than the travel time residuals for a single event (Fig. 6), indicating that there are systematic variations in waveform that are characteristic of particular stations and paths. Since the overall paths for closely-spaced station pairs are similar, yet the envelopes can be significantly different, most of these differences must arise near the receivers. Although our approach of fitting functional forms to the envelope is very different, the variance we find in this way is similar to that found by Shen (2002) in relative event locations accomplished by cross-correlating the observed envelopes of T-phases.

Comparison between T-phase and surface wave relative locations

Using the fixed-shape approach and the relative location techniques stated above, we locate the 10 largest events within the swarm (Table 1.). Figure 8 shows a plot of the 95% confidence ellipses for the locations relative to the mainshock. The T-phase epicenters of these events form two clusters about 25 km apart (Fig. 8a) that appear to be located on two

transform faults striking about N80°E (Forsyth et al., 2003)..

This separation is larger than would normally be expected for a swarm on a mid-ocean ridge, calling into question the reliability of these locations. To test the precision of location, we have also performed relative event locations of these events using Rayleigh and Love waves observed at teleseismic stations. We simply cross-correlate the waveforms of the reference event, chosen to be the largest event, with the waveforms of other events to find relative arrival times. In the frequency band we employ, 0.02 to 0.05Hz, and for the separation between events of this swarm, dispersion effects can be neglected. We employ phase velocities for young seafloor from Nishimura and Forsyth (1989) as the characteristic velocity in the source region for the calculation of locations. Waveforms from different events in the sequence are very similar (Fig. 9), indicating that the mechanisms and depths are similar. There is a good azimuthal distribution of stations (Fig. 10) with adequate signal-to-noise ratio, yielding very precise relative locations.

The surface wave relative locations of these 10 events (Table 1.) also show two clusters of events separated to the same extent (Fig. 8b). The two clusters based on T-phases and surface waves are in agreement with the strike and separation of the Anakena and Raraku transform faults mapped with long-range, side-scan sonar (Rusby and Searle, 1995) and satellite altimetry (Smith and Sandwell, 1997).

Comparing the 95% confidence intervals, we note the location uncertainty based on T-phases is greater than that based on surface waves, because the surface wave records have a good azimuthal distribution of stations, at least one station in each azimuthal

quadrant, whereas almost all the OBSs are concentrated in a single azimuthal quadrant and only one station, RPN, lies in the southern quadrants.

We also note the 95% confidence intervals of the events based on T-phases and surface waves do not completely overlap. However, there is no systematic bias between T-phase locations and surface wave locations and the differences between them are relatively small, about only 8 km on average. The differences in location relative to the surface wave epicenters may partly be a result of station geometry, with the great importance of RPN due to lack of redundancy to the south making locations sensitive to noise at this single station, and partly due to details of bathymetry at the source locations, which cause differences in location of the most efficient transfer of acoustic energy into the sound channel (Dziak et al, 1997). If locations were based on the peak energy arrivals rather than the peak of the fitted function, the primary effect is to greatly increase the size of the confidence regions. Because the locations based on T-phases using our method have no systematic bias, this approach should be especially useful to detect and locate small events that are not detected by other means.

A comparison between T-phase maximum amplitude and earthquake magnitude

Some prior studies have empirically related the peak amplitude of T-phases to earthquake magnitude (Johnson and Northrop, 1966), the mean T-wave spectral amplitude (in db) to seismic moment (Walker et al, 1992) and T-phase source power level to

earthquake magnitude and seismic moment (Dziak et al, 1997; Fox et al., 2001; Dziak, 2001). These studies all found a very large scatter in observed T-phase amplitude. The efficiency of transformation from seismic energy to T-phase energy is strongly influenced by the source geometry. If linear propagation processes were assumed, the strength of the T-phase would be proportional to earthquake magnitude for similar sources with similar geometries (Johnson and Northrop, 1966). These earlier studies were handicapped by using a variety of different earthquakes in different locations with different paths and by using only reported magnitudes, thus perhaps obscuring the relationship between earthquake size and T-phase excitation.

The events within the swarm have similar source locations and similar focal mechanisms based on the radiation patterns of Rayleigh and Love waves (Forsyth et al. 2003). Though the source depth cannot be obtained directly, it is reasonable to assume the depth variation of events within the swarm is relatively small since the surface waveforms of these events are similar and the earthquakes occur on relatively short transforms on a fast-spreading ridge where the lithosphere should be quite thin. Thus, the swarm provides us sources that have similar source parameters except for magnitude.

In this study area (Fig. 1) the seawater depth is almost uniform, thus energy loss due to bathymetric obstruction along propagation paths from sources to the OBS is negligible. The attenuation of T-phases by absorption in seawater is very small at the low frequencies (<30 Hz), only about 0.25 db per 500 km for a 10 Hz acoustic wave in 10°C seawater (Dziak, 2001). Considering that the greatest epicentral distance is less than 900 km,

attenuation by absorption in the water column is negligible. The rate of decay of amplitude with distance (Fig. 7a) is greater than expected for geometrical spreading alone, suggesting some energy loss due to interaction with the seafloor for these phases that are recorded at the ocean bottom, but because epicentral distance to individual stations is nearly constant within the swarm, no bias between events is introduced by correcting only for geometrical spreading. We can assume the T-phase maximum amplitude variation for different events is only the result of the earthquake size difference of these similar sources.

In order to reduce the possible error and increase the signal-to-noise ratio, records from a number of stations are stacked to obtain an estimate of the T-phase maximum amplitude of each event. The T-phases are too high frequency and unpredictable to stack directly. We shift the fixed-shape-model from the mainshock along a time span including the entire earthquake sequence solving for A_1 at each possible value of t_0 . This yields a time series of A_1 values for each station, which are then summed according to their distance to the mainshock using the cylindrical spreading model. After this process, events stand out more clearly above the background noise. Figure 11 clearly exhibits a number of different amplitude events; there are more than 50 events detected in this swarm using this method, whereas using surface waves only about 24 events are detected at RPN or at the quietest OBSs. Here, to empirically analyze the relationship between the T-phase maximum amplitude and earthquake size, we only need care about the amplitudes relative to the mainshock rather than absolute values. Surface wave magnitude (M_s) is chosen to represent earthquake size because it is directly proportional to the log of seismic moment

for earthquakes of the magnitude found in this swarm. M_s was estimated from cross-correlating the surface waves at a common set of low-noise, Global Seismic Network stations down to a threshold of $M_s = 3.5$. For $2.5 \leq M_s \leq 3.5$, magnitudes were estimated by cross-correlating long-period waveforms at the single, nearby station RPN.

The log of the T-phase amplitude is linearly related to M_s in the magnitude range of this study (Fig. 12). The scattering from this linear fit is much smaller than in the prior studies (Johnson and Northrop, 1966; Walker et al., 1992; Dziak et al., 1997), because the mechanisms and depths are most probably similar, the paths are nearly constant, the T-phase amplitude estimated from fitting a function to the entire waveform is more stable than peak amplitudes, and surface wave magnitude estimated from cross-correlating waveforms at common stations is less variable. Reduced scatter in T-phase-amplitude-vs-magnitude has also been reported for nuclear tests at Mururoa atoll that share a common source location (Smith, 1987) and for the mainshock and aftershock sequence in the Bhuj area with T-phases recorded by a hydroacoustic array in the Indian Ocean (Pulli and Upton, 2002). The slope of M_s vs. $\log(A_1)$ is very close to 2. For the ω -square source model (Aki, 1967, 1972), the corner frequency for displacement spectra is expected to lie between 4 Hz and 0.05 Hz, the typical frequencies of the T-phase and surface waves, respectively, for magnitudes M_s between 2 and 5. If 0.05 Hz is small compared to the corner frequency and 4 Hz is large, then the slope should approach 3. For magnitudes much below 2, where the corner frequency is much larger than 4 Hz, the slope should return to 1. The fact that the slope is 2 rather than 3 suggests perhaps that these

earthquakes lack geometrical self-similarity. Instead of the width of the earthquake rupture zone increasing in proportion to length as in the usual source model, perhaps for these events on transform faults on a fast-spreading ridge, the earthquake width is limited by the thermal state of lithosphere so that the sources are essentially linear ruptures with nearly constant width.

Extrapolating the linear magnitude scale to events that are too small to detect surface waves, we find that we detect many events with M_s about 2 and can clearly identify some events with magnitude as small as 1.5 during periods when they are not obscured by other events of larger magnitude.

T-phase Excitation

To apply the empirical techniques employed for T-phases in this paper to a more general tectonic setting or to predict the variations in shape of the envelope that are observed at different stations requires an understanding of the mechanism of T-phase excitation. Existing models for T-phase excitation are not adequate. The basic problem is that for a flat seafloor, the transmitted acoustic energy converted from seismic energy at the seafloor interface propagates almost vertically in the water column due to the great velocity contrast between crust and water. To convert the energy to a horizontally traveling wave requires some sort of scattering at an irregular interface. Conversion and coupling between normal modes excited by an earthquake can, in principle, provide a complete description of the process (Park et al., 2001) but may be too computationally cumbersome for routine

application. Similarly, numerical approaches such as finite difference, finite element, and boundary element methods provide insight into the physics of the process, but are too computationally intensive for routine application to realistic, three-dimensional geometries.

Relatively simple conceptual models for the conversion process include downslope conversion, where multiple reflections between the sea surface and the sloping seafloor deflect the rays horizontally (Johnson et al., 1963; Talandier and Okal, 1998); and single scattering from a rough seafloor (Walker et al., 1992; de Groot-Hedlin and Orcutt, 1999; de Groot-Hedlin and Orcutt, 2001). In our particular case, the seafloor is rough, nearly unsedimented basalt, as confirmed by high reflectivity on side-scan sonar (Searle et al., 1989), but the overall topographic relief is limited. The events in the swarm occurred on the Anakena and Rarakuku transforms between the East Pacific Rise and the west rift of the Easter microplate (Forsyth et al., 2003), a region mapped with long-range, side-scan sonar (Rusby and Searle, 1995) and satellite altimetry (Smith and Sandwell, 1997). It is unlikely that T-phase excitation is dominated by downslope conversion, because total relief in the area between the deepest fracture zone troughs and the shallowest parts of the fracture zone ridges is only about 1200m and the envelopes have approximately the same shape for the northern and southern groups of epicenters at both the OBSs to the north and station RPN to the south.

A very promising, simple approach to excitation was developed by de Groot-Hedlin and Orcutt (1999). In their model, P-wave energy from an earthquake spreads spherically

in the solid earth until it encounters the rough seafloor. Each point on the seafloor then acts as a radiator or pressure source, exciting T-phase normal modes in proportion to the product of the P-wave amplitude at that point and the relative displacement of the normal modes at that depth. In their examples, a long-duration, T-phase envelope was predicted for sources at depths of several tens of kilometers, because the P energy spread out over a large area, encountering shallow seafloor within the SOFAR channel along the arc-trench slope over an extended distance from the receivers. Applied to our tectonic setting of shallow earthquakes in a relatively flat but rough seafloor, however, their single-scattering approach fails.

The primary problems with their single-scattering model are that it neglects the fact that only a small fraction of the energy first entering the water column is converted to horizontally traveling modes at the seafloor and it predicts that the duration of the excitation, due to spreading out of the area of the insonification of the seafloor by P-waves, should be proportional to earthquake depth for a sub-seafloor source. In our case, the events are unlikely to be any deeper than 6 km, and are more likely within the crust, because they are located on short-offset transforms on a fast spreading center and they excite short-period Love waves (3-5 s) that are guided within the crust (Dunn and Forsyth, 2003). As we will show later in more detail, single scattering of P-waves from a shallow source beneath flat, rough seafloor would produce a short, symmetric T-phase with little resemblance to the observed, long-duration, asymmetric phases generated by the earthquakes in this study. The energy in the water column that does not travel horizontally

will reflect at the sea surface and re-encounter the seafloor, where it will be rescattered.

Another limitation of the de Groot-Hedlin/Ocrutt model is that it neglects S-wave excitation of T-phases. The conversion from S wave to T-phase has been observed in the vicinity of downgoing slabs (Okal and Talandier, 1997; Lin, 2001) and these studies suggest that in these particular settings S-wave conversion dominates over P-wave conversion. In general, for shallow sources where there is little distance in which the S-wave can be attenuated, S-wave excitation should be dominant. Far-field displacements for earthquake waves are proportional to $1/v^3$, where v is the P or S velocity, so for a Poisson's ratio of 0.25, S-wave would carry roughly 15.6 times the energy of P-wave. For vertically incident waves on a flat, smooth interface, of course there is no conversion of S-waves to acoustic energy in the water column, but at large incidence angles where more of the energy leaves the source (because the surface area where rays leave the focal sphere in any small range of incidence angle is proportional to the sine of the angle of incidence), the conversion of S-wave energy to transmitted acoustic energy can be more efficient than the transmission of P-wave energy (Fig. 13a). In the frequency band of the T-phases, S-waves from microearthquakes recorded locally on OBSs or hydrophones typically have much larger amplitude than P-waves.

In the following sections, we develop a very simple model to illustrate the importance of multiple reverberations and S-waves in generating the T-phase. We adopt the philosophy of de Groot-Hedlin and Ocrutt of treating the seafloor as an ensemble of scattering points that excite acoustic modes, but follow the energy in the acoustic waves converted from

both P and S waves as it reflects back to the seafloor at the sea surface after the initial conversion. The model is illustrative only; it will require further development for general application to real topography, which would then automatically include effects such as downslope conversion.

Multiple-reverberation seafloor-scattering

In our model, we represent the seafloor in the source area as a flat, rough plane separating a uniform half-space from an overlying seawater layer. Figure 14 illustrates the basic idea for this model. Since the seafloor is rough, a small portion of the transmitted acoustic energy is scattered into horizontally propagating T-phases when seismic energy crosses the seafloor interface. In this simple model, most of the acoustic energy continues to propagate nearly vertically towards the sea surface along the ray path expected for a flat, smooth interface. This part of the energy is reflected totally at the sea surface back to the seafloor. Then it is scattered and reflected again. This same process continues and the acoustic waves experience multiple reverberations. Each time the acoustic wave is incident at the seafloor, part of the acoustic energy converts back to seismic energy and is transmitted out of the system into the lower medium, a small fraction is scattered into horizontally propagating T-phases and the rest is reflected back into the water column at steeper angles. The scattered, horizontally propagating T-phase energy spreads out cylindrically from different scattering points that behave like second sources and form the observed T-phase waveform.

We recognize that there is a continuum of intensity of scattered energy as a function of angle from horizontal (Fig. 14b,c), but our arbitrary partitioning into horizontally scattered energy and energy that propagates along the ray path expected for a flat seafloor provides a reasonable, first approximation to illustrate the significance of multiple reverberations in the excitation of T-phases.

Numerical simulation

In generating a synthetic excitation function for the T phase, we take the source focal mechanism into account assuming a double-couple source. We assume spherical spreading for the seismic wave within the crust and employ a ray tracing technique by dividing the spherical wave into a number of ray bundles with the same solid angle. Thus the energy of each ray bundle is only dependent on propagation orientation and can be determined using the formula of double-couple energy radiation pattern (eqn. 4-87, Aki and Richards, 1980).

Since both P and S waves can transform to acoustic waves when crossing the seafloor, we need take into account the energy ratio of the P wave to the S wave and the difference in radiation pattern of the two phases. We first calculate the energy envelope of the T-phase converted from the P wave and S wave separately and then sum them together to form the predicted T-phase envelope. To compute the T-phase envelope shape, we need care only about relative value of the energy; the exact value only changes the amplitude and has no effect on the shape.

The body wave (P and S wave) attenuation due to absorption within the crust is

negligible since the source is very shallow and the propagation path of body wave within the crust is quite short. For a deep source, this attenuation energy loss should be subtracted from the energy of each ray.

The first step in computing the T-phase excitation is to calculate the energy transmission coefficient from seismic wave to acoustic wave at the seafloor interface and the energy reflection coefficient when acoustic wave is incident on the seafloor. We use the Ergin (1950) method to calculate these two coefficients. The presence of a thin veneer of sediment or slow layer 2A at the top of the crust may alter the details, particularly at high frequencies, but is neglected here. Figure 13a illustrates the transmission coefficient variation with incidence angle for a P wave and a SV wave incident at the seafloor against the seawater. The transmission coefficient of the P wave simply decreases with increasing incidence angle, whereas that of the SV wave is complex: first the value increases from zero to a local maximum before suddenly decreasing to zero at the critical angle for S-to-P reflection, after that, the value increases rapidly to a maximum and gradually decreases to zero at grazing incidence. Figure 13b shows the reflection coefficient of the acoustic wave at the seafloor. The value is almost constant when the incidence angle is smaller than the critical angle for the transmitted P wave. When the incidence angle is greater than the critical angle for the transmitted SV wave, the reflection coefficient is one and all acoustic energy is reflected back. At the free sea surface, we assume all acoustic energy is reflected.

Thus, having the transmission and reflection coefficients and Snell's law, we can follow each ray trajectory in three dimensions and know the energy partition for each ray

when it encounters the interface.

When the seismic waves cross the rough seafloor or the acoustic wave is incident on the seafloor, we assume a small, constant fraction (one percent) of the acoustic energy is scattered to T-phase energy. This constancy of conversion, independent of angle slope of seafloor or direction to the receiver, is equivalent to de Groot-Hedlin and Orcutt's assumption that each scattering point can be regarded as a secondary pressure source that excites acoustic T-phase modes in simple proportion to the amplitude of the incoming waves. The relative excitation of different modes is dependent on the depth of the secondary source. If the seafloor is flat, the excitation value for each mode will be the same for all points and the ratio of scattered T-phase energy to incoming acoustic wave energy is constant. A small arbitrary conversion value is used in the calculation for T-phase shape, since the exact excitation value only changes the amplitude of T-phase, not the shape, provided the fraction of energy converted to T-phase is small compared to the fraction lost by transmission. Scattering into T-phase energy may be less efficient for the initial encounter of seismic energy with the seafloor than for subsequent reverberated energy, because the rescattering of singly scattered energy produces a more nearly isotropic energy distribution (Fig. 14b,c) and because the pressure variations at the seafloor are greater for the reflected phases, which are the sum of the downgoing and upgoing reflected waves. To take these effects into account in an approximate manner, we halve the conversion coefficient at the first encounter with the seafloor.

For each ray bundle, the T-phase energy is generated at multiple scattering points at

different times corresponding to each time the ray crosses the seafloor or is incident on the seafloor. The T-phase energy that would be observed at a receiver from each scattering point is given by the product of acoustic energy remaining in the bundle and the constant conversion value, divided by the distance from the scattering point to a receiver (geometrical spreading correction). The travel time for scattered T-phase energy is the sum of three parts: the seismic travel time within the crust, the acoustic travel time within the water column and the T-phase travel time from scattering point to receiver. To form the amplitude envelope for the T-phase, we sum the T-phase energy within 0.1 second bins according to the energy intensity of each bundle arriving in that interval.

Synthetic Envelopes

In our first example, we do not consider source focal mechanism or ray reverberation and only the P wave is included, corresponding to the de Groot-Hedlin and Orcutt (1999) equivalent model for a flat seafloor. In Figure 15a, the heavy line shows the computed T-phase envelope for this case. The duration of the envelope is relatively short and the shape is symmetric about the peak energy. The short duration is the result of shallow source depth, since the shallow source excites only a small scattering area in the epicentral region. The symmetry is due to the flat seafloor and great epicentral distance. Since the scattering seafloor is flat and scattering is assumed to be omni-directional, the predicted T-phase energy from each scattering point is symmetric about the epicenter. Thus, given the great epicentral distance of receivers relative to scattering area dimension, the distribution of

distances from scattering points to receiver is symmetric and a nearly symmetric shape is predicted. This computation suggests the seafloor single scattering model for a very shallow source cannot accurately predict the observed, asymmetric, long-duration T-phase envelope.

If we take reverberations into account, the predicted signal broadens and becomes more asymmetric. Even if only one reverberation (Fig.15a) is considered in computing the T-phase energy envelope, the difference is obvious. When taking all the reverberations into account, the T-phase envelope has much more energy in the coda and it decays much more gradually compared to the no reverberation case. Since acoustic rays experience multiple reverberations in the water column before scattering at the near horizontal angles that can generate T-phases, a lot of the scattered T-phase energy arrives later and leads to slower decay.

Figure 15b shows the T-phase shapes converted from the P and S waves for a strike-slip source with 6 km source depth. It shows that the T-phase has much more energy converted from the S wave than the P wave. Figure 15c demonstrates the change of T-phase envelope shape with the source depth. As is shown, the deeper the source, the broader the computed T-phase shape, although most of the broadening takes place in the growth phase; the decay governed by reverberations changes little. Schreiner et al. (1995) report changes in rise time of the wave packet that they attribute to changes in source depth in an earthquake swarm associated with a dike injection. Changing the water depth or transmission loss through the seafloor will affect primarily the rate of decay of the envelope.

Figure 15d shows the comparison of an observed T-phase envelope and a predicted envelope computed for a strike-slip source with 3 km water depth, 6 km focal depth, both P-wave and S-wave conversion and all reverberations. The rapid growth, slower gradual decay and overall duration of the T-phase envelope are accurately predicted by our model. In the later parts of the coda, the real envelope decays more slowly than our model. This difference is probably due to our arbitrary division of energy into undisturbed and horizontally scattered components. With a continuum of scattering angles, some of the reverberating energy will be incident on the seafloor beyond the critical angle for SV transmission, thus reducing transmission loss and decreasing the decay rate.

The main task of our study is not to synthesize the exact shape of the T-phase envelope. Instead, the purpose of this section is to show the significant role of multiple reverberation scattering in excitation of T-phases. We propose a possible physical model that predicts waveforms in good agreement with the observed waveforms and the empirical function we employed to describe the growth and decay of T-phase energy. In some more heavily sedimented areas, multiple reverberations may be less important as the velocity contrast at the seafloor will be reduced and attenuation within the sediment column increased. In these areas, a more symmetric excitation function would be expected (deGroot-Hedlin and Orcutt, 2001).

Our simple model could be improved by 1) incorporating real topographic relief and depth dependent excitation of T-phase normal modes, 2) adding more realistic crustal structure that would modify the initial ray paths and the reflection and transmission

coefficients, and 3) employing a more realistic, continuous scattering function that depends on the local seafloor roughness.

Summary

T-phases can be recorded on oceanic bottom seismometers and used to detect and locate small events. In a source region with relatively flat seafloor, the waveforms of T-phases are primarily governed by the source depth, water depth, and multiple reverberations in the water column in the vicinity of the source. Subsequent propagation and receiver local scattering only have second order influence on the shape of the T-phase envelope.

Fitting a functional shape to the log of the envelope of the T-phases greatly improves the picking of the arrival times compared to simply picking the time of peak energy. In addition, this approach uses the entire signal and is less likely to be influenced by individual bathymetric features affecting the excitation of the hydroacoustic phase. Relative event locations of a foreshock/aftershock sequence using surface waves confirm that there is no apparent bias in relative locations based on T-phase, at least in our example with relatively limited bathymetric relief.

By fitting a functional shape to the log of the envelope of the T-phases, the T-phase peak amplitude of ocean events can be estimated more accurately. The detectable threshold is smaller for T-phases than for surface waves. More than 50 events within a swarm of events on the Easter microplate can be detected using T-phases, whereas only 24 events are

detected with surface waves. We find that there is a linear relationship between the log of T-phase amplitude and surface wave amplitude (M_s) for events from the swarm ranging in size from M_s 2.5 to 4.8, indicating that T-phase amplitude can provide a reasonable estimate of earthquake magnitude and seismic moment of oceanic earthquakes. It can be used to estimate earthquake size and seismic moment of small oceanic events that are detectable only with T-phases.

Using a multiple-reverberation seafloor-scattering model, the T-phase envelope for a relatively shallow event beneath a flat seafloor can be computed. The character of the T-phase shape, rapid growth followed by gradual decay, is predicted correctly. Multiple reverberation scattering plays an important role in T-phase generation and should be considered in excitation of T-phases.

Acknowledgments

The comments of Catherine deGroot-Hedlin, Emile Okal and Jose Pujol were helpful in improving the manuscript. The initial data acquisition was supported by the RIDGE program of the National Science Foundation. We thank the OBS groups and the captain and crew of the R/V Melville for their contributions to gathering the data. This work was supported by Defense Threat Reduction Agency contract DTRA01-00-C-0071.

References

Aki, K., and P. G. Richards (1980). *Quantitative seismology: theory and methods*, Freeman, New York, Vol. 1, 77-84.

- Aki, K. (1972). Scaling law of earthquake source time-function, *Geophys. J. MNRAS* **31**,3-25.
- Aki, K. (1967). Scaling law of seismic spectrum, *J. Geophys. Res.* **72**, 1217-1231.
- Blackman, D. K., C. E. Nishimura, and J. A. Orcutt (2000). Seismoacoustic recordings of a spreading episode on the Mohns Ridge, *J. Geophys. Res.* **105**, 10,961-10,973.
- de Groot-Hedlin, C. D., and J. A. Orcutt (1999). Synthesis of earthquake-generated T-waves, *Geophys. Res. Lett.* **26**, 1227-1230.
- de Groot-Hedlin, C. D., and J. A. Orcutt (2001). Excitation of T-phases by seafloor scattering, *J. Acoust. Soc. Am.* **109**, 1944-1954.
- Dunn, R., and D. W. Forsyth (2003). Short-period Love wave reveals the transition from broad mantle upwelling to the narrow crustal magmatic system beneath the southern East Pacific Rise, submitted to *J. Geophys. Res.*.
- Dziak, R. P. (2001). Empirical relationship of T-wave energy and fault parameters of northeast Pacific Ocean earthquakes, *Geophys. Res. Lett.* **28**, 2537-2540.
- Dziak, R. P., C. G. Fox, H. Matsumoto, and A.E. Schreiner (1997). The April 1992 Cape Mendocino earthquake sequence: seismo-acoustic analysis utilizing fixed hydrophone arrays, *Mar. Geophys. Res.* **19**, 137-162.
- Ergin K. (1952). Energy ratio of the seismic waves reflected and refracted at a rock-water boundary, *Bull. Seism. Soc. Am.* **42**, 349-372.
- Forsyth, D. W., Y. Yang, M. D. Mangriotis, and Y. Shen (2003). Coupled seismic slip on adjacent oceanic transform faults, *Geophys. Res. Lett.* in press..

- Fox C.G., H. Matsumoto, and T. A. Lau (2001). Monitoring Pacific Ocean seismicity from an autonomous hydrophone array, *J. Geophys. Res.* **106**, 4183-4206.
- Fox, C. G., and W. E. Radford (1995). Acoustic detection of a seafloor spreading episode on the Juan de Fuca Ridge using military hydrophone arrays, *Geophys. Res. Lett.* **22**, 131-134.
- Fox, C. G., R. P. Dziak, H. Matsumoto, and A. E. Schreiner (1994). The potential for monitoring low-level seismicity on the Juan de Fuca Ridge using military hydrophone arrays, *Mar. Tech. Soc. J.* **27**, 22-30.
- Johnson, R. H., J. Northrup, and R. Eppley (1963). Sources of Pacific T-phases, *J. Geophys. Res.* **68**, 4251-4260.
- Johnson, R. H., and J. Northrop (1966). A comparison of earthquake magnitude with T-phase strength, *Bull. Seism. Soc. Am.* **56**, 119-124.
- Lin C. (2001). T-wave excited by S-waves and oscillated within the ocean above the southeastern Taiwan forearc, *Geophys. Res. Lett.* **28**, 3297-3300.
- MELT Seismic Team (1998). Imaging the deep seismic structure beneath a mid-ocean ridge: The MELT Experiment, *Science* **280**, 1215-1218.
- Nishimura, C.E., and D.W. Forsyth (1989). The anisotropic structure of the upper mantle in the Pacific, *Geophys. J.* **96**, 203-229.
- Norris, R.A., and R.H. Johnson (1969). Submarine volcanic eruptions recently located in the Pacific by sofar hydrophones, *J. Geophys. Res.* **74**, 650-664.

- Okal, E. A., and J. Talandier (1997). T waves from the great 1994 Bolivian deep earthquake in relation to channeling of S wave energy up the slab, *J. Geophys. Res.* **102**, 27,421-27,437.
- Okal, E. A., and J. Talandier (1986). T-wave duration, magnitudes and seismic moment of an earthquake—application to Tsunami warning, *J. Phys. Earth* **34**, 19-42.
- Park, M., and R. I. Odom (2001). Modal scattering: a key to understanding oceanic T-waves, *Geophys. Res. Lett.* **28**, 3401-3404.
- Pulli, J. J. and Z. M. Upton (2002). Hydroacoustic observations of Indian earthquake provide new data on T-waves, *Eos Trans, AGU* **83**,145,150,151.
- Rusby, R. I., and R. C. Searle (1995). A history of the Easter microplate, 5.25 Ma to present, *J. Geophys. Res.* **100**, 12,617-12,649.
- Schreiner, A. E., C. G. Fox, and R. P. Dziak (1995). Spectra and magnitudes of T-waves from the 1993 earthquake swarm on the Juan de Fuca Ridge, *Geophys. Res. Lett.* **22**, 139-142.
- Searle, R. C., R. I. Rusby, J. Engeln, R. N. Hey, J. Zekin, P. M. Hunter, T. P. LeBas, H. J. Hoffman, and R. Livermore (1989). Comprehensive sonar imaging of the Easter microplate, *Nature* **341**, 701-705.
- Shen, Y (2002). Seismicity at the southern East Pacific Rise from recordings of an ocean bottom seismometer array, *J. Geophys. Res.* **107(B12)**, 2368, doi:10.1029/2001JB001742.

- Slack P. D., C. G. Fox, and R. P. Dziak (1999). P wave detection thresholds, Pn velocity estimates, and T wave location uncertainty from oceanic hydrophones, *J. Geophys. Res.* **104**, 13,061-13,072.
- Smith, W. D. (1987). Underground nuclear explosions recorded in Rarotonga: estimation of m_b from T-phase amplitude, *Geophys. J. R. Astr. Soc.* **90**, 35-42.
- Smith, W. H., and D. T. Sandwell (1977). Global seafloor topography from satellite altimetry and ship depth soundings, *Science* **277**, 1956-1962.
- Talandier, J., and E. A. Okal (1996). Monochromatic T waves from underwater volcanoes in the Pacific Ocean: Ringing witnesses to geyser process? , *Bull. Seism. Soc. Am.* **86**,1529-1544.
- Talandier, J., and E. A. Okal (1987). Seismic detection of underwater volcanism: The example of French Polynesia, *Pure Appl. Geophys.* **125**, 919-950.
- Talandier, J., and E. A. Okal (1998). On the mechanism of conversion of seismic waves to and from T waves in the vicinity of island shores, *Bull. Seism. Soc. Am.* **88**, 621-632.
- Tolstoy, I., and M. Ewing (1950). The T-phase of the shallow-focus earthquake, *Bull. Seism. Soc. Am.* **40**, 25-51.
- Walker, D. A., C. S. McCreery, and Y. Hiyoshi (1992). T-phase spectra, seismic moments, and tsunamigenesis, *Bull. Seismol. Soc. Am.* **82**, 1275-1305.
- Wilson, W. D (1960). Speed of sound in sea water as a function of temperature, pressure and salinity, *J. Acoust. Soc. Am.* **32**, 641-644.

Figure Captions

Figure 1. Bathymetry of the Easter microplate area and MELT arrays. Triangles represent Ocean-Bottom Seismometers (OBS) equipped with 3-component seismometers. GSN station RPN shows in the lower right-hand corner. Star indicates location of earthquake swarm; double lines represent the East Pacific Rise and Easter microplate Rise.

Figure 2. Smoothed envelopes of the mainshock T-phases recorded at some of the stations of the MELT array. These data are vertical component, filtered from 2 to 6 Hz. The envelope is formed by the quadrature or Hilbert transform method and smoothing is performed by a 1 s moving average. These envelopes exhibit the great variability in waveforms. Station numbers are labeled on each seismogram and locations are shown in Figure 1.

Figure 3. T-phase amplitude, envelope, smoothed envelope, and log of the smoothed envelope of one particular station (top to bottom). Noise is approximately log-normal. There is an overall gradual growth in amplitude of the log of the envelope, followed by an even slower gradual decay.

Figure 4. Comparison of the log of model (heavy line) amplitude envelope and the log of the real (thin line) T-phase amplitude envelope for the mainshock at one particular station.

Figure 5. Travel time of T-phase versus epicentral distance. The travel times are obtained from the maximum amplitude of signal using the fixed-shape model. The regression line is also plotted. The residuals from this regression line are relatively small, $R^2 = 5.8 \text{ s}^2$.

Figure 6. Variance of travel time residuals estimated from four different approaches to picking arrival times. The fixed shape model yields a reduction of about 50% in variance of travel time residuals compared to picking the peak arrival time.

Figure 7. Variations of model maximum amplitude with epicentral distance (a), receiver depth (b) and receiver azimuth (c). Model maximum amplitude tends to decrease somewhat with increasing epicentral distance and has no systematic variation with the azimuth and water depth of the receivers. Figures d to f show the variations of the characteristic time of T-phase waveform having fixed decay coefficient (γ) with epicentral distance, receiver depth and receiver azimuth, respectively. There is no systematic variation of t_b and t_c (see eq. (1)) with epicentral distance, depth or azimuth of receivers. Figures h to j display the variations of the decay coefficient (γ) with epicentral distance, receiver depth and receiver azimuth, respectively.

Figure 8. Locations of events relative to the mainshock (star). Gray ellipses represent 95% confidence estimates. (a) Locations based on T-phases; (b) locations of the corresponding events based on surface waves. In both figures, these events form two clusters about 25 km

apart that are probably located on two approximately east-west striking transform faults (Forsyth et al., 2003).

Figure 9. Vertical, radial and transverse components of ground motion (velocity) recorded at GSN station RAR in French Polynesia, a distance of about 2800 km from the mainshock. The original broadband records have been filtered from 0.02 to 0.05 Hz. (a) Mainshock, (b) the largest aftershock. The surface waveforms of these two events are very similar.

Figure 10. Distribution of GSN stations (triangles) employed in relative event surface wave locations. The azimuthal equidistant projection is centered on the epicenter of the mainshock. Azimuthal coverage is good, at least one station in each quadrant, i.e., better than the azimuthal distribution of stations recording T-phases.

Figure 11. Summed maximum amplitude of T-phase records as a function of time for foreshock sequence obtained by stacking a number of station records according to their epicentral distance from the mainshock. There are more than 50 events visible within this sequence.

Figure 12. Observed relationship between earthquake sizes based on surface wave magnitude (M_s) and the log of T phase maximum amplitude. Analysis is limited to 24 events that can be observed with both surface waves and T-phases. The regression line is

limited to events with $M_s < 4.8$ since no bigger events took place during the swarm. The linear relationship is highly significant, with $R=0.969$.

Figure 13. Square root of energy transmission and reflection coefficients. A crustal density of 2700 Mg/m^3 , a crustal P-wave velocity of 6.5 km/s and an S-wave velocity of 3.75 km/s are used to represent the average properties of the crust. A seawater density of 1000 Mg/m^3 and an acoustic velocity of 1.5 km/sec are used (a) Acoustic wave transmission coefficient for upgoing P wave (solid line) and SV (dashed line) wave incident at the seafloor. (b) Reflection coefficient for downgoing acoustic wave incident at the seafloor.

Figure 14. (a) Schematic diagram of simple multiple-reverberation seafloor-scattering model. Note that this diagram is the cross-section of 3-D model. The star represents an earthquake. The large circle represents a cross-section of the spherical seismic wave front in the crust. Two parallel heavy lines represent the sea surface and the seafloor. The continuous rebound line in the seawater represents an acoustic ray that experiences multiple reverberations in the water column. The horizontal arrows represent the T-phase generated by the point scatterers when the ray interacts with the rough seafloor. (b) Schematic distribution of intensity of scattered energy as a function of scattering angle for the first upward leg when seismic wave is incident on the seafloor at 45 degrees. (c) Schematic distribution of intensity of scattered energy for the second upward leg. The solid dots in (b) and (c) represent the incident points .

Figure 15. Synthetic T-phase envelopes. (a) Computed T-phase envelopes without considering S waves or source focal mechanism, i.e., equivalent to a spherically symmetric explosive source. The heavy solid line is predicted T-phase envelope without reverberation scattering, the dashed line is envelope taking one reverberation scattering into account and the thin solid line is for almost infinite number of reverberations. (b) Computed T-phase envelopes converted from P waves (solid line) and S waves (dashed line) respectively for a strike-slip source with 6 km depth. (c) Computed T-phase envelope from sources with the same source parameters except source depth. The solid line, dotted line and dashed line are for 1km, 3km and 6km source depth respectively. (d) Comparison of amplitude envelopes for the observed (thin line) and the computed (heavy line) T-phase for a strike-slip, shallow source. In each case, epicentral distance and corresponding travel time are assumed to be large compared to the source region of multiple reverberations and duration of the generated signal, respectively.

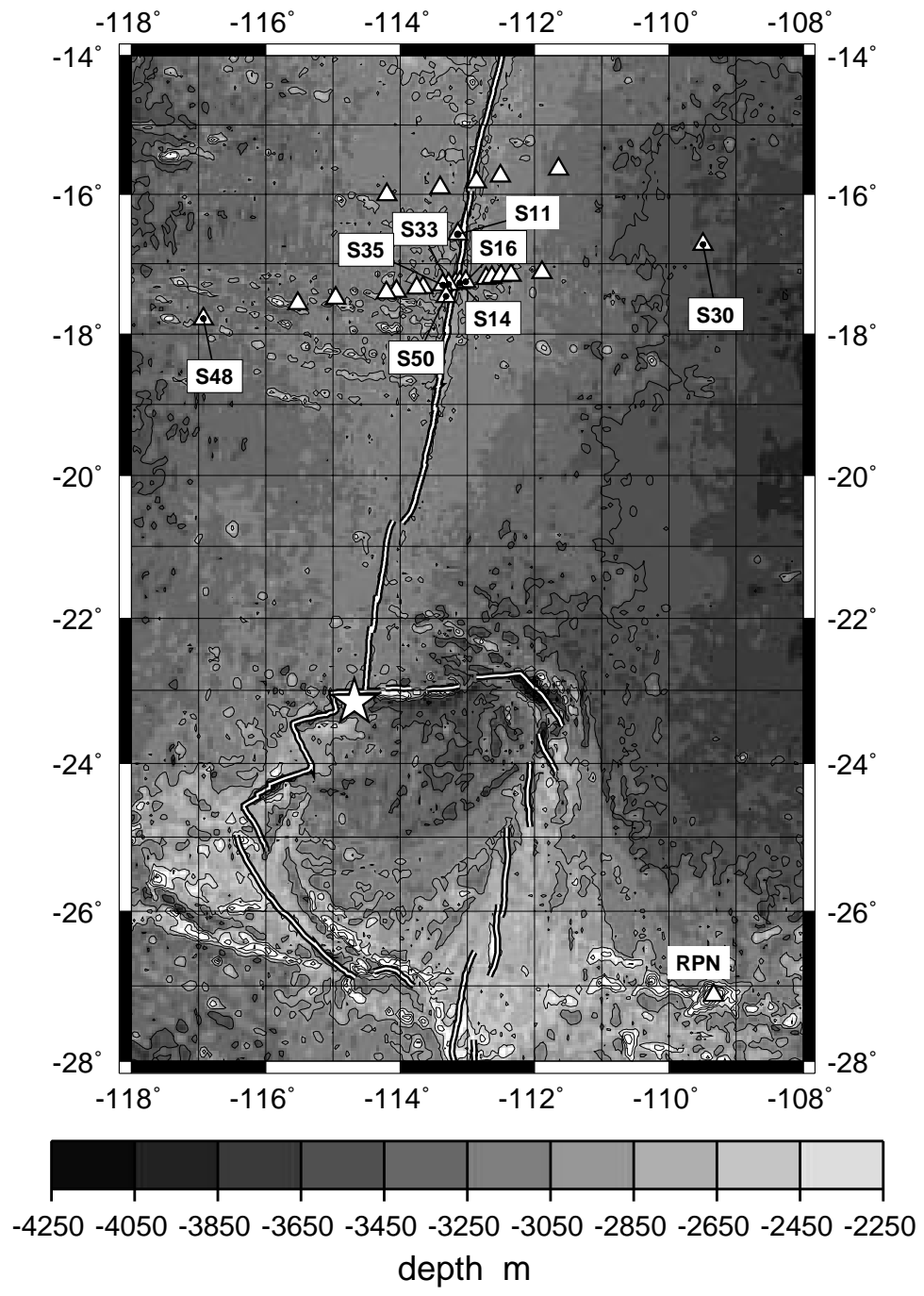


Figure 1

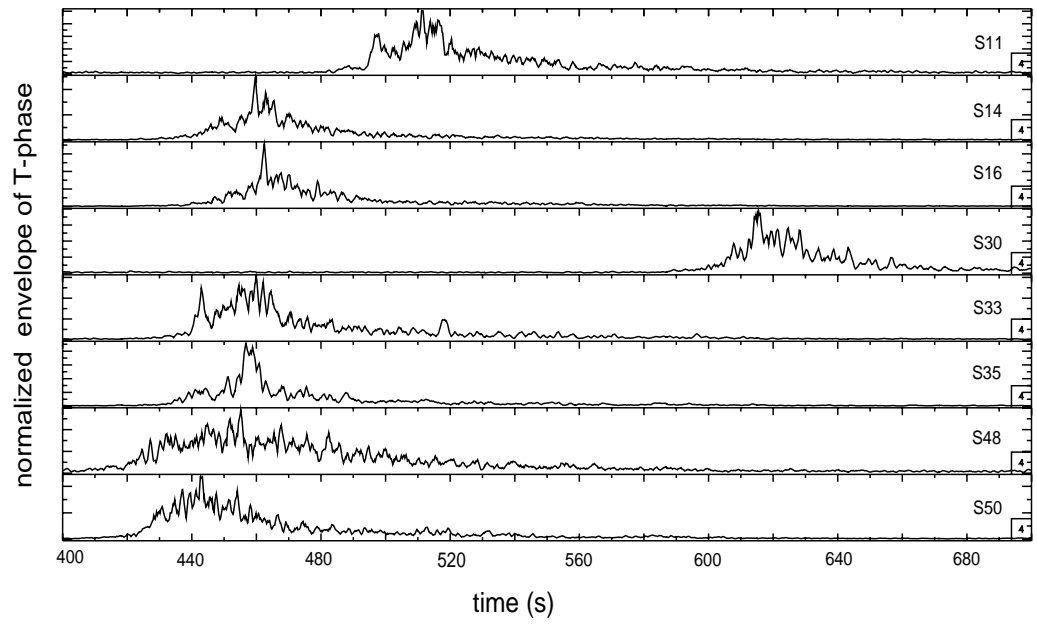


Figure 2

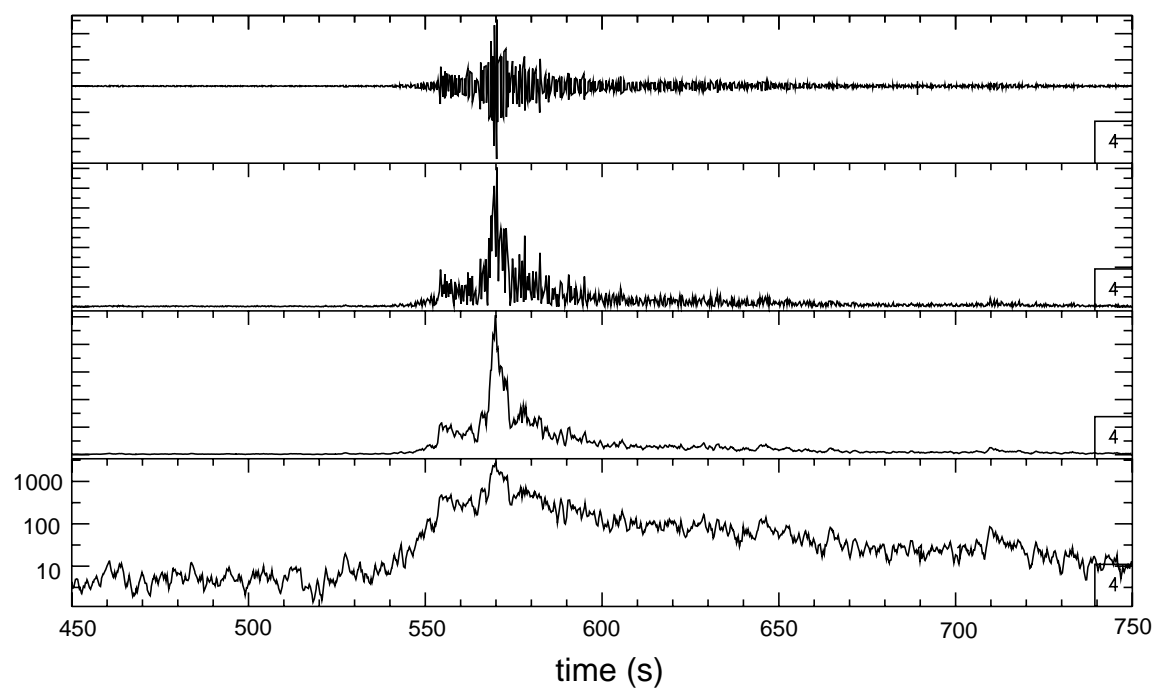


Figure 3

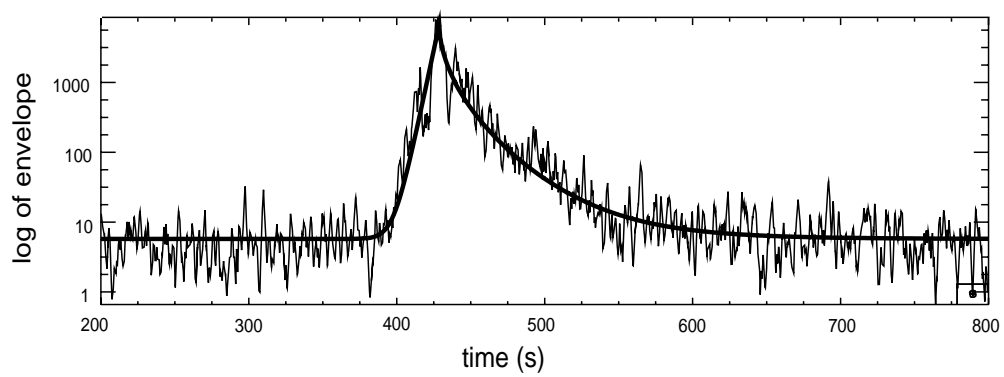


Figure 4

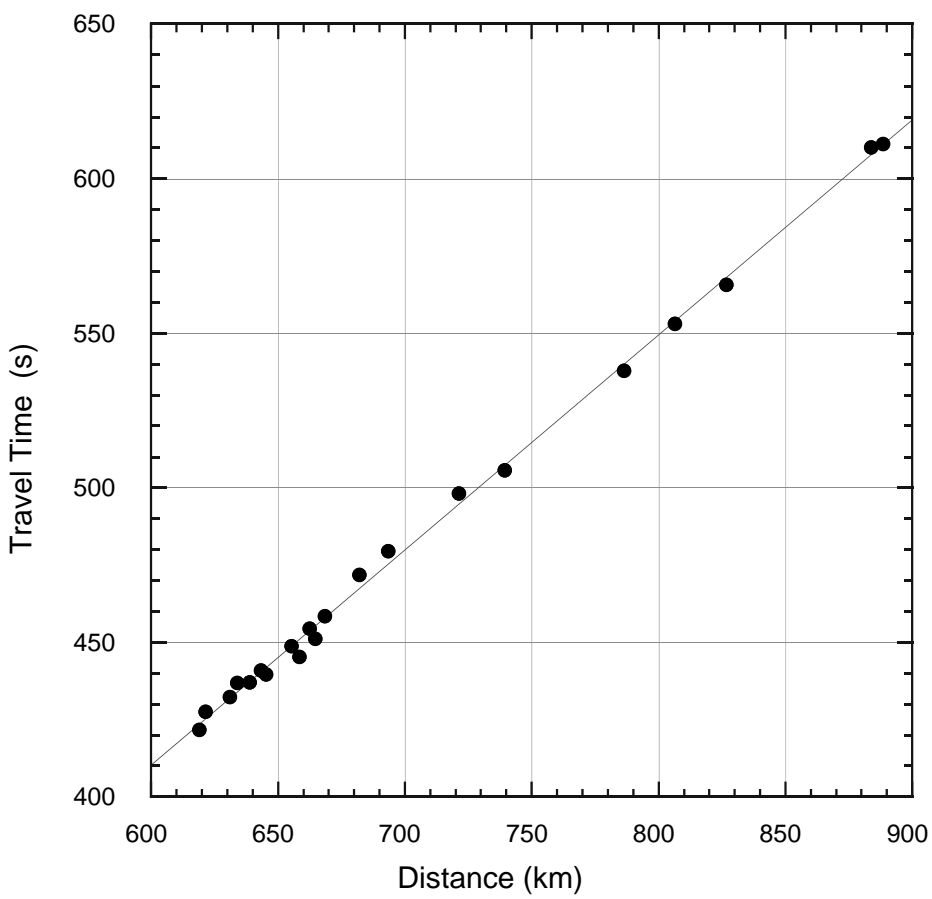


Figure 5

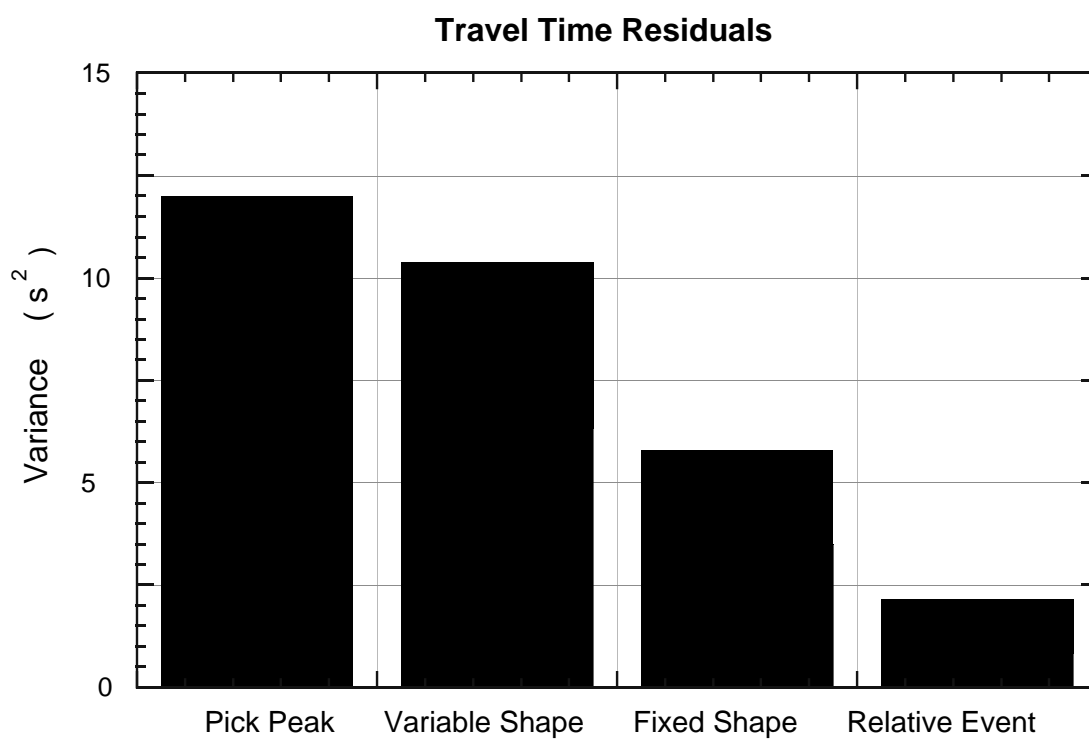


Figure 6

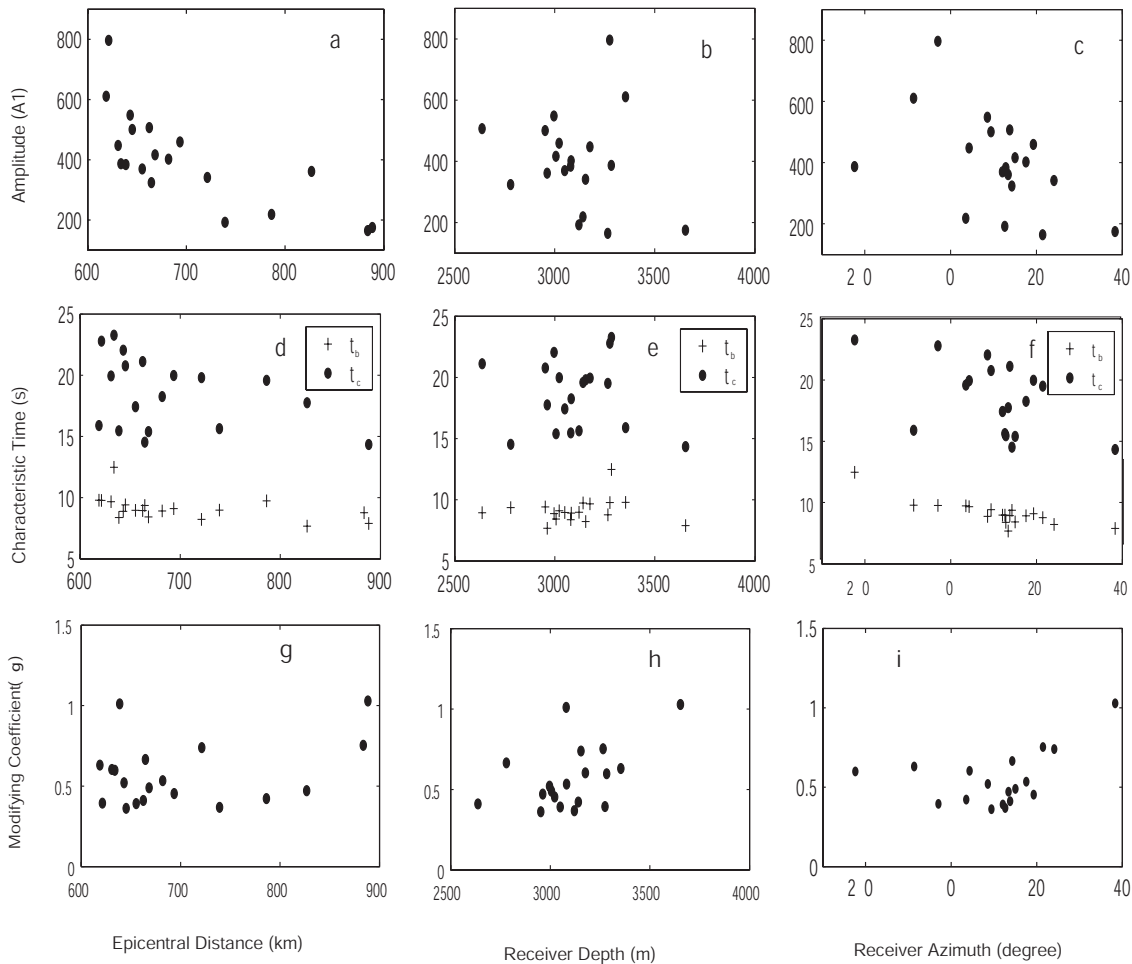


Figure 7

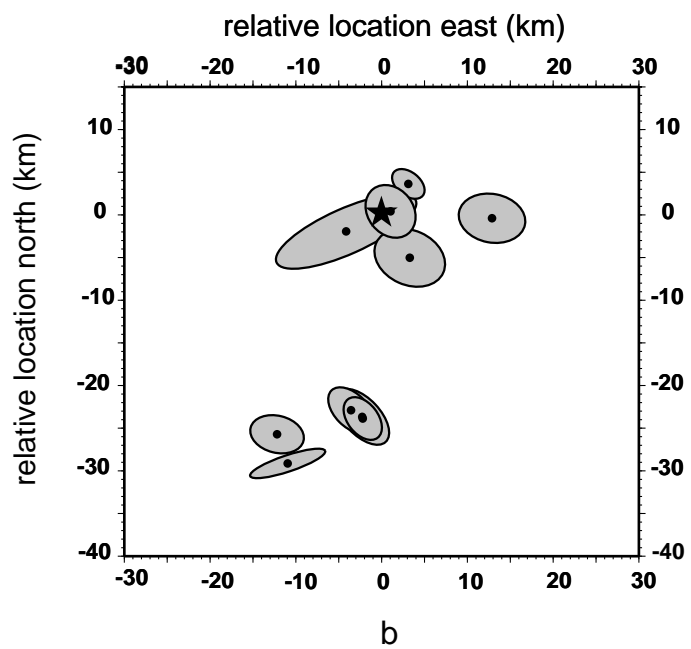
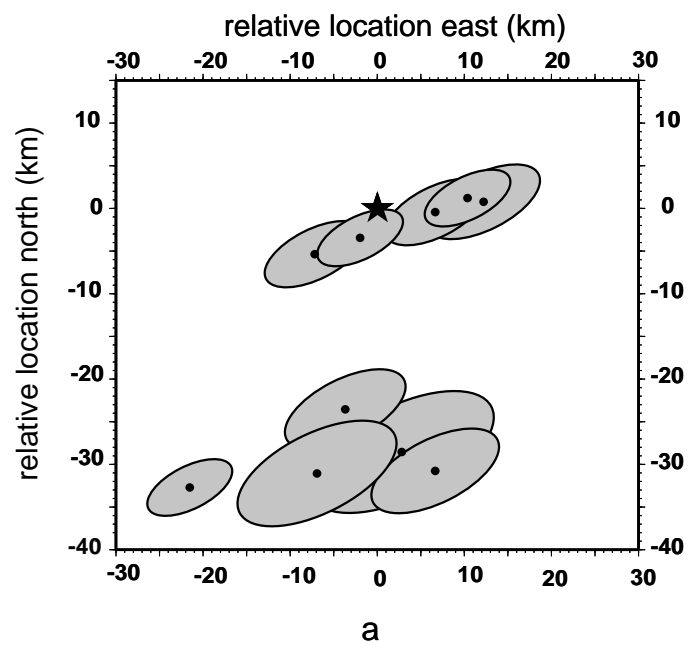
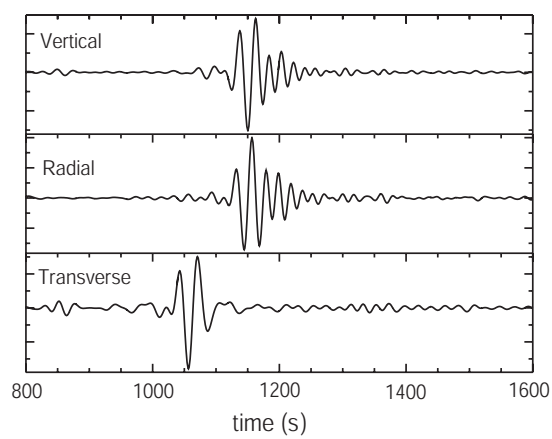
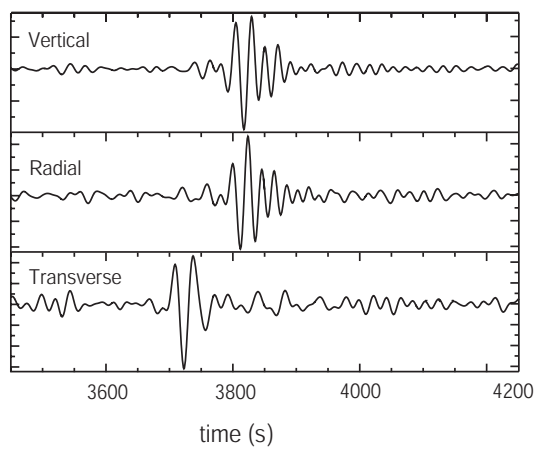


Figure 8



a



b

Figure 9



Figure 10

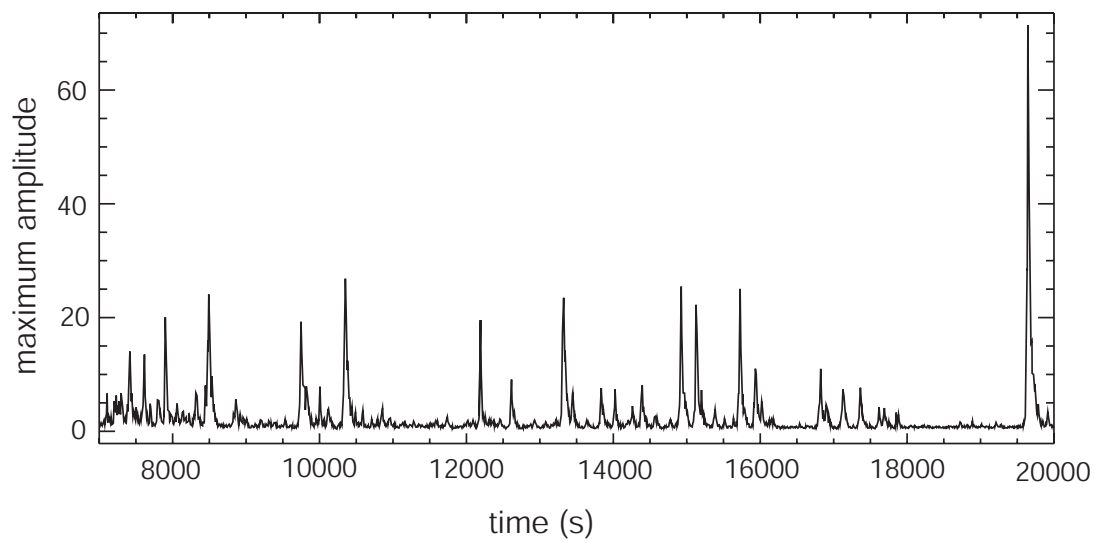


Figure 11

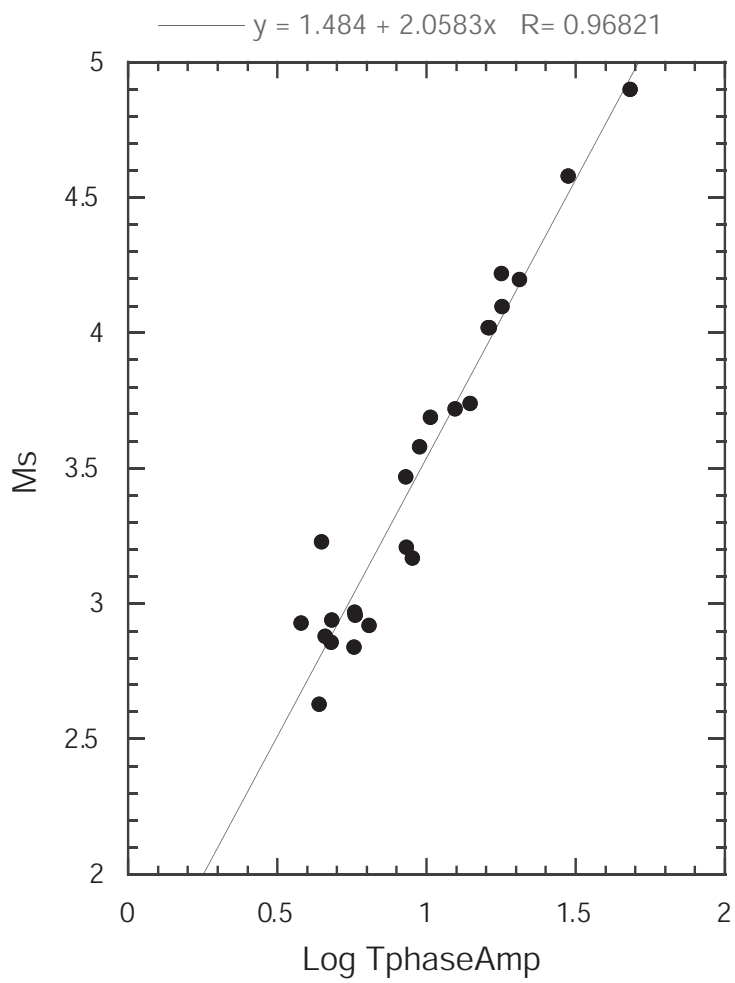


Figure 12

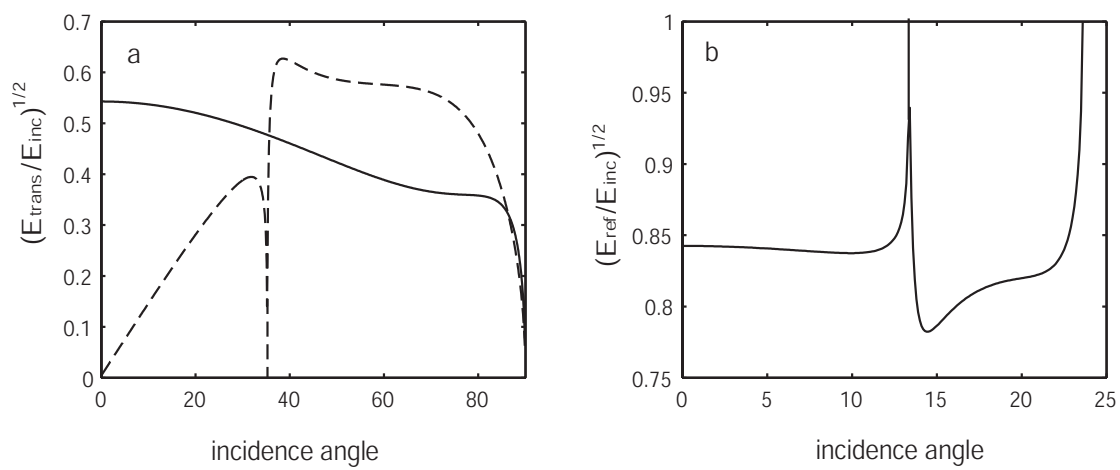


Figure 13

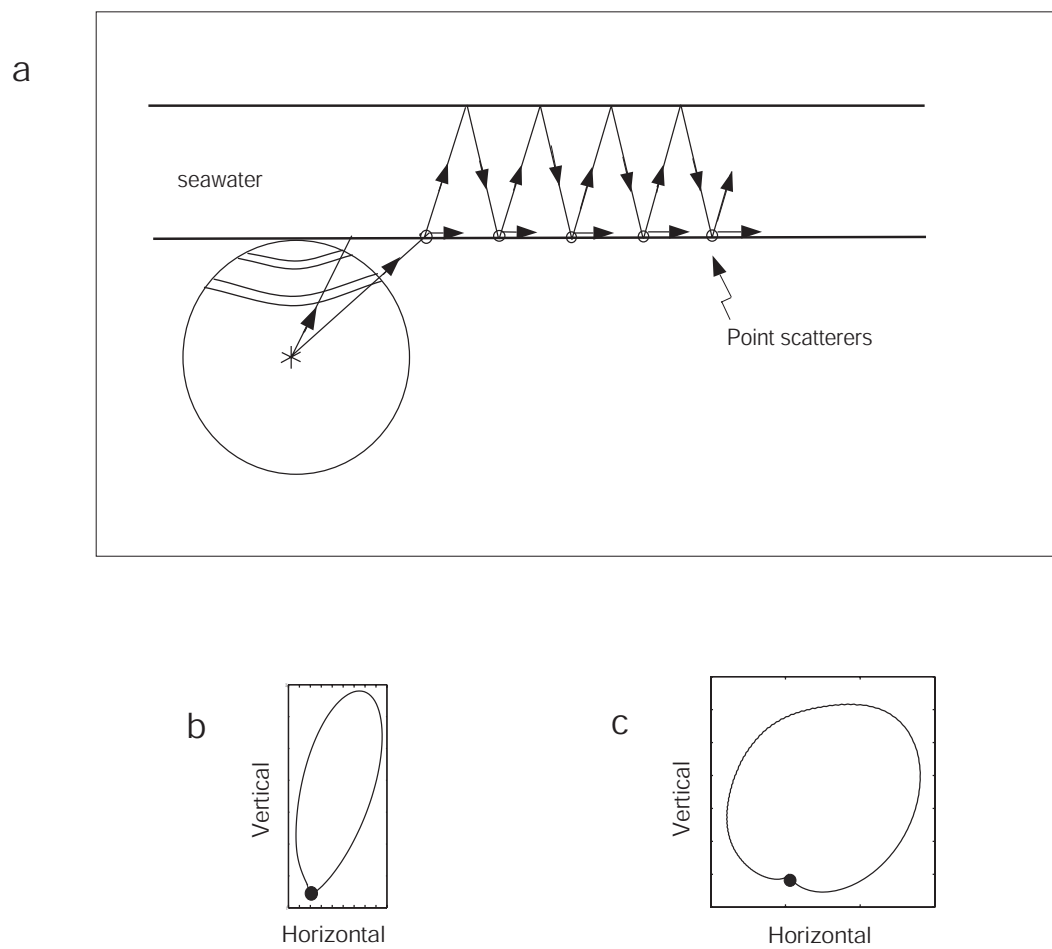


Figure 14

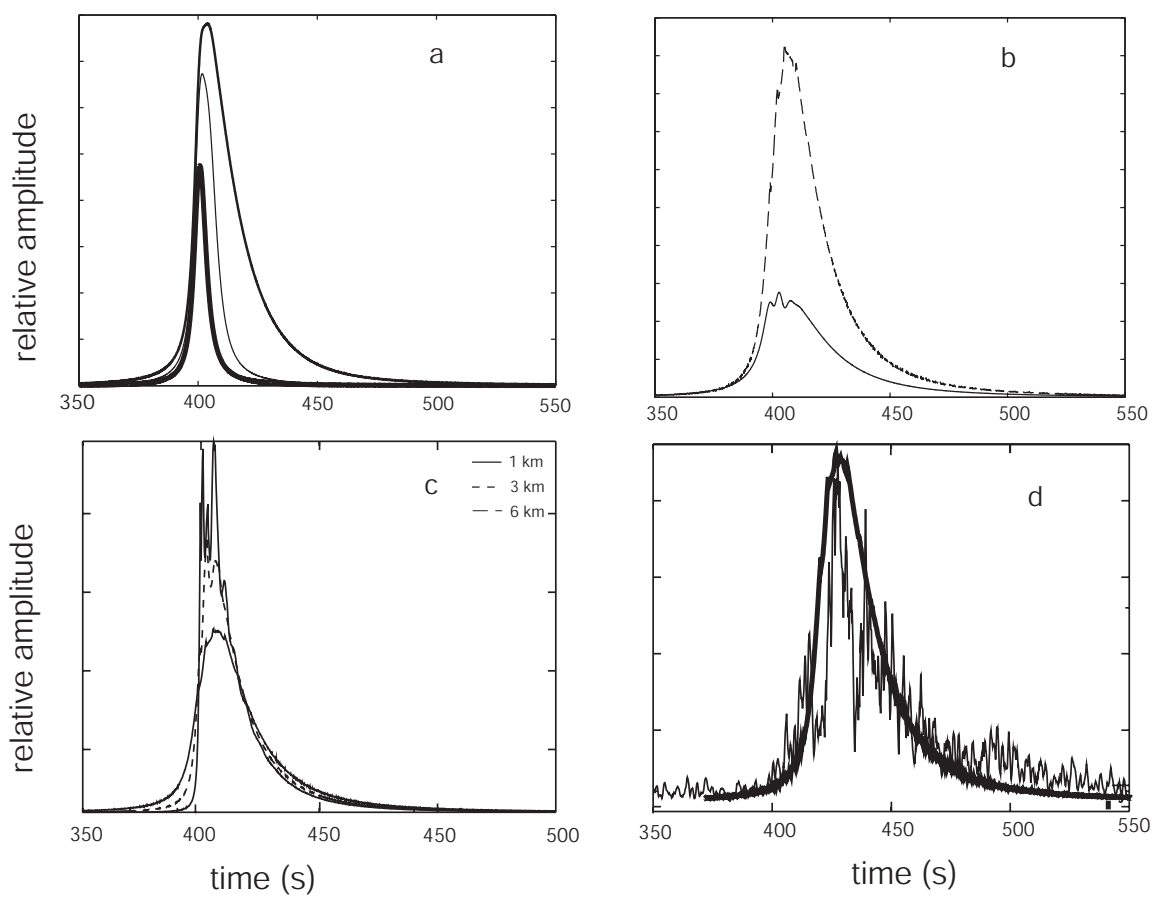


Figure 15